# ABSTRACT

Title of dissertation: 3D IONOSPHERIC EFFECTS ON HF PROPAGATION AND HEATING

Katherine Zawdie, Doctor of Philosophy, 2015

Dissertation directed by: Professor Konstantinos Papadopoulos
Department of Physics

The thesis uses a three-dimensional, first-principles model of the ionosphere in combination with High Frequency (HF) raytracing model to address key topics related to the physics of HF propagation and artificial ionospheric heating. In particular:

1. Explores the effect of the ubiquitous electron density gradients caused by Medium Scale Traveling Ionospheric Disturbances (MSTIDs) on high-angle of incidence HF radio wave propagation. Previous studies neglected the all-important presence of horizontal gradients in both the cross- and down-range directions, which refract the HF waves, significantly changing their path through the ionosphere. The physics-based ionosphere model SAMI3/ESF is used to generate a self-consistently evolving MSTID that allows for the examination of the spatio-temporal progression of the HF radio waves in the ionosphere.

2. Tests the potential and determines engineering requirements for ground-based high power HF heaters to trigger and control the evolution of Equatorial Spread F (ESF). Interference from ESF on radio wave propagation through the

ionosphere remains a critical issue on HF systems reliability. Artificial HF heating has been shown to create plasma density cavities in the ionosphere similar to those that may trigger ESF bubbles. The work explores whether HF heating may trigger or control ESF bubbles.

3. Uses the combined ionosphere and HF raytracing models to create the first self-consistent HF Heating model. This model is utilized to simulate results from an Arecibo experiment and to provide understanding of the physical mechanism behind observed phenomena. The insights gained provide engineering guidance for new artificial heaters that are being built for use in low to middle latitude regions.

In accomplishing the above topics: (i) I generated a model MSTID using the SAMI3/ESF code, and used a raytrace model to examine the effects of the MSTID gradients on radio wave propagation observables; (ii) I implemented a three-dimensional HF heating model in SAMI3/ESF and used the model to determine whether HF heating could artificially generate an ESF bubble; (iii) I created the first self-consistent model for artificial HF heating using the SAMI3/ESF ionosphere model and the MoJo raytrace model and ran a series of simulations that successfully modeled the results of early artificial heating experiments at Arecibo.

# 3D IONOSPHERIC EFFECTS ON HF PROPAGATION AND HEATING

by

Katherine Zawdie

Dissertation submitted to the Faculty of the Graduate School of the
University of Maryland, College Park in partial fulfillment
of the requirements for the degree of
Doctor of Philosophy
2015

Advisory Committee:
Professor Konstantinos Papadopoulos, Chair/Advisor
Dr. Joseph D. Huba, Co-Advisor
Professor Thomas Antonsen
Professor Adil Hassam
Professor Raymond Sedwick

*For my family and friends.*

# Acknowledgments

I am exceedingly grateful for the help I have received during my graduate school experience. First, I would like to thank my advisor, Professor Dennis Papadopoulos, for encouraging me to look deeper and really get to the heart of physics problems. It is inspiring to work with someone who has such incredible physical intuition, and his efforts have pushed me to be a better scientist.

A very special thanks is also due to my co-advisor, Dr. Joseph Huba, who has taught me to find the essence of a problem and explain it as simply and clearly as possible. I could not have hoped for a better instructor.

Many thanks also go out to the employees of the Naval Research Laboratory, particularly in the Geospace Science and Technology Branch, who have all given me advice and encouragement. I've truly enjoyed working with everyone. A special thanks goes to Dr. Sarah McDonald, whose guidance and support through the graduate school process has been invaluable. I would like to thank Dr. Douglas Drob for his boundless enthusiasm and for introducing me to adjectives. I'd like to thank Dr. Fabrizio Sassi for expanding my areas of interest and for inspiring me to continue moving forward. I would like to thank Dr. Jules Goldspiel for providing the initial opportunities that led to this work and for his continuing advice. I'd also like to thank Clayton Coker, for his encouragement and also for reminding me not to be singularly focused. In addition, I am grateful for the continued support of the Edison Memorial Graduate Training Program and the support of my supervisors, Dr. Jill Dahlburg, Dr. Christoph Englert, and Dr. David Siskind, who sponsored

me for this program.

I would like to thank the students and faculty at the University of Maryland, both for general support and also for helpful discussions. In particular the members of the Space Plasma Physics Group: Gennady Milikh, Chris Najmi, Surja Sharma, Xi Shao, and Aram Vartanyan.

I would also like to thank the other members of my committee, Dr. Adil Hassam, Dr. Tom Antonsen and Dr. Raymond Sedwick for their insightful comments and support.

I am very grateful for my husband, Dave, who has constantly supported me and who never fails to believe that I am capable of all things. In addition, I'd like to thank my family not only for their support, but for always encouraging me to think critically and to follow my own path in life. My friends, Patty Koscinski, Sasha Bishop, Ellen Wagner and Aurora Bristor also deserve recognition for their unwavering support.

To anyone who was inadvertently left out of these acknowledgments, Thank you!

# Table of Contents

List of Figures vii

List of Abbreviations ix

1 Overview 1

2 Background 4
2.1 The Ionosphere . . . 4
2.1.1 Plasma Physics . . . 5
2.1.2 Basic Structure and Composition . . . 8
2.1.3 Dynamics and Conductivity . . . 12
2.1.4 Modeling (SAMI3/ESF) . . . 17
2.2 HF Propagation . . . 22
2.2.1 Basic Physics . . . 23
2.2.2 Modeling (MoJo) . . . 26
2.3 Artificial Modification . . . 29

3 The Role of 3D Electron Density Gradients on HF Propagation 32
3.1 Medium Scale Traveling Ionospheric Disturbances (MSTIDs) . . . 33
3.2 HF Probing Techniques . . . 40
3.3 Deficiencies of 2D Models . . . 49
3.4 The Time Evolution of HF Observables During MSTID Propagation . 50
3.5 Discussion . . . 57

4 Can HF Heating Generate ESF Bubbles? 60
4.1 The Physics of Equatorial Spread F Generation in the Ionosphere . . 61
4.2 Modeling the Effects of Artificial HF Heating in the $F$-Region Ionosphere . . . 69
4.3 Can HF Heating Generate ESF Bubbles? . . . 74
4.4 Discussion . . . 79

5 The Role of Neutral Winds on $F$-Region Ionospheric HF Heating: The Snapback Effect 83
5.1 The Modification of Ionospheric Density Structures by Zonal Neutral Winds . . . 84
5.2 The Necessity for a Self-Consistent HF Heating Model . . . 90
5.3 Simulations of the Snapback Effect . . . 93
5.4 Discussion . . . 103

6 Summary 105

A MoJo 108
A.1 Overview . . . 108
A.2 Basic Symbols . . . 109
A.3 Input Parameters . . . 111
A.3.1 Electron Density . . . 111
A.3.2 Magnetic Field . . . 112
A.3.3 Collision Frequency . . . 113
A.4 Ray Tracing Equations . . . 114
A.4.1 Numerical Integration . . . 114
A.4.2 Hamilton's Equations . . . 114
A.5 The Appleton-Hartree Formulation . . . 116

Bibliography 123

# List of Figures


2.1 Example ionospheric plasma density profiles . . . . . 9
2.2 Equatorial Fountain . . . . . 16
2.3 Example of raytracing through a simple ionosphere . . . . . 26

3.1 Example MSTID as seen in airglow . . . . . 34
3.2 Simulated electron density profiles . . . . . 38
3.3 Simulated horizontal electron density gradients . . . . . 39
3.4 Example QVI . . . . . 42
3.5 Example of ray paths connecting a transmitter and receiver . . . . . 45
3.6 Sample ray fans used to construct the grid mesh pattern . . . . . 47
3.7 Grid mesh technique: background ionosphere . . . . . 48
3.8 Effect of horizontal gradients on a beam of HF rays . . . . . 51
3.9 Time series of MSTID propagating over a transmitter . . . . . 53
3.10 Virtual height as a function of time . . . . . 56
3.11 Multipath effects in QVI . . . . . 57

4.1 Example of spread F in an ionogram . . . . . 62
4.2 Example ESF in a range-time-intensity map . . . . . 63
4.3 Formation of a Rayleigh-Taylor instability . . . . . 65
4.4 Example evolution of electron density during ESF . . . . . 67
4.5 Example electron density depletion from HF heating . . . . . 70
4.6 Electron density perturbation comparison . . . . . 76
4.7 Electron density distribution along the field line . . . . . 77
4.8 Field line integrated density, Pedersen conductivity, growth rate . . . 78

5.1 Effect of an eastward zonal wind on the $F$-region ionosphere . . . . . 86
5.2 Impact of zonal wind on the morphology of electron density depletions 88
5.3 Time evolution of an artificial HF heating depletion in the presence of zonal winds . . . . . 89
5.4 Bernhardt's hypothesis for snapback . . . . . 91
5.5 Experimental observations of snapback compared to simulations . . . 95
5.6 Physical mechanism for snapback . . . . . 97
5.7 Snapback effect in three dimensions . . . . . 99

5.8 Evolution of heating longitude for different zonal wind speeds. . . . . 101
5.9 Evolution of heating longitude for different heating rates and frequencies 102

# List of Abbreviations

| | |
|---|---|
| 2D-ART | 2D Analytic Ray Tracer |
| AFOSR | Air Force Office of Science Research |
| CIS | Convective Ionospheric Storm |
| DEMETER | Detection of Electro-Magnetic Emissions Transmitted from Earthquake Regions |
| EISCAT | European Incoherent Scatter Scientific Association |
| EM | Electro-Magnetic |
| EPB | Equatorial Plasma Bubble |
| ESF | Equatorial Spread F |
| EUV | Extreme Ultra Violet |
| GPS | Global Positioning System |
| HAARP | High Frequency Active Auroral Research Program |
| HF | High Frequency |
| HWM14 | Horizontal Wind Model |
| ISR | Incoherent Scatter Radar |
| LHCP | Left Hand Circularly Polarized |
| MSTID | Medium Scale Traveling Ionospheric Disturbance |
| MURI | Multidisciplinary University Research Initiative |
| MoJo-15 | Modernized Jones Code |
| NRLMSISE00 | Naval Research Laboratory Mass Spectrometer and Incoherent Scatter Radar |
| OTHR | Over The Horizon Radar |
| QVI | Quasi Vertical Ionogram |
| RHCP | Right Hand Circularly Polarized |
| SAMI3 | Sami is Another Model of the Ionosphere |
| Sq | Solar quiet |
| TID | Traveling Ionospheric Disturbance |
| UV | Ultra Violet |

# Chapter 1: Overview

Radio wave propagation plays a major role in modern life due to our increasing reliance on technology; GPS, satellite communications and over-the-horizon radars send electromagnetic waves through the ionosphere at different frequencies. When the ionosphere is disturbed it can cause severe technological problems affecting navigation and communication systems. To better understand the ionospheric processes scientists have developed a method of active experiments where strong radio waves are used to heat the ionospheric plasma. The resulting perturbations in the plasma can be studied and insights gained from the experiments to develop understanding and prediction of the state of the ionosphere as well as improve the performance of the relevant transionospheric systems.

In this dissertation the effect of ionospheric processes on radio wave propagation and artificial heating is examined using physical models. Chapter 2 provides background on both the ionosphere and HF propagation. The ionosphere background section begins by summarizing important properties that are common to plasmas. Next, the composition and structure of the ionosphere and its dynamical properties and conductivity are outlined. As this dissertation deals extensively with ionospheric modeling, the governing equations for the ionosphere are presented in

the context of an ionospheric model, SAMI3/ESF. The following section details the basic physics of HF radio wave propagation in the ionosphere. The raytrace code, MoJo, which simulates radio wave propagation is outlined. Finally, a brief summary of the physics of artificial ionospheric modification is provided.

Chapter 3 utilizes the first-principles ionosphere code, SAMI3/ESF and the 3D raytrace model, MoJo, to examine the effect of ionospheric density gradients generated from Medium Scale Traveling Ionospheric Disturbances (MSTIDs) on HF radio wave propagation. The chapter begins with a summary of the MSTID characteristics and an outline of the techniques used to model the structures in the ionosphere. Next, HF probing techniques are considered, and the basic observable quantities are described. The importance of a 3D raytrace code compared to a 2D code is then considered, followed by an in depth look at how ionospheric density gradients affect high angle of incidence HF radio wave propagation. The discussion and conclusions section follows.

In Chapter 4, we examine whether artificial HF heating can generate or alter the formation of Equatorial Spread F (ESF). First, the general properties and the physics of ESF bubble formation are discussed and previous work in ESF modeling is outlined. Next, the density structures that form due to artificial HF heating are described, followed by an overview of previous studies that have modeled artificial ionospheric heating. Once the phenomena have been introduced, we utilize the models to determine whether artificial HF heating can generate ESF bubbles, and briefly consider whether HF heating could suppress an ESF bubble. Finally we present a discussion and conclusions section.

The interaction between the ionosphere and artificial HF heating are examined in Chapter 5. In order to study these phenomena, a raytrace model (MoJo) and the 3D ionospheric model (SAMI3/ESF) are coupled to form a self-consistent ionospheric HF heating model. The first topic outlined in the chapter is the physics of how zonal neutral winds affect the $F$-region ionosphere and how they modify density cavities formed by artificial HF heating. Then an earlier HF heating experiment at Arecibo Observatory is described, which suggests that there are indeed interaction effects between the heater wave and the evolving ionospheric density cavity. The new self-consistent model is then outlined and used to simulate the results from the Arecibo experiment, in the process providing new insight into the physical mechanism responsible for the observations. This is followed by discussion on the implications of the work for future HF heater development and some conclusions.

Chapter 6 presents the overall summary and conclusions of the dissertation.

# Chapter 2: Background

## 2.1 The Ionosphere

The neutral atmosphere and the ionosphere are geospace regions closest to the surface of the Earth. The neutral atmosphere extends from the Earth's surface to about 1000 km. The lowest regions, the troposphere, stratosphere, and mesosphere, are critical for the control of the surface temperature and they also filter solar radiation. The next layer is the thermosphere, which extends from about 85 to 500 km altitude. The final layer is the exosphere, which reaches altitudes of 1,000 km. The term ionosphere is used to distinguish the ionized portion of the upper atmosphere with the background neutral particles. The ionosphere resides between about 60 to 3,000 km altitude, and is unique in that it is affected both from dynamical processes originating in atmospheric regions close to the Earth, and also by solar forcing from above.

The ionosphere can be well described with the equations of plasma physics, so the first task is to summarize some basic properties of a plasma. The basic processes responsible for the formation of the ionosphere has been understood since about the middle of the 20th century and in general, the climatology of the geomagnetically quiet ionosphere is reasonably well accounted for. It is still not possible to predict

ionospheric weather, where the conditions deviate from the monthly mean values due to solar activity, but advances in this field continue to be made. In addition, during quiet periods, dynamical processes in the lower atmosphere can cause significant day to day variations in the ionosphere, but the coupling between the two are not well understood. Next, the basic structure, composition and electrodynamic properties of the ionosphere are examined. Dynamical processes that occur in the ionosphere are briefly outlined. Finally, the governing equations for the ionosphere in the context of an ionospheric model, SAMI3/ESF, which is used extensively in this work, are presented.

### 2.1.1 Plasma Physics

Plasma is an ionized gas that exhibits collective behavior, which means that the local state of the plasma depends on the state of plasma in more remote regions. The cause for the collective behavior is the fact that the particles are charged. If the motion of local plasma creates concentrations of positive and negative charge, an electric field is generated. In addition, moving charges constitute a current, which in turn generates a magnetic field. Thus, the motion of charged particles in a local region of the plasma can generate electromagnetic fields that affect the plasma in more remote regions. In this section we outline some of the key parameters that describe a plasma. For further reference on this topic, refer to [50].

One important plasma quantity is the Debye length, $\lambda_D = (\epsilon_0 k T_e / n_e e^2)^{1/2}$, which defines the smallest distance over which plasma can exhibit collective behav-

ior. A typical value of $\lambda_D$ for the peak of the Earth's ionosphere is 1 cm. Another way to look at the Debye length is in terms of shielding: local charge separations can occur on scales of the Debye length without affecting the neutrality of the plasma system as a whole. A plasma of this type is called quasi-neutral and for a system of size L it must meet the requirement $\lambda_D << L$. Note that for this concept to be statistically valid, the definition of a plasma requires that the local plasma density be sufficiently dense such that the number of particles in a Debye sphere is much greater than unity. Namely, the Debye sphere ($N_{\lambda_D}$), $N_{\lambda_D} = 4\pi\lambda_D^3 n_e/3 >> 1$. A typical value of $N_{\lambda_D}$ for the Earth's ionosphere is $4.2 \times 10^5$ [50], so the ionosphere can be considered quasi-neutral plasma.

Another important plasma quantity is the cyclotron frequency, or gyrofrequency, defined as: $\omega_{\alpha cf} = e|B|/m_\alpha$, where $\alpha$ represents either an electron ($e$) or an ion ($i$). The cyclotron frequency describes the gyration frequency of a charged particle about the background magnetic field lines. For a plasma immersed in a strong magnetic field, like the ionosphere, the cyclotron frequency determines the magnitude and direction that external forces will have on the plasma particles. For example, the Earth's ionosphere is coincident with a neutral atmosphere, and the importance of the neutral particles on the plasma can be determined by comparing the collision frequency of the charged particles with the neutral particles ($\nu_{\alpha n}$) to the cyclotron frequency. If the cyclotron frequency is much less than the collision frequency, $\omega_{\alpha cf} << \nu_{\alpha n}$, then collisions with the neutral particles dominate the plasma motion and the force of neutrals on the plasma particles causes motion in the direction of the force. On the other hand, if the cyclotron frequency is much

larger than the collision frequency, $\omega_{\alpha cf} >> \nu_{\alpha n}$, the particles are effectively tied to the magnetic field lines. For intermediate cases, the angle of the plasma drift relative to the force is given by: $\tan^{-1}(\omega_{\alpha cf}/\nu_{\alpha n})$. The ratio between the collision frequency and the cyclotron frequency is crucial to understanding the dynamics of the ionosphere.

Plasmas are also affected by electric fields, such as those created by High Frequency (HF) radio waves. The plasma frequency, $\omega_{p_\alpha} = (n_\alpha e^2/\epsilon_0 m_\alpha)^{1/2}$, describes how quickly the particles in a plasma react to an electric field. Due to their large mass, the ions are not easily affected by HF electromagnetic fields. The electron plasma frequency, however, is on the same order as HF radio waves, so the electrons are strongly affected by incident HF radio waves and vice versa. The cutoff frequencies and resonance frequencies for radio wave propagation in a plasma are strongly dependent on the electron plasma frequency. In this dissertation the electron plasma frequency is frequently referred to as "the" plasma frequency because it is the one that is relevant for HF propagation.

A particularly successful method for describing and modeling the ionosphere is using a plasma fluid model method. The fluid equations are composed of the continuity, momentum and energy equations and they describe the time and spatial evolution of a plasma as a fluid. Details on the actual equations that can be used to describe a plasma will be discussed in Section 2.1.4.

### 2.1.2 Basic Structure and Composition

The plasma in the ionosphere is generated by ionization of the background neutral particles. The primary ionizing force is radiation from the sun during the day, which is called photoionization. Ions can also be produced via impact ionization of neutral atoms, molecules and high energy electrons and indirectly due to chemical exchange. These processes are all height dependent since the ionosphere is nonuniform. It can generally be assumed that the ionosphere is quasi-neutral, thus the total electron density is equal to the sum of the ion density components.

The spatial form of the electron density profile can be mostly explained by simply looking at the production and loss of ions due to direct photoionization and recombination. Solar photons are able to create more ion electron pairs as they go deeper in the ionosphere since there are more neutrals available to ionize. The increase in neutral density, however, also leads to an increase in the recombination rate. The peak layer of ionization is formed at the altitude where the photoproduction and recombination rates balance. At nighttime the ionizing radiation from the sun goes away and the ionosphere quickly becomes depleted due to electron-ion recombination.

During the day, the ionosphere is composed of a number of different layers: the $D$-region, the $E$-region and the $F$-region. Each region is ionized by a different wavelength of radiation and they tend to occur at specific altitude ranges. The regions are identified by peaks in the electron density and can be characterized further by examining the primary ion composition and the wavelength that most

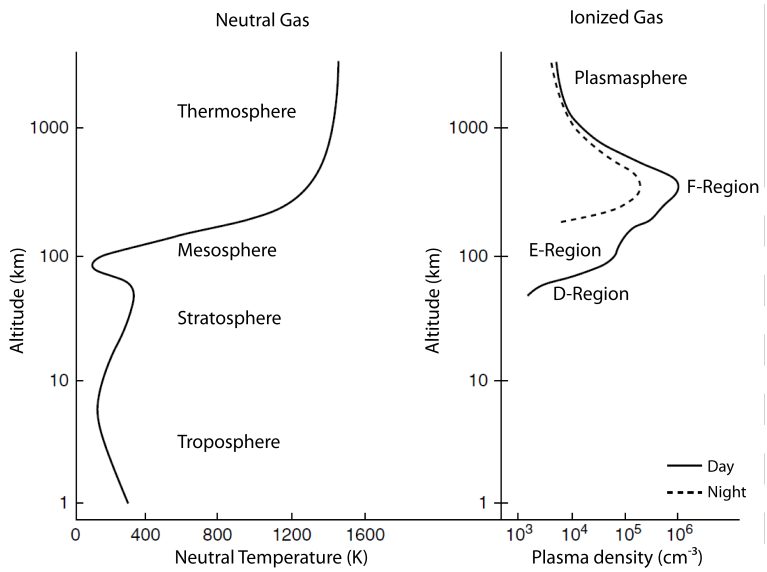


Figure 2.1: An example of a typical midlatitude neutral atmospheric temperature profile (left panel). Representative daytime and nighttime ionospheric density profiles with the ionospheric regions labeled. (Reproduced from [30])

efficiently ionizes neutral particles in that altitude range. In general, the molecular ion species dominate regions at lower altitudes and the atomic ion species dominate higher altitude regions. The $F$-region plasma density exceeds the other regions, so the peak of this region is often referred to as the peak density of the ionosphere. The altitude region below the peak is often called the bottomside ionosphere and the altitude region above the peak is referred to as the topside ionosphere. Chemical processes tends to be more important in the bottomside ionosphere and diffusion process generally dominate above the peak. Figure 2.1 shows an example ionospheric layer for both the daytime and the nighttime.

In the $D$-region, chemical processes are very important. Molecular ions are dominant, particularly $NO^+$ and $O_2^+$. The $D$-region covers about 60-100 km alti-

tude. In this layer there can be both positive and negative ions. There are also water cluster ions and three-body chemical reactions become important. The $D$-region is produced by Lyman alpha (121.6 nm), X-rays ($< .8$ nm) and cosmic rays and the neutrals in this region are primarily $O_2$ and $N_2$. The layer mostly disappears at night.

The $E$-region ranges from about 100 to 150 km altitude. Chemical processes are also important in this layer. The region is weakly ionized, so collisions between charged particles are less important than collisions with the neutral atmosphere. There is some ionization at night, but it is significantly reduced compared to daytime levels. The primary ions are $O_2^+$ and $NO^+$. The $E$-region is produced by EUV radiation (80-102.6 nm) and soft X-rays (1.0-10.0 nm). The photoionization mainly ionizes $O_2$ molecules, but rapid charge-exchange and atom-ion interchange also produces $O_2^+$ and $NO^+$ ions. Recombination in this region is mainly through dissociative recombination.

During the day, the $F$-region divides into separate regions: the $F1$-region and the $F2$-region. The $F1$-region generally lies between 150 to 250 km altitude. Here ion-atom interchange and transport processes become important. The atomic species $O^+$, $O_2^+$ and $NO^+$ dominate. The primary ionizing radiation is from UV lines and continuum, which are between 100-800 Å. At night this layer combines with the $F2$-region.

The $F2$-region is the densest region because in this region the plasma transport and chemical loss processes are balanced. The dominant atomic species is $O^+$. The plasma processes are dominant in the topside region above the $F$-region peak where

the primary ions are $O^+$ and $H^+$. The plasmasphere region consists of the region between about 1200 km altitude and 4-6 Earth radii; the primary ions in this region are $H^+$ and $He^+$.

At nighttime the lower regions, which are dominated by chemical processes, tend to shrink very rapidly because the chemical rates for dissociative electron-ion recombination is much faster for the molecular ions that are abundant at these altitudes. The $F$-region reduces to one peak, and is partially maintained by outflow from the plasmasphere. Altitudes above the $F$-region are dominated by transport processes, and thus are largely unaffected by the transition from daytime to nighttime.

The ionospheric densities vary with local time, latitude, season and solar cycle. For this work we only consider quiet times, where geomagnetic activity is low, but in general the ionosphere is very strongly affected by geomagnetic storms. While the ionosphere is ionized and needs to be described with the equations of plasma physics, the density of the background neutral particles below about 1000 km generally exceeds the density of ions, so the neutrals play a large role in ionospheric composition and dynamics. In particular, since the ionosphere is generated from the ionization of neutral particles, the variation of neutral particle concentration influences the composition of the ionosphere. Also, the dynamics of the thermosphere, which during quiet geomagnetic activity conditions is primarily driven by solar heating, has a significant effect on the dynamics of the ionosphere. This effect will be discussed in a later section.

### 2.1.3 Dynamics and Conductivity

The ionosphere is made up of charged particles, and as the motion of charged particles describes a current, we are naturally interested in the conductivity, or the the ability of the ionosphere to carry a current. The current is given by Ohm's Law:

$$\mathbf{J} = \overline{\overline{\boldsymbol{\sigma}}} \cdot \mathbf{E} \tag{2.1}$$

where $\overline{\overline{\boldsymbol{\sigma}}}$ is the conductivity tensor, which can be defined as:

$$\overline{\overline{\boldsymbol{\sigma}}} = \begin{pmatrix} \sigma_P & -\sigma_H & 0 \\ \sigma_H & \sigma_P & 0 \\ 0 & 0 & \sigma_\parallel \end{pmatrix}, \tag{2.2}$$

This equation assumes that the $\hat{\mathbf{z}}$ direction is parallel to the magnetic field. Then $\sigma_\parallel$ is the conductivity parallel to the magnetic field, $\sigma_P$ is the Pedersen conductivity, and $\sigma_H$ is the Hall conductivity.

The different conductivities describe the ability of the charged particles to move in relation to the magnetic field and generally are a function of altitude. The exception is the parallel, or specific, conductivity ($\sigma_\parallel$), which is several orders of magnitude larger than the other two conductivities at all altitudes since charged particles at all altitudes can move very easily along the magnetic field lines. It is defined as:

$$\sigma_\parallel = en_e \left( \sum_i \frac{\omega_{icf}}{B_0 \nu_{in}} - \frac{\omega_{ecf}}{B_0 \nu_{en}} \right) \tag{2.3}$$

The parallel conductivity is often assumed to be infinite, which implies that the magnetic field line is an equipotential. This approximation is reasonable for time scales where Ohm's Law is valid.

The other two conductivities describe the ability of the charged particles to move in directions perpendicular to the magnetic field line. If the magnetic field is sufficiently strong that the cyclotron frequency is much larger than the neutral collision frequency, then the plasma is said to be magnetized. A magnetized plasma tends to be "frozen in" to the magnetic field lines, which means that collisions can force a particle up and down the magnetic field line, but cannot drive the particle off of the field line. Even for a magnetized plasma, however, the particles can still be driven from the magnetic field due to forces from electric fields, which cause an $\mathbf{E}\times\mathbf{B}$ drift perpendicular to the magnetic and electric fields. The ratio of the cyclotron frequency to the neutral collision frequency changes as a function of altitude for both the ions and the electrons because it depends on the collision frequency with the neutral particles, which tends to decrease as a function of altitude.

The electrons become magnetized around the bottom of the $D$-region ($\sim$ 70 km), but the ion cyclotron frequency is much larger than the ion neutral collision frequency ($\omega_{icf}/\nu_{in} << 1$), which results in unique dynamical processes, as the electrons are frozen into the magnetic field, but the ions are highly influenced by neutral collisions. This region is also referred to as the Hall Magneto-Hydrodynamic (MHD) region. The Hall conductivity is both perpendicular to the background magnetic field and the applied electric field. It is defined as follows:

$$\sigma_H = \frac{en_e}{B}\left(\frac{(\omega_{ecf}/\nu_{en})^2}{1+(\omega_{ecf}/\nu_{en})^2} - \sum_i \frac{(\omega_{icf}/\nu_{in})^2}{1+(\omega_{icf}/\nu_{in})^2}\right) \tag{2.4}$$

By day, at $F$-region altitudes, the Hall conductivity is the smallest of the conductivities. At night it is negligible, so it will not be considered further in this work.

At the peak of the $E$-region ($\sim$ 120 km), $\nu_{in}/\omega_{icf} \sim 2$, so the ions will move at an angle of $\tan^{-1}(\omega_{icf}/\nu_{in})$ to an applied force. In the $F$-region, the electrons and ions are both fully magnetized; however, the electrons are tied more tightly to the magnetic field lines. In the case of the ions $\nu_{in}/\omega_{icf} \sim 1/300$, $\tan^{-1}(\omega_{icf}/\nu_{in}) \sim 90°$, so the ions tend to move perpendicularly to applied forces. The Pedersen conductivity is important in the $F$-region ionosphere and also in the generation of the Rayleigh-Taylor instability that is described in Chapter 3. The Pedersen conductivity is the conductivity that is perpendicular to the background magnetic field, and parallel to the applied electric field. It can be defined as follows:

$$\sigma_P = \frac{en_e}{B}\left(\sum_i \frac{\omega_{icf}/\nu_{in}}{1+(\omega_{icf}/\nu_{in})^2} - \frac{\omega_{ecf}/\nu_{en}}{1+(\omega_{ecf}/\nu_{en})^2}\right) \tag{2.5}$$

In summary, in the Earth's ionosphere, the electrons are largely constrained to the magnetic field lines, whereas the ions at low altitudes can be influenced by the motion of the neutral atmosphere. The ions still move more freely along the magnetic field than in other directions. So for both electrons and ions, the shape of the magnetic field is extremely important in understanding the dynamics of the ionosphere. At ionospheric altitudes the geomagnetic field is dipolar, so the field lines are parallel to the Earth near the magnetic equator and the inclination angle increases as a function of latitude. The primary drivers for the field-aligned motion are gravity, density and temperature gradients, field-aligned neutral winds and collisions with neutral particles.

Gravity tends to pull particles down along the magnetic field, but it also plays another important role: it sets up the ambipolar electric field. Since the ions are

much heavier than the electrons, the gravitational force is stronger on the ions than it is on the electrons. This leads to a slight charge separation, on the order of the Debye length, which leads to a polarization electric field that causes the ions and electrons to move together as a single fluid to prevent further charge separation. This motion is called ambipolar diffusion.

Another important driver of the ionosphere is the horizontal neutral winds in the thermosphere. As the neutral atmosphere is heated by solar EUV radiation, it expands, causing winds to flow away from the subsolar point. In general, there is an eastward flow from the day side to the night side. During the day the north-south (meridional) winds are polewards. At night they reverse and tend to flow towards the equator. In general, the meridional winds are symmetric about the equator and the amplitude increases from low to higher latitudes. Particularly in the $E$ and $F$-regions, these winds drive currents and produce electric fields that very strongly affect the ionosphere.

In the $E$-region, the ions are not fully magnetized, so the neutral winds can drive the ions off of the magnetic field lines, whereas the electrons are constrained to the field lines. The differences in the ion and electron motions leads to the generation of currents and electric fields. This results in a global current system, which is known as the solar-quiet (Sq) current system. It is important to note that this is a global current system driven by tidal oscillations of the atmosphere (primarily the diurnal tide), so the local neutral wind direction is not a major factor here. At the equator, where the magnetic field lines are nearly horizontal, the Sq current is strongly enhanced, and this enhanced current is known as the equatorial

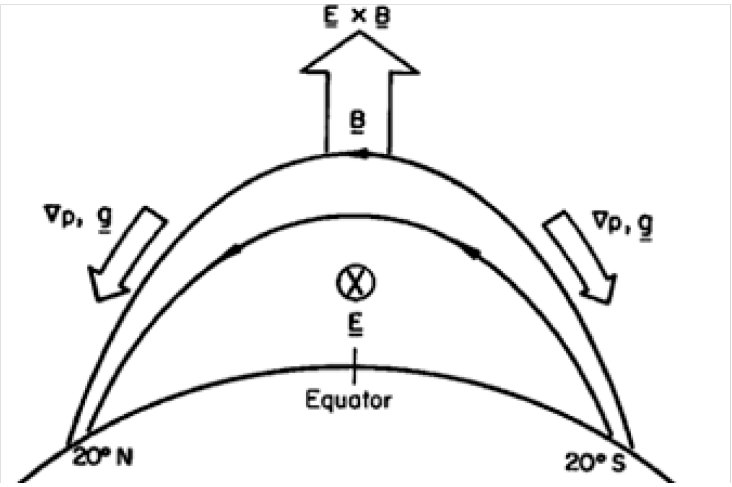


Figure 2.2: The Equatorial Fountain is generated from the $E$-region dynamo, which produces an eastward electric field during the day. The resultant $\mathbf{E} \times \mathbf{B}$ drift drives the plasma upwards across the magnetic field lines. The lifted plasma is drawn back down the field lines due to the gravitational force, which causes density enhancements along the magnetic equator. (Reproduced from [30])

electrojet. The resultant dynamo electric field is called the $E$-region dynamo. The field is in the eastward direction during the daytime, which causes an upward $\mathbf{E} \times \mathbf{B}$ drift of the plasma. At night, the field is westward, resulting in a downward $\mathbf{E} \times \mathbf{B}$ drift. The daytime upward plasma drift (along with ambipolar diffusion) drives the plasma upward; it then falls down along the geomagnetic field lines due to the gravitational force. A schematic of this process is shown in Figure 2.2. This effect is known as the "equatorial fountain" effect and the resulting enhanced plasma density in the $F2$-region of the tropical ionosphere is known as the Appleton or equatorial anomaly. The morphology of the equatorial anomaly crests vary with solar cycle, season, time of day, and longitude.

### 2.1.4 Modeling (SAMI3/ESF)

SAMI3/ESF (Sami Is Another Model of the Ionosphere/Equatorial Spread F) is a three-dimensional physics-based model of the ionosphere [21]. The code includes 21 chemical reactions, dissociative and radiative recombination and simulates plasma along the entire dipole electric field line. Quasi-neutrality is assumed, so the electron density is determined by summing the densities of each ion species. SAMI3/ESF includes both vertical and longitudinal $\mathbf{E} \times \mathbf{B}$ drifts perpendicular to B, and ion inertia parallel to B, which is included in the ion momentum equation for motion along the geomagnetic field.

The code uses a nonorthogonal, nonuniform fixed grid that follows the Earth's geomagnetic field. While the Earth's magnetic field is generally modeled as a tilted-dipole field, in this work we use a non-tilted dipole for simplicity so geographic and magnetic latitude are the same. The grid is periodic in longitude and simulates a $4^\circ$ longitudinal wedge of the ionosphere with a fine longitudinal grid. The neutral composition and temperature are specified using the empirical NRLMSISE00 model. The neutral wind may either be specified using the empirical Horizontal Wind Model (HWM14) or for simplicity can be set to a constant [10].

The equations used in SAMI3 are the five-moment system of transport equations for a plasma. This approximation assumes that the velocity distribution for the species in the plasma can be adequately represented by a drifting Maxwellian. The system of equations is made up of the continuity, momentum, and temperature equations. For a good description of the five-moment approximation and its

limitations, see [50]. We describe the basic equations here, but it should be noted that the equations in the code are actually in the dipole coordinate system. The full equations in the dipole coordinate system are described in the original reference paper [20].

In the following equations, the number density of an ion species is denoted as $n_i$, the electron number density is $n_e$. The mass of of an ion species is $m_i$ and the electron mass is $m_e$. The density of an ion species is $\rho_i = m_i n_i$.The drift velocity of an ion species is denoted as $\mathbf{V}_i$ and the electron drift velocity is $\mathbf{V}_e$. The pressure tensor for each species is assumed to be diagonal and isotropic, so for the ions we have $\mathbf{P}_i = (n_i k T_i)\mathbf{I} = p_i \mathbf{I}$, and we have $\mathbf{P}_e = (n_e k T_e)\mathbf{I} = p_i \mathbf{I}$ for the electrons where $\mathbf{I}$ is the unit dyadic.

The continuity equation for a given ion species is:

$$\frac{\partial n_i}{\partial t} + \nabla \cdot (n_i \mathbf{V}_i) = P_i - L_i n_i \tag{2.6}$$

In the above equation, $P_s$ and $L_s$ are production and loss terms that depend on photoionization, radiative recombination, and chemistry. The continuity equation is solved for the following ion species: $H^+$, $He^+$, $O^+$, $O_2^+$, $N^+$, $N_2^+$, and $NO^+$. Note that the plasma is assumed to be quasi-neutral, so the electron continuity equation is not solved; instead the electron density is determined by summing the densities of each ion species.

The momentum equation is solved for both the ions and the electrons, but the electron momentum equation is simplified by neglecting the electron inertia due to the small electron mass. In addition, the electron collisional terms are neglected

as the electron collision frequency, $\nu_e$, is much smaller than the electron cyclotron frequency, $\omega_{ecf}$. The resulting equation for electron momentum is:

$$0 = -\frac{1}{n_e m_e}\nabla \mathbf{P}_e - \frac{e}{m_e}\mathbf{E} - \frac{e}{m_e c}\mathbf{V}_e \times \mathbf{B} \tag{2.7}$$

The ion momentum equation, solved for the seven ion species ($H^+$, $He^+$, $O^+$, $O_2^+$, $N^+$, $N_2^+$, and $NO^+$) is as follows:

$$\frac{\partial \mathbf{V}_i}{\partial t} + \mathbf{V}_i \cdot \nabla \mathbf{V}_i = -\frac{1}{\rho_i}\nabla \mathbf{P}_i + \frac{e}{m_i}\mathbf{E} + \frac{e}{m_i c}\mathbf{V}_i \times \mathbf{B} + \mathbf{g} - \nu_{in}(\mathbf{V}_i - \mathbf{V}_n) - \sum_{j \neq i} \nu_{ij}(\mathbf{V}_i - \mathbf{V}_j) \tag{2.8}$$

where $\nu_{in}$ is the ion-neutral collision frequency, $\nu_{ij}$ is the ion-ion collision frequency and the summation is done for ion species $j \neq i$.

The temperature equation is solved for the following three ion species: $H^+$, $He^+$ and $O^+$. The temperature for the remaining ions is assumed to be equal to the $O^+$ temperature.

$$\frac{\partial T_i}{\partial t} + \mathbf{V}_i \cdot \nabla T_i + \frac{2}{3} T_i \nabla \cdot \mathbf{V}_i + \frac{2}{3}\frac{1}{n_i k}\nabla \cdot \mathbf{Q}_i = Q_{in} + Q_{ij} + Q_{ie} \tag{2.9}$$

The terms on the right-hand side of the equation are heating terms that are due to ion-neutral collisions ($Q_{in}$), ion-ion collisions ($Q_{ij}$), and ion-electron collisions ($Q_{ie}$). The $k$ on the left-hand side of the equation is the Boltzmann constant. The $\mathbf{Q}_i$ term is the heat flux, which can be defined as $\mathbf{Q}_i = -\kappa_i \nabla T_i$. Here, $\kappa_i$ is the thermal conductivity. Since the thermal conductivity primarily only occurs along the magnetic field line, the heat flux term can be reduced to:

$$\nabla \cdot \mathbf{Q}_i \simeq -b_s^2 \frac{\partial}{\partial s}\kappa_i \frac{\partial T}{\partial s} \tag{2.10}$$

where $s$ is a coordinate along the magnetic field line and $b_s$ is the component of the magnetic field in the field line direction.

The temperature equation is also solved for the electrons with the assumption that $\mathbf{V}_e = 0$:

$$\frac{\partial T_e}{\partial t} + \frac{2}{3}\frac{1}{n_e k}\nabla \cdot \mathbf{Q}_e = Q_{en} + Q_{ei} + Q_{phe} \tag{2.11}$$

The terms on the right-hand side of the equation are heating/cooling terms associated with electron-neutral collisions ($Q_{en}$), electron-ion collisions ($Q_{ei}$), and photoelectron heating ($Q_{phe}$). The second term on the left-hand side is a diffusion term, which can be simplified similarly to the term in the ion equation so that:

$$\nabla \cdot \mathbf{Q}_e \simeq -b_s^2 \frac{\partial}{\partial s}\kappa_e \frac{\partial T}{\partial s} \tag{2.12}$$

where $\kappa_e$ is the parallel electron thermal conductance.

There is physical feedback that occurs between the electric fields in the ionosphere, the ionospheric conductivites, and the neutral winds. In order to calculate the $\mathbf{E} \times \mathbf{B}$ drifts self-consistently, it is necessary to calculate the electric field. For time scales longer than about 1 minute, the electric field can be assumed to be electrostatic: $\mathbf{E} = -\nabla\Phi$. Then the potential equation can be derived from the assumption of current conservation: $\nabla \cdot \mathbf{J} = 0$, which is valid for time scales longer than about 1 second. The electric potential can be assumed to be constant along the magnetic field lines due to the high conductivity of the ionosphere along the geomagnetic field. This allows us to express the equation as a two-dimensional function that varies perpendicularly to the field lines. This assumption starts to break down below about 100 km altitude. The full equation and terms are described in detail

in reference literature [22]. The electric potential equation used in SAMI3/ESF in dipole coordinates is:

$$\frac{\partial}{\partial p}\Sigma_{pp}\frac{\partial \Phi}{\partial p} - \frac{\partial}{\partial p}\Sigma_H\frac{\partial \Phi}{\partial \phi} + \frac{\partial}{\partial \phi}\frac{1}{p}\Sigma_{p\phi}\frac{\partial \Phi}{\partial \phi} + \frac{\partial}{\partial \phi}\Sigma_H\frac{\partial \Phi}{\partial p} = \frac{\partial F_{pV}}{\partial p} + \frac{\partial F_{\phi V}}{\partial \phi} - \frac{\partial F_{pg}}{\partial p} + \frac{\partial F_{\phi g}}{\partial \phi} \tag{2.13}$$

Here $p$ and $\phi$ are dipolar coordinates. The $\Sigma$ represent the field line integrated Hall and Pedersen conductivities:

$$\Sigma_{pp} = \int (p\,\Delta/b_s)\sigma_p\,ds; \quad \Sigma_{p\phi} = \int (1/p\,b_s\Delta)\sigma_p\,ds; \quad \Sigma_H = \int \sigma_H/b_s\,ds \tag{2.14}$$

where $\sigma_P$ is the Pedersen conductivity, $\sigma_H$ is the Hall conductivity, $\sigma_{Pi}$ is the ion component of the Pedersen conductivity, $\sigma_{Hi}$ is the ion component of the Hall conductivity, $\Delta = (1+3cos^2\theta)^{1/2}$, here $b_s = (r_E^3/r^3)\Delta$, and $r_E$ is the radius of the Earth. The integration is performed along the magnetic flux tube in the $s$ direction.

The $F$ terms are integrated functions of the gravitational force and neutral wind velocities along the field line:

$$F_{pV} = \int (B_0/c)\,r sin\theta\,(\sigma_P V_{n\phi} + \sigma_H V_{np})ds \tag{2.15}$$

$$F_{\phi V} = \int (B_0\,r_E\,sin^3\theta/c\Delta)(-\sigma_P V_{np} + \sigma_H V_{n\phi})ds \tag{2.16}$$

$$F_{pg} = \int r sin\theta\,(B_0/c\,\Omega_i)\,\sigma_{Pi}\,g_p\,ds \tag{2.17}$$

$$F_{\phi g} = \int (r_E\,sin^3\theta/\Delta)(B_0/c)(1/\Omega_i)\,\sigma_{Hi}\,g_p\,ds \tag{2.18}$$

For the purposes of this dissertation, we neglect the background global neutral wind dynamo and only consider the local wind dynamo.

In order to solve the above equations, a time splitting scheme is used. First, the equations are solved for motion along the geomagnetic field, then they are solved

for motion perpendicular to the geomagnetic field. This approach allows for the equations to be solved as long as a relatively small time step ($\sim 1 - 12$ seconds) is used.

## 2.2 HF Propagation

The ionosphere was originally discovered by radio engineers who were researching HF radio wave propagation. They realized the HF signals must be reflected from an ionized layer of gas and called that layer the ionosphere. While the ionosphere enables some HF propagation such as HF communications and Over-The-Horizon Radar (OTHR), it hinders others such as GPS signals. The ionosphere is the most variable part of the atmosphere; large and small scale perturbations can potentially disrupt HF signals that we use for communication, navigation and surveillance. At high latitudes, geomagnetic storms can cause severe disruptions, but there are a number of quiet time disruptions such as Equatorial Spread F (ESF) and Traveling Ionospheric Disturbances (TIDs) that can also severely affect HF communication at lower latitudes. HF radio waves are also used as a heating source for artificial ionospheric modification, which are used for diagnostics and provide additional insight into ionospheric processes.

In this section, the basic physics of radio wave propagation in the ionosphere is outlined. Next an ionospheric raytracing model, MoJo (Modernized Jones Code), that models the propagation of the radio waves through the ionosphere is described. Finally a brief summary of the physical processes that result in artificial heating of

the ionosphere by radio waves is provided.

### 2.2.1 Basic Physics

Radio wave propagation through the ionosphere is highly dependent on the local electron density, collision frequencies, and the density gradients. The ionosphere acts as a nonuniform, anisotropic, lossy dielectric medium. It is nonuniform because the density of the ionosphere varies as a function of position, thus so does the index of refraction for a radio wave in the ionosphere. For HF waves, the electrons in the ionosphere are affected by the wave, whereas the ions are too heavy to respond; thus it is the electron density that is important. The vertical electron density gradients are the most important to consider for radio wave propagation, as this determines the reflection altitude. We will see in Chapter 3, however, that while the vertical gradient is the most important, horizontal gradients can also significantly impact HF propagation. The anisotropy of the ionosphere is due to the fact that it is immersed in the Earth's geomagnetic field. The modes of an electromagnetic wave that can propagate in a plasma are highly dependent on the direction of the wave normal to the magnetic field direction.

Important quantities for the calculation of radio wave propagation in the ionosphere include: the background electron density, the direction and strength of the background geomagnetic field, the wave vector and the wave electric field, and the electron neutral and electron ion collision frequencies. The theory of how a radio wave propagates in a cold, magnetized plasma was worked out in the early 20th cen-

tury by a number of scientists including E. V. Appleton, D. Hartree, H. K. Lassen, and K. G. Budden [5]. A full description of the physics of radio wave propagation can be found in the reference literature. C. B. Haselgrove and J. Haselgrove pioneered the implementation of the equations on a computer that allowed for scientists to calculate the path of a radio wave through the ionosphere [17].

The primary equation that controls the propagation of electromagnetic waves involves the index of refraction of the radio wave in the ionosphere. The equation describing it can be derived from the linearized fluid and Maxwell equations with the assumption that the plasma is cold ($T_e = 0$). A complete derivation is given by [5]. The equation for the index of refraction is:

$$n^2 = 1 - 2X \frac{1 - iZ - X}{2(1 - iZ)(1 - iZ - X) - Y_T^2 \pm \sqrt{Y_T^4 + 4Y_L^2(1 - iZ - X)^2}} \tag{2.19}$$

with X, Y, and Z are defined as follows:

$$X = \frac{\omega_p^2}{\omega^2}; \quad Y = \frac{\omega_{ecf}}{\omega}; \quad Y_T = Y \sin\psi; \quad Y_L = Y \cos\psi; \quad Z = \frac{\nu_e}{\omega} \tag{2.20}$$

Here $\omega = 2\pi f$ is the input angular wave frequency, $\omega_p$ is the plasma frequency, $\omega_{ecf}$ is the electron cyclotron frequency, $\nu_e$ is the electron collision frequency, and $\psi$ is the angle between the wave normal direction and the Earth's magnetic field.

There are two solutions for the index of refraction equation depending on whether one selects the '+' or the '−' in the equation. The solution for the '+' is called the ordinary mode, or the O-mode, and it corresponds to HF waves emitted from a transmitter with the wave electric field parallel to the ambient magnetic field and is also known as Left Hand Circularly Polarized (LHCP). It is called ordinary because the solution is the same as the solution given in the absence of a background

magnetic field. Note that this is not the same as the O wave defined in cold plasma wave theory, which is actually a special case of this mode for parallel propagation to the magnetic field. In the O-mode, the index of refraction goes to zero when $\omega = \omega_p$, a cutoff point; thus, the wave will reflect at the altitude where the plasma frequency is equal to the input wave frequency. For oblique propagation, however, the reflection condition is $\omega = \omega \cos\theta$, so the ionosphere can reflect much higher frequencies.

Additionally, there is the extraordinary mode or X-mode, which is the solution with the '$-$' in the equation. This mode is not typically used for HF heating of the $F$-region, and it will not be addressed in this work, so its properties are only briefly outlined here. The X-mode corresponds to Right Hand Circularly Polarized (RHCP) HF waves, and there are two cutoff points at $X = 1 \pm Y$. In most cases the X-mode reflects before it reaches the cutoff point defined by $X = 1 + Y$, since the cutoff point defined by $X = 1 - Y$ is satisfied at a lower altitude. The lower altitude solution, $X = 1 - Y$, can be rewritten as $\omega_p/\omega = \sqrt{1 - \omega_{ecf}/\omega}$. Typically for HF propagation in the ionosphere we can assume that $Y < 1$, so $\omega_p/\omega \approx 1 - \omega_{ecf}/2\omega$ and the X-mode will reflect at the point where $\omega = \omega_p + \omega_{ecf}/2$.

An interesting characteristic of the O-mode vs. X-mode waves is the direction of the electric field at reflection. The O-mode electric field is parallel to the magnetic field at the reflection point, whereas the X-mode electric field is perpendicular. This can be seen in the propagation characteristics in Figure 2.3. The O-mode is refracted towards the magnetic pole and the X-mode is refracted away from it. It should also be noted that the O-mode reflects at a higher altitude than the X-mode,

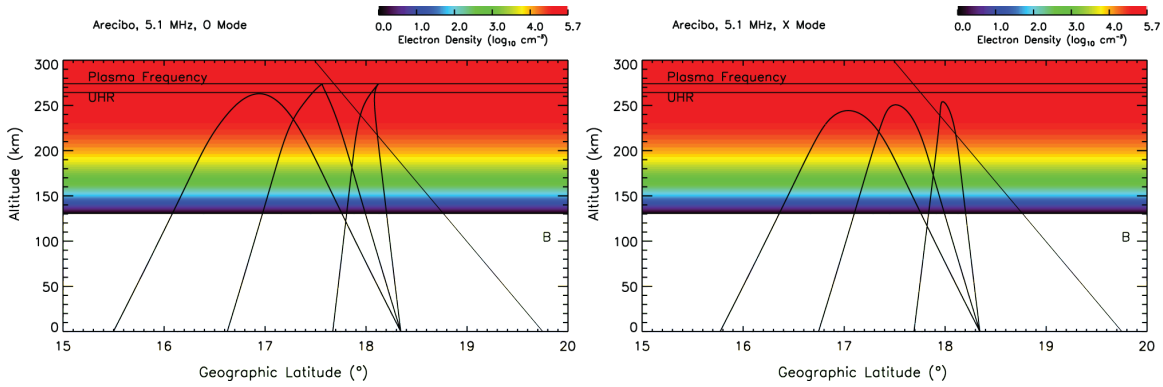


Figure 2.3: An example of raytracing through a simple Chapman layer at the location of the Arecibo Observatory in Puerto Rico. The left panel shows traces for the O-mode, the right for the X-mode.

specifically, only the O-mode wave reflects above the upper hybrid resonance where $\omega^2 = \omega_p^2 + \omega_{ecf}^2$; this fact will be important for artificial HF heating.

### 2.2.2 Modeling (MoJo)

MoJo (Modernized Jones Code) is a raytrace code based on a classical raytracing code [28]. While the code has been updated to take advantage of modern computational techniques, it retains the same general structure and equations as the original code. The general problem of raytracing is to follow the path of an HF electromagnetic wave through the ionosphere given a particular frequency, location and initial direction. In order to solve this problem, the general method is to numerically integrate Hamilton's equations, which define how the position of the wave and the wave propagation vector, $\mathbf{k}$, change along the ray path. In order to integrate the equations, at every point along the path, it is necessary to know the coordinates, the electron density and its derivatives, and also the magnetic field and

the collision frequency. Once these parameters have been determined, the derivatives of the equations are calculated and the numerical integrator propagates the ray forward along the path.

The numerical integration technique used in this work is the standard Runge-Kutta 4th order integration method, which is provided as a subroutine in the MoJo code. The variables that must be solved for via the numerical integration are the spherical coordinates of each point along the ray path (r, $\theta, \phi$), the propagation vector with components $k_r, k_\theta, k_\varphi$, which are normalized so that in free space ($k_r^2 + k_\theta^2 + k_\varphi^2 = \omega^2 n^2/c^2$), as well as the time (t) and the angular frequency of the wave ($\omega = 2\pi f$). Hamilton's equations (see Appendix A) describe the evolution of these quantities as a function of derivatives of the Hamiltonian. The Hamiltonian used here is as follows:

$$H = \frac{1}{2}\left(\frac{c^2}{\omega^2}(k_r^2 + k_\theta^2 + k_\varphi^2) - n^2\right) \tag{2.21}$$

Note that the Hamiltonian depends on the index of refraction, which is defined in the previous section.

In order to solve for the index of refraction and the Hamiltonian, it is necessary to know the input wave frequency, the mode (O-mode or X-mode), the electron density, the magnetic field and the collision frequency. Some of these quantities are specified as input; namely, the wave frequency and the wave mode. Other quantities, including the electron density, magnetic field, and collision frequency can either be specified as input fields, or default values provided by internal functions may be used.

For the electron density field, MoJo requires a fixed latitude, longitude, altitude grid. For the purposes of this dissertation, the electron density is provided by the SAMI3/ESF code output. An internal subroutine calculates the strength and direction of the magnetic field at a given location using a harmonic analysis. It is also required to define the collision frequency of the electrons with the ions and the neutral particles, which is a function of altitude. The collisions primarily serve as a source of absorption for the incoming EM wave and do not significantly impact the path of the wave through the ionosphere. This work does not consider collisional absorption, only the path of the ray; thus, any effects of the time, latitude or longitudinal variability of the collision frequency is negligible here and a simple collision frequency profile is used:

$$\nu_e = \nu_{en}/e^{A_{en}(z-z_{en})} + \nu_{ei}/e^{A_{ei}(z-z_{ei})} \tag{2.22}$$

where $\nu_{en} = 5 \times 10^{11} s^{-1}$ is the electron-neutral collision frequency at the reference height $z_{en} = 0$ km, and $A_{en} = 1/6.5 km^{-1}$ is the scale height for the electron-neutral collisions. For the electron-ion collisions: $\nu_{ei} = 1.0e3 s^{-1}$ is the electron-ion collision frequency at $z_{ei} = 200$ km and $A_{ei} = .01 km^{-1}$ is the scale height.

While the collision frequency and magnetic field can be calculated for random points along the ray's path, the electron density is provided in a fixed grid format, thus MoJo must use a cubic interpolator to determine the local electron density and its gradients. Further details of the MoJo ray trace code are discussed in Appendix A.

## 2.3 Artificial Modification

Early ionospheric research generally consisted of monitoring the ionosphere in its natural state. Such studies are still important, but sometimes it is difficult to interpret the driver behind certain ionospheric phenomena. Active experiments allow scientists to control the input mechanism and examine the result of interacting with the ionosphere. This provides further insight into the basic processes at work in the ionosphere. The scientists use large arrays of antennas that transmit high power density HF radio waves. The waves are strongly absorbed near the reflection altitude, which causes a large rise in the electron temperature and both linear and nonlinear effects such as turbulence. These types of experiments allow scientists to treat the ionosphere as an "open plasma laboratory". For diagnostics, the artificial heaters are supplemented by diagnostic instruments both on the ground and in space such as radars, magnetometers, etc.

The majority of artificial modification investigations have focused on middle to high latitudes because the operational radio wave heaters (HAARP, EISCAT, SURA) are located at magnetic latitudes above 40°. In the 1980s and 1990s, a number of scientific investigations were carried out at Arecibo, which is located at 28° magnetic latitude before the radio wave heater was destroyed by a 1998 hurricane. An updated heating facility is currently being installed at Arecibo, which should be available for experiments in the near future.

Artificial HF heaters exploit natural plasma oscillations in the ionosphere to increase the absorption of radio waves beyond the levels that are seen with typical

collisional absorption. Generally, most of the power from a radio wave is reflected from the ionosphere, with only about 5-10% of the power lost to collisions. In the case of anomalous absorption, described by Gurevich [16], as much as 95% of a incoming HF pump wave can be absorbed by the ionospheric plasma.

Anomalous absorption dominates in the altitude range between the upper hybrid height and the O-mode wave reflection point. The upper hybrid height, $z_{uh}$, is defined by the altitude where the HF pump frequency is equal to the upper hybrid resonance frequency $\omega = \omega_{uh} = [\omega_p^2(z_{uh}) + \omega_{ecf}^2]^{1/2}$. Here $\omega_{ecf}$ is the electron cyclotron frequency and $\omega_p$ is the electron plasma frequency at $z_{uh}$. The upper hybrid altitude is usually located 5-10 km below the O-mode reflection level, but it is above the X-mode reflection level, thus X-mode waves do not result in anomalous absorption. The upper hybrid frequency is associated with plasma oscillations that are perpendicular to the background magnetic field. When the HF pump wave passes through the upper hybrid altitude, the Upper-Hybrid Resonance (UHR) is established, which converts a significant portion of the wave energy to the plasma, pumping up the turbulence and raising the electron temperature.

After exciting resonances at the upper hybrid altitude, the pump wave continues to the O-mode reflection level, which occurs when $\omega = \omega_p$. At this altitude the component of the pump electric field that is parallel to the geomagnetic field increases, while the perpendicular components decrease. This swelling of the parallel electric field drives electrostatic plasma, or Langmuir, waves. The enlargement of the parallel electric field also contributes to other nonlinear processes that occur in this region, such as Langmuir turbulence.

The anomalous absorption of HF radio waves creates strong electron heating, which causes an increase in the electron temperature and pressure and forces the electrons to expand away from the heated regions. The ions initially do not move, as they are not strongly affected by the HF heating due to their large mass. The motion of the electrons, however, sets up a charge separation between the electrons and ions, which creates an ambipolar electric field and causes the plasma (both electrons and ions) to expand away from the heating zone. Due to the plasma expansion, a depletion, or cavity is formed in the local area of HF heating. These cavities will be studied extensively in Chapters 4 and 5.

# Chapter 3: The Role of 3D Electron Density Gradients on HF Propagation

One of the challenges for the utilization of HF radio waves in practical applications is to understand how the signals propagate in time- and range-dependent multipath environments. For typical quiescent ionospheric conditions, the interpretation of the received signal is relatively straightforward. More complicated ionospheric conditions with tilts and other irregularities, such as from Medium Scale Traveling Ionospheric Disturbances (MSTIDs), present significant challenges to data interpretation. MSTIDs distort the path of HF radio waves through the ionosphere, which results in large coordinate registration errors for OTHR (Over the Horizon Radar) systems that depend on a smooth ionosphere in order to accurately probe the surrounding environment. The MSTIDs also produce inaccuracies in HF geolocation services, which use the angle of arrival information of the radio waves to locate the source of the signal.

This chapter presents a modeling study that exploits the capabilities of a first-principles ionosphere code (SAMI3) and a 3D raytrace code (MoJo) in order to examine the relationship between various HF propagation observables and MSTID characteristics. First, the properties of MSTIDs and the current modeling capabil-

ities are described. Next, HF probing techniques are outlined. We briefly consider the importance of a 3D raytrace code compared to a 2D code. Then we demonstrate the implications of MSTIDS on high angle of incidence HF propagation during typical low-latitude, post-sunset ionospheric conditions and examine the spatiotemporal evolution of multiple propagation paths that may connect a given source and receiver. Finally we present a brief discussion and conclusions.

## 3.1 Medium Scale Traveling Ionospheric Disturbances (MSTIDs)

Traveling Ionospheric Disturbances (TIDs) are common in the ionosphere and have been detected for many decades. The understanding and prediction of TIDs is vital for a variety of HF applications, as the disturbances create large disruptions to HF geolocation services and introduce large uncertainties into coordinate registration for OTHR systems. The typical TIDs manifest as propagating density perturbations near the $F$-peak height that are organized into bands at an angle to the magnetic equator. They are usually classified according to their speed and size. In general, larger scale TIDs have longer wavelengths, longer periods and faster propagation speeds. Medium Scale TIDs (MSTIDs), which are of interest for this work, typically have a period somewhere in the order of 10-60 minutes, and wavelength on the order of 100 km [14, 51]. MSTIDs are typically a midlatitude phenomenon, but they can be generated in the auroral region and subsequently propagate to lower latitudes. The signatures of TIDs can be found in both airglow imaging and Total Electron Content (TEC) data. Figure 3.1 shows an example of

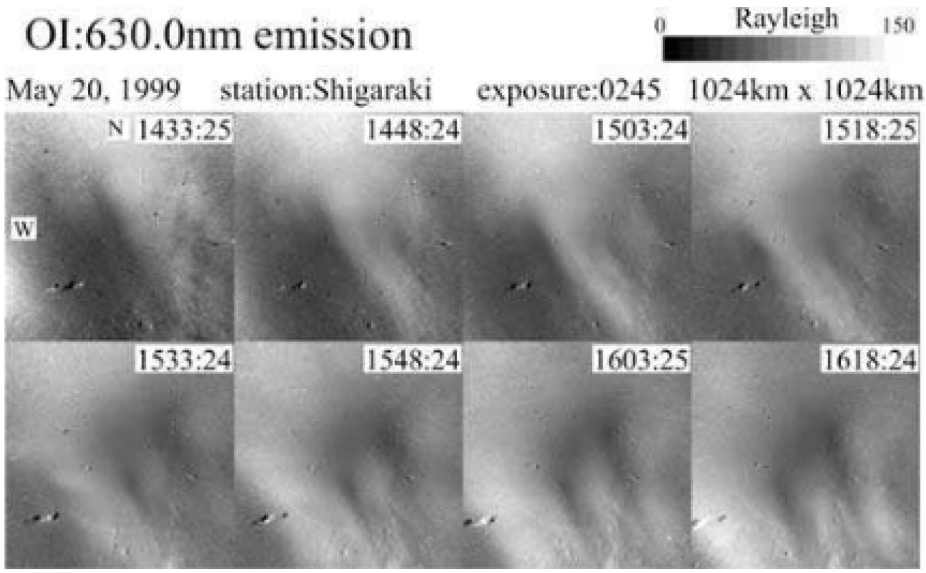


Figure 3.1: A sequence of 630.0 nm airglow images showing an MSTID propagating in the nighttime at middle latitudes. As time progresses the density bands move southwest. (Reproduced from [51])

a propagating MSTID as seen from airglow imaging.

A particular type of MSTID is an "electrodynamic" MSTID, similar to a typical MSTID, but associated with changes in the electric field. The $\mathbf{E} \times \mathbf{B}$ drifts of the plasma from the electric field result in the formation of perturbed density bands that travel at speeds of approximately 100 m/s. In the northern hemisphere, the waves propagate southwest towards the equator with the wave fronts typically aligned from northwest to southeast. These types of perturbations typically occur late at night or after midnight at low- and midlatitude. Since they carry an electric field and the conductivity along the magnetic field line is very large, they often have a signature in the conjugate hemisphere.

The electrodynamic MSTID is generally believed to be created by the so-

called Perkins instability. The night time $F$-region is supported by the force balance between the gravitational effects and electric field forces. The Perkins instability [46] results when the equilibrium is upset by a north-south component of the electric field. Recent modeling studies, however, indicate that the growth rate for the Perkins instability is slow, so while it clearly is a contributing factor it cannot fully account for the generation of MSTIDs in the ionosphere [11]. It has been suggested that gravity waves are responsible for triggering the instability and increasing the growth rate above the nominal Perkins instability growth rate [8].

The mechanisms for TID generation in the ionosphere are not yet fully understood, and modeling the structures from first principles is an ongoing area of research. Two very recent studies have provided the first examples of TID generation from first principles in a 3D ionospheric model. The first method demonstrated that the addition of random perturbations to the local Pedersen conductivity resulted in an MSTID-like structure with modes that are consistent with the Perkins instability [11]. The other study successfully generated an MSTID by adding gravity wave perturbations to the neutral winds in order to simulate the ionospheric response to a tsunami [26].

While the ionospheric community has had recent success in first principles modeling, the scientists investigating the effects of MSTIDs on HF propagation typically use a simpler approach to model MSTID structures. Generally, a background electron density field is assumed without any horizontal gradients; the vertical gradients are either determined using a simple model or ionosonde measurements. A horizontal perturbation in the shape of an MSTID is subsequently superimposed on

the background electron density field. In some cases a simple Gaussian perturbation is assumed, but recently the Hooke model has become popular since the model is consistent with forcing from gravity waves [19]. Since the vertical electron density gradient is the primary factor that determines the path of HF radio waves through the ionosphere (including the reflection altitude), this is a reasonable first approximation and also has the advantage of simplicity. It does not, however, account for background horizontal gradients in the ionosphere, such as the density gradient in the latitudinal direction due to the equatorial anomaly. Such models also fail to self-consistently account for the spatio-temporal evolution of the MSTID.

To generate a realistic MSTID for this work, a traveling sinusoidal in-situ electric field is added to the SAMI3/ESF ionosphere model during the calculation of the $\mathbf{E}\times\mathbf{B}$ drift [33]. While this method does not model the MSTID from first principles, the evolution of the MSTID in space and time is calculated self-consistently using SAMI3/ESF, which is a significant advance over simple, superimposed MSTID models. In addition, the parameters of the MSTID can be well controlled by altering the shape of the traveling-wave electric field. The in-situ wave-driven electric field is defined in terms of the vertical (p) and horizontal (h) directions as:

$$(\mathbf{E}_{TID} \times \mathbf{B})_{[p,h]} = -U_{TID} \frac{k_{[x,y]}}{k} \sin(k_x x + k_y y - \omega t) \tag{3.1}$$

Here, x and y are Cartesian coordinates corresponding to the longitudinal and latitudinal directions, respectively. The wavenumbers $k_x$ and $k_y$ are defined as $k_x = k \cos\theta_{TID}$ and $k_y = k \sin\theta_{TID}$. The magnitude of the wavenumber vector,

$\mathbf{k}$, is defined as $k = \frac{2\pi}{\lambda}$, where $\lambda$ is the wavelength. The propagation angle, $\theta_{TID}$ is defined as the angle between $\mathbf{k}$ and the magnetic equator. A propagation angle of 0° is equivalent to a bearing of -90°, which implies propagation parallel to the equator and crests that are aligned with the magnetic field. A propagation angle of 90° (or bearing of -180°) implies propagation perpendicular to the equator. We set the maximum $\mathbf{E} \times \mathbf{B}$ drift amplitude ($U_{TID}$) to 50 m/s, the wavelength to 250 km, the period to 1 hour, and the propagation direction to southwestward.

As in other SAMI3/ESF studies, the simulation is initialized using output from SAMI2, in this case, for day of year 80 (equinox). The $F_{10.7} = F_{10.7a} = 150$, and the Ap = 4. The longitudinal extent of the simulation is 4°, and it is centered on 0°. The SAMI3/ESF simulations consider the ionosphere's evolution, starting at 19:30 Local Time (LT), which is after the lifting of the $F$-layer by the pre-reversal enhancement; and ends at 20:30 LT. Snapshots of the time evolving 3D electron density field are saved at 1 minute intervals for the HF propagation calculations. Three different SAMI3/ESF simulations were run that only differed in the MSTID parameters. The first of these is the control that does not have an MSTID perturbation. The second simulation includes an MSTID with a bearing of -110° ($\theta_{TID} = 20°$) and the third a bearing of -140° ($\theta_{TID} = 50°$).

Figure 3.2 shows the electron density as a function of altitude at 10° latitude and 0° longitude at different times for each of the three simulations. The height of the peak density is around 480 km altitude and falls slightly during the hour. The peak density ranges from about $2.9 \times 10^6/\text{cm}^3$ to $3.1 \times 10^6/\text{cm}^3$, which corresponds to a critical frequency range of about 15-16 MHz. The profiles from the three

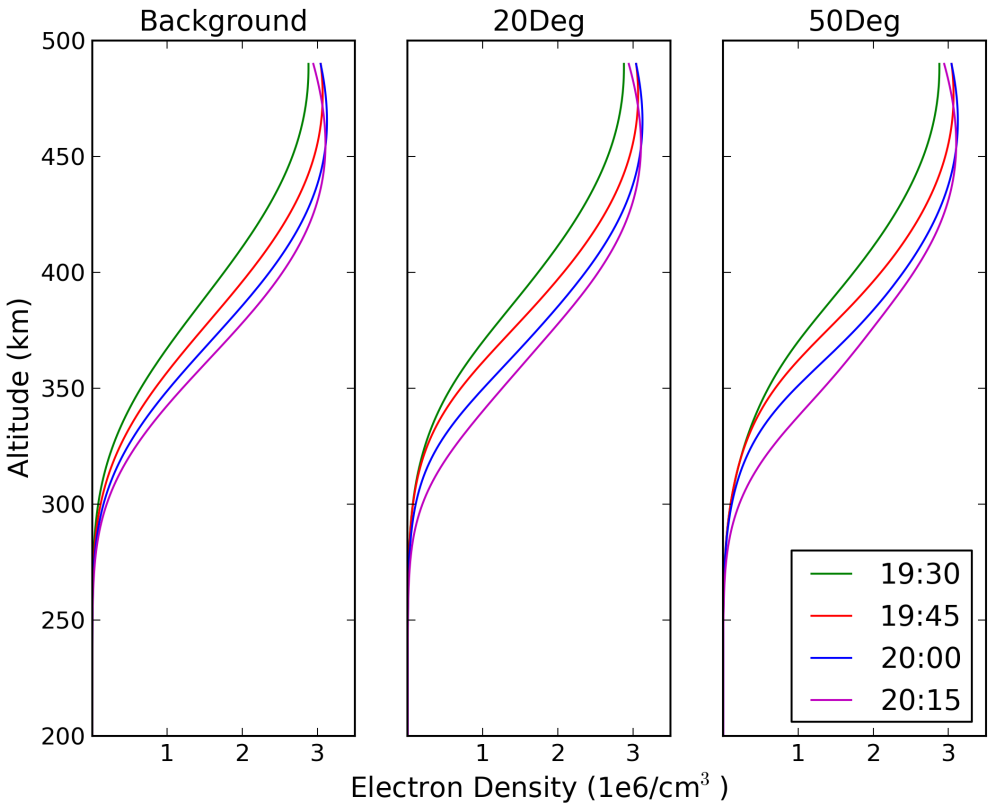


Figure 3.2: Electron density as a function of altitude at 10° latitude and 0° longitude for 4 different times during each simulation. The left panel shows the background case (no MSTID). The other two panels show cases with MSTIDs; the middle panel shows an MSTID with a -110° bearing, the right panel MSTID has a -140° bearing.

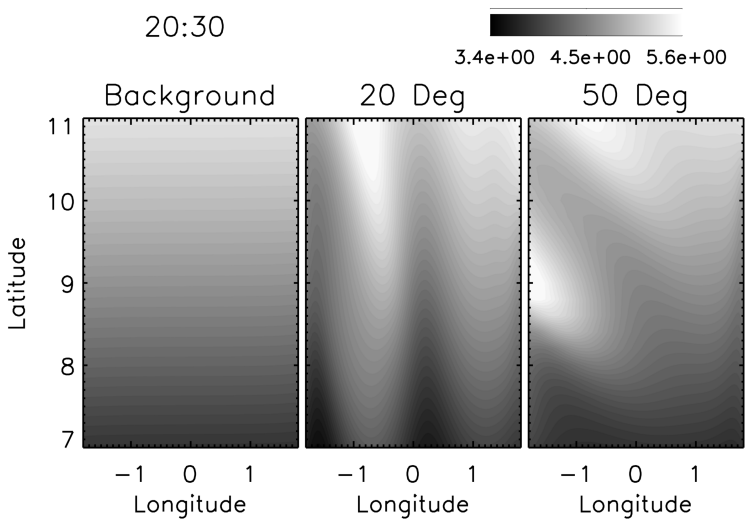


Figure 3.3: Electron density as a function of latitude and longitude at 290 km altitude. The left shows the background case, the center shows the MSTID with bearing -110°, the right shows the MSTID with bearing -140° .

different simulations are qualitatively very similar. This is because the MSTID primarily creates horizontal gradients rather than simply modifying the electron density profiles. As will be shown, the horizontal gradients in electron density resulting from the presence of MSTIDs are responsible for significant changes in the HF propagation path from a given source to a given receiver.

Figure 3.3 shows the ($log_{10}$) electron density at 290 km altitude as a function of latitude and longitude. The background case (left) has a slight gradient in the latitudinal direction, but it is fairly smooth and much less pronounced than the horizontal gradients introduced by the MSTID simulations. The -110° bearing case (center) has gradients in both directions, but the largest horizontal gradients are in the longitudinal direction. In the -140° bearing case (right) the large horizontal gradients

are at an angle. Note that in both of the MSTID cases, the minimum/maximum of the density crests are lower/higher than in the background case. In addition, the horizontal gradients are a much smaller scale than the background case.

## 3.2 HF Probing Techniques

A radar transmitter sends out High Frequency (HF) radio waves into the ionosphere. A receiver can identify two types of scatter: scatter from the irregularities in the ionosphere and backscatter that results from the reflection of the signal from the ground, which is often referred to as ground clutter. Early understanding of the influence of TIDs on HF propagation was obtained by examination of the ground backscatter observed by Over-the-Horizon-Radars (OTHR). A study in 1969 presented some of the first evidence that OTHR observables could provide information to better understand TID phenomena [15]. This early study, however, neglected the effects of the magnetic field. The idea was later revisited and it was established that TID parameters could be estimated from the backscatter signature using 2D ray-tracing [4]. Soon after, another possible method for using the backscatter signature to determine properties of TIDs was demonstrated, but the method neglected the effects of the magnetic field [52].

While examining radar observables from ground clutter has advanced our understanding of the effect of MSTIDs on HF radio waves, the reflection of the radio wave on the ground introduces clutter to the received signal, which complicates the signal interpretation. Thus, more recent studies often examine HF propagation ob-

servables from radio waves that propagate through the ionosphere from a transmitter to a receiver without reflecting off of the ground. This type of ionospheric probing is called monostatic if the transmitter and receiver are co-located and bistatic if they are not.

Multiple quantities can be measured at a receiver, but a particularly common measurement is the time delay of the signal from the transmitter. Generally, this time delay is multiplied by the speed of light in a vacuum ($c$); it then represents the group path length of the received signal through the ionosphere. Often the group path length is divided by 2, since we assume that the signal propagates up into the ionosphere and then reflects back down to the receiver; in this case it is called the virtual height. If the transmitted signal is swept through a series of frequencies, then one can plot the virtual height as a function of frequency. For monostatic probing this type of plot is referred to as an ionogram. For bistatic probing, if the transmitter and receiver are separated by a short distance ($\sim$ 100 km), then it is referred to as a Quasi Vertical Ionogram (QVI). Figure 3.4 shows an example QVI during a quiet period at 20:10 LT. The blue trace is for the O-mode signal, the red trace is for the X-mode signal. Other possible observables at the receiver are the doppler shift of the signal, the polarization of the received signal and the angle of arrival.

One early study of that used monostatic probing to understand the influence of TIDs on HF radio wave propagation demonstrated that the "U-shaped" features that sometimes overlap the main trace of ionograms are the result of horizontal gradients in the ionosphere resulting from MSTIDs [36]. These horizontal gradients

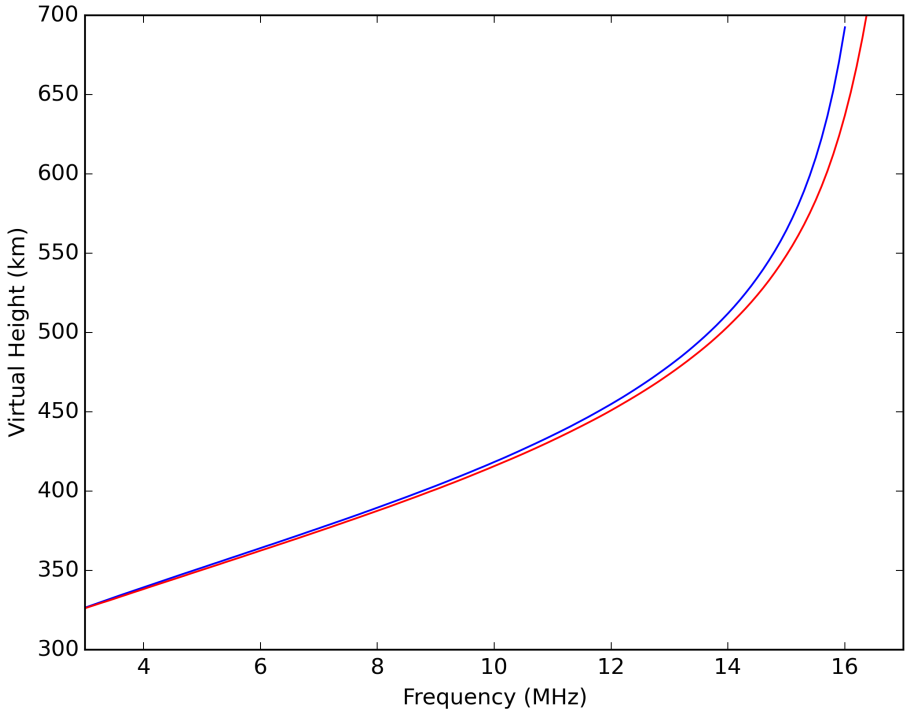


Figure 3.4: Example QVI during a quiet period at 20:10 LT. The O-mode trace is in blue, the X-mode trace is in red. The transmitter is located at 10.5° latitude, 0.0° longitude and the receiver at 9.5° latitude and 0° longitude.

from MSTIDs result in multipath propagation (i.e. more than one ray path connects the receiver and the transmitter at a given frequency), which leads to multiple traces on the ionogram. While they were able to successfully calculate multipathing that occurs during the passage of an MSTID, their model was 2D and the effect of the magnetic field was neglected. In addition, for the TID perturbation, they assumed a very simple Gaussian-perturbed parabolic layer, such that gradients in the background ionosphere were neglected and the TID did not evolve self-consistently with the background ionosphere.

A more recent study used bistatic probing to examine the influence of TIDs on QVIs utilizing a detailed 3D ionospheric raytrace code, which also includes the effects of the magnetic field [6]. Prior to this work, it was typically assumed that HF radio waves did not deviate significantly from the initial great-circle-path plane between source and receiver, justifying the use of 2D raytrace calculations. Importantly, however, it was demonstrated that a 3D raytrace calculation is actually required to accurately explain typical TID disturbance features observed in QVIs. The study did make a few simplifying assumptions. In particular they utilized the Hooke model [19] to represent the TID perturbations, so background ionospheric gradients were neglected and the time evolution of the ionosphere was simply determined by an analytic sinusoidal function. In addition, the ionospheric gradients in the cross-track range, perpendicular to the propagation direction, were neglected.

For this work the raytrace code MoJo is used. MoJo integrates the 3D Haselgrove HF raytrace equations [17] in spherical 3D coordinates, assuming the Appleton-Hartree Dispersion relation with collisions. The code takes into account the Earth's

magnetic field and uses a 4th-order Runge-Kutta scheme. The gradients of the electron density and magnetic field are calculated in all three directions for the Jacobian of the raytrace equations at every step of the numerical integration. Although MoJo can also do this for the electron collision frequency, for the calculations herein only an altitude-dependent electron collision frequency model is used for simplicity.

One major feature of MoJo (not included in the original Jones and Stephenson code) is the capability to quickly calculate exact eigenrays to machine precision via the non-linear Levenburg-Marquard algorithm, given a reasonable first guess of azimuth and elevation for a fixed frequency and propagation mode (O or X). If only one eigenray exists connecting the source and receiver MoJo will always find this ray. When multi-eigenrays exist, i.e. in a multipath environment, the algorithm will only find the closest eigenray to the initial guess. Figure 3.5 shows an example of eigenrays that connect a given transmitter and receiver for three different frequencies (dark lines). The lighter lines show that variations in the launch elevation angle change the location where the ray reaches the ground.

In very complicated multipath environments it is a nontrivial problem to quickly identify and locate every possible eigenray; particularly in time-evolving environments. The simplest brute force approach is to integrate a very dense distribution of rays over an extended domain of azimuths and elevations and identify any clusters of rays that land within some tolerance distance, $\sim$O(1 km), from the receiver. In a more elegant approach, a recent paper integrated a tessellated triangular mesh of rays and identified those triangles with landing points that encompass a given receiver [6].

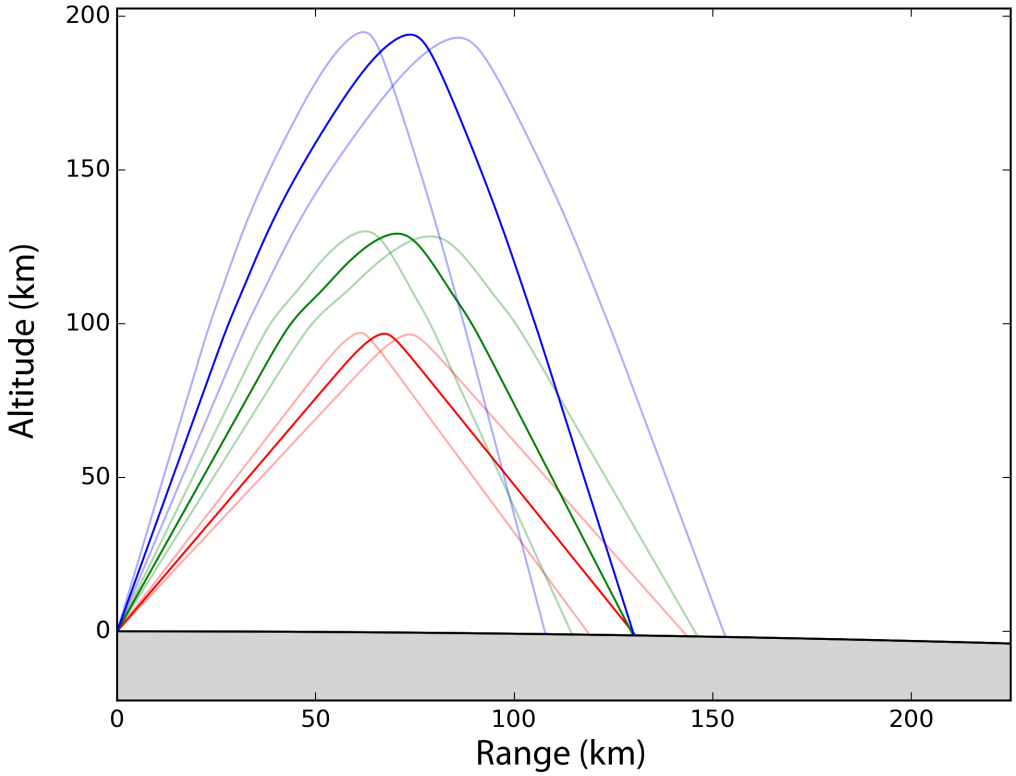


Figure 3.5: The dark lines show the ray paths for three different frequencies through a given ionosphere from a transmitter to a receiver that is approximately 130 km away. The lighter lines show near misses from the homing algorithm.

Here a novel technique to elucidate how MSTIDs warp all possible propagation paths from a given transmitter to the set of all possible ground receiver locations is presented. In this technique a series of euler rotations is applied to a linear 2D ray fan such that the 2D ray fan is swept at regular angular intervals away from the zenith; first in the north-south direction and after a 90° rotation in the east-west direction. For example, in Figure 3.6, one of the purple fans is pointed directly overhead for the east-west direction, the other purple fan is pointed directly overhead for the north-south direction. In both cases the azimuths of the initial rays are 90° and vary with elevation from 55° to 125°. The third fan in Figure 3.6 (shown in blue) is a north-south fan with an initial azimuth of 75°. Note that the red dot indicates the position of the transmitter and the lines at 0 km altitude illustrate the landing points of the ray fan.

A spherical distribution of rays over regular azimuth and elevation intervals maps to a series of concentric circles and radial lines, which can be potentially offset from the transmitter due to ionospheric tilts and magnetic inclinations. The series of tilted linear 2D ray fans maps to a nearly orthogonal rectangular grid of landing points in the region surrounding the transmitter, assuming that no significant ionospheric gradients are present.

An example of this mapping is shown in the left panel of Figure 3.7, for the SAMI3/ESF ionospheric control case at 20:10 UT, where a hypothetical transmitter broadcasting at 3.125 MHz with O-mode polarization is located at 10.5°N, 0.0°E (indicated by the red dot). Each line represents the landing points of the swept linear 2D rays over different beta angles from the zenith. In the control case, with

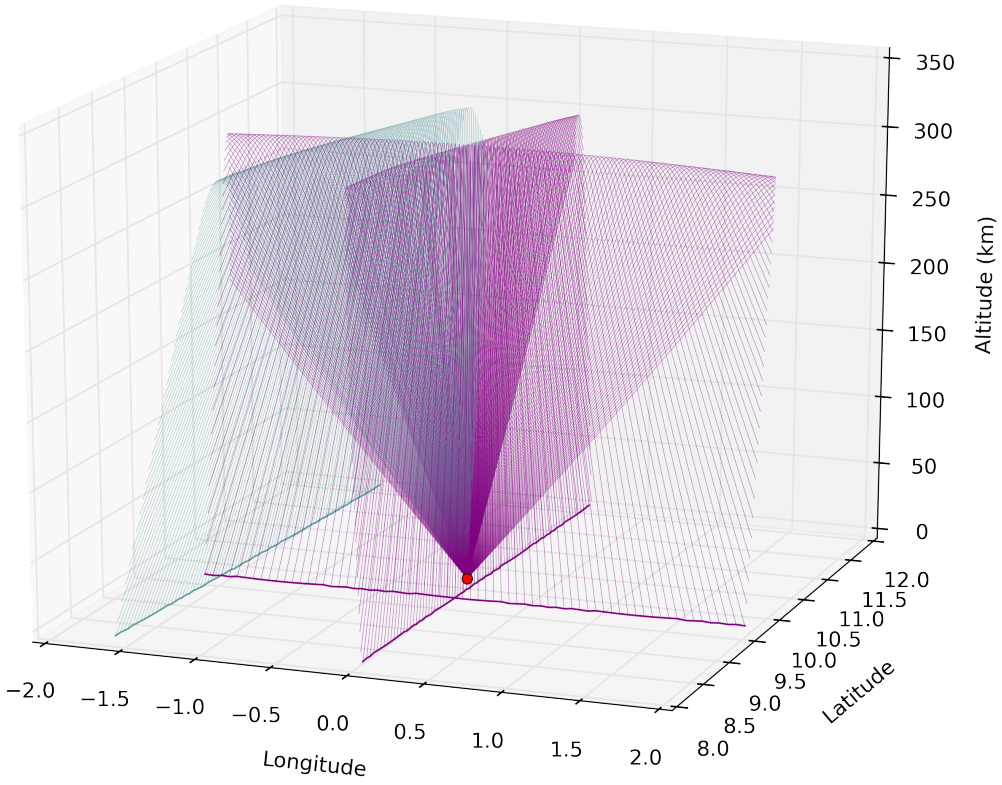


Figure 3.6: Three example ray fans that are used to generate the grid mesh pattern on the ground. The two purple ray fans have initial azimuths of 90°; one is in the north-south direction, one is in the east-west. The blue fan has an initial azimuth of 75°. The thick lines at 0 km altitude indicate the landing position of the ray fan on the ground.

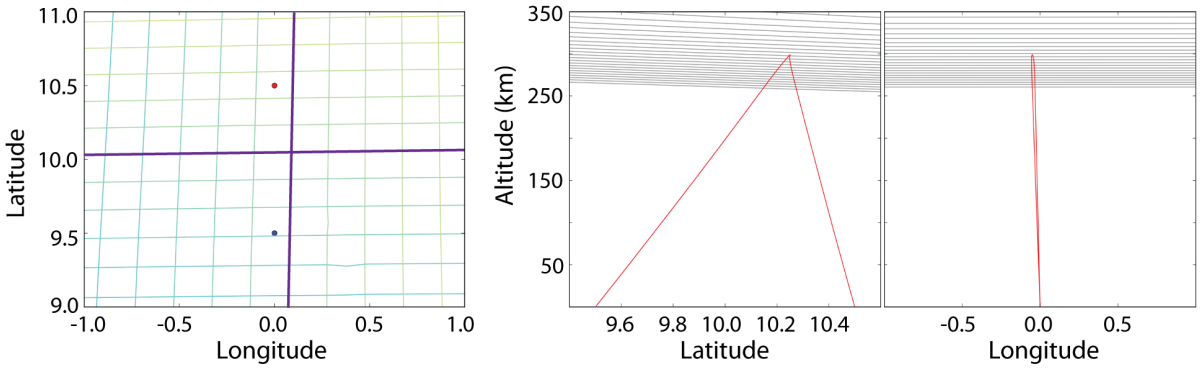


Figure 3.7: The left panel shows the landing point of 3.125 MHz O-mode waves launched in the square grid pattern at 20:10 for the background case. The transmitter (red dot) is at at 10.5° latitude, 0.0° longitude. The middle and right panels show the single ray launched from the transmitter that lands at a receiver located at 9.5° latitude and 0° longitude.

only global scale horizontal gradients, this results in a nearly orthogonal rectangular pattern. The landing location of the vertically incident east-west aligned ray fan is indicated by the horizontal purple line. It is located ∼0.5° southward of the transmitter, due to the magnetic inclination angle and the global scale ionospheric gradients (see Figure 3.3) in the control case. The vertical purple line indicates the landing location for the vertically aligned north-south ray fan. Again the landing locations are slightly offset from the transmitter location due to a slight magnetic declination in the ionospheric control case. It should be noted that at ranges much farther away from the transmitter (i.e., for very low transmission elevations) these lines eventually diverge as a result of the Earth curvature.

It should be apparent from this figure that for a hypothetical receiver located at 9.5°N, 0.0°E (blue dot), there is only one eigenray for 3.125 MHz O-mode propagation. The middle and right panels of Figure 3.7 show the path of the single

eigenray as a function of latitude and altitude (middle) and as a function of longitude and altitude (right). The grey contours indicate lines of constant electron density. In the middle panel there is a clear tilt in the latitude direction due to the global scale gradient. In the right panel there are no horizontal gradients in the longitude direction, but the eigenray is necessarily offset from the vertical due to the effects of the magnetic field (a slight declination), which is accounted for in MoJo15.

## 3.3 Deficiencies of 2D Models

For each of the three time-dependent 3D SAMI3/ESF simulations described in Section 3.1, MoJo-15 is used to calculate the time evolution of high-angle-of-incidence HF propagation during the passage of an MSTID. Before describing the main results regarding the time evolution of eigenrays, the effect of the presence of an MSTID on the east-west aligned vertical 2D ray fan is considered. The propagation of this ray fan through the different modeled ionospheres at 20:00 LT is shown in Figure 3.8. The left column shows the control case. As expected there is no significant ray bending or focusing, in this case, and the rays reflect uniformly at a height of $\sim$300 km altitude.

The center column of Figure 3.8 shows the results for the MSTID propagating with a bearing of -110°; here the effect of the MSTID-induced horizontal gradients are apparent. First, the rays reflect at different altitudes. Secondly, the longitude altitude panel shows focusing around 0°, often interpreted as a caustic, which we

expect for horizontal gradients. The latitude and longitudes of the landing points shown in the bottom panel, however, clearly illustrates that this focusing is a mirage. While a large number of rays land on the ground near 0°, they are dispersed in latitude, with offsets ranging from 9.5° to 10.5°N; or distances approaching nearly 100 km.

The right column shows the case for the MSTID propagating at a bearing of -140°. The effect of horizontal gradients is also clearly noticeable. The rays launched with negative azimuths (westward) reflect at a lower altitude than those launched with positive azimuthal angles. Again the rays deviate significantly from the original 2D plane of propagation.

Both of these examples highlight a potential limitation of 2D ray trace calculations, as well as 2D parabolic and full wave methods for accurately modeling HF skywave propagation in the presence of 3D ionospheric gradients. In both of the MSTID cases the rays deviate significantly from the initial plane, thus for example the group path delay would be underestimated with 2D raytracing. In addition, signal amplitudes would be overestimated in the regions of caustics for the -110° MSTID propagation case.

## 3.4 The Time Evolution of HF Observables During MSTID Propagation

This section describes the main results of the time evolution of the reflected high-angle-of-incidence HF propagation during the passage of an MSTID. The left

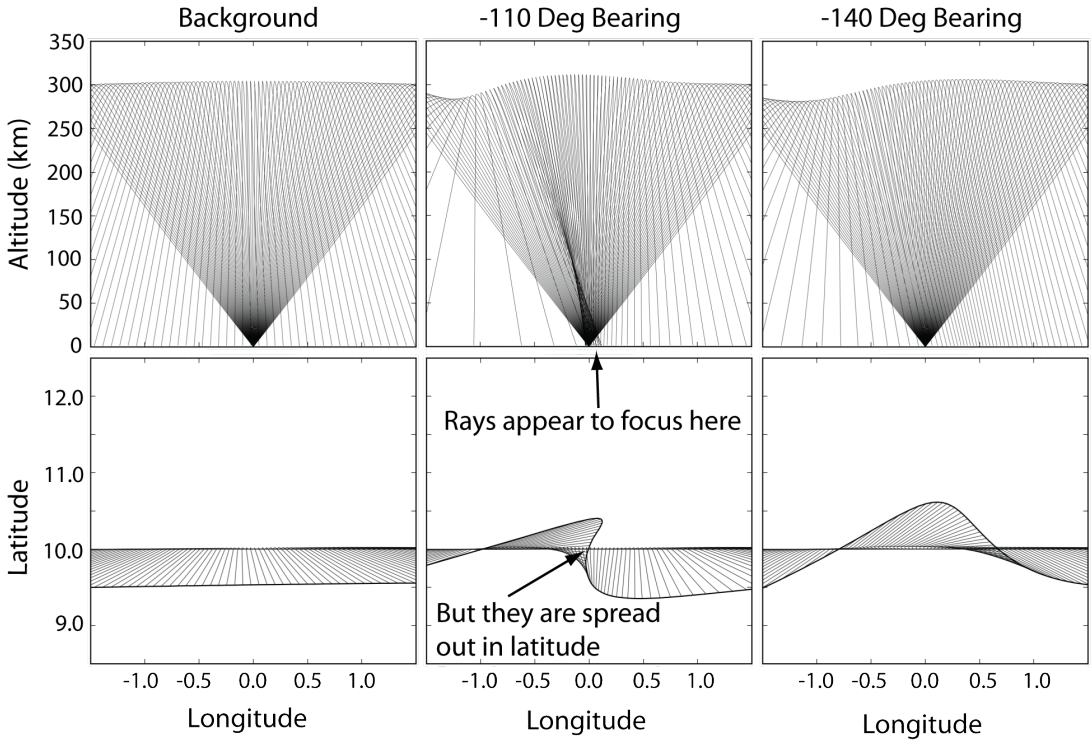


Figure 3.8: Ray paths from a single transmitter (3.125 MHz O-mode) as a function of longitude-altitude (top row) and longitude-latitude (bottom row) for each of the three simulations. The MSTID both show ray bending. The -110° bearing case appears to show focusing in the longitude-altitude plane (top, middle panel) around 0°, but the rays are actually spread out in latitude (bottom, middle panel).

column of panels in Figure 3.9 shows the effect of the -140° bearing MSTID's passage on the mapping of the reflected 3.125 MHz O-mode propagation paths at four different times. In this case, the MSTID-induced gradients in the ionosphere result in a strikingly different mesh pattern. Instead of a rectilinear grid, the mesh is warped and folds in on itself. In locations where the mesh is folded over, a triad of eigenrays exists as explained in earlier studies [7, 9]. The time series of maps shown in the first column reveals the prominent spatial aspects, as well as distinct time evolution of the MSTID-induced gradients on HF propagation. The middle column shows the eigenray paths as a function of latitude and altitude connecting the hypothetical transmitter and receiver at the four different times. The right column shows the same eigenrays over longitude and altitude. As before, the grey lines indicate the lines of constant electron density.

The first row corresponds to a simulation time of 20:00 LT. Although there are some horizontal gradients in the ionosphere associated with the approaching MSTID, there is still only one eigenray connecting the transmitter and receiver. Note that in the far left panel, the region of multipathing has not yet reached the location of the receiver. As compared to the control case shown in Figure 3.7, the location of the eigenray reflection point is shifted ∼0.5° westward and ∼0.5° southward; almost 70 km. This is almost as large as the wavelength of the specified MSTID. As noted by [7] this has important repercussions for the accuracy of HF Doppler sounding techniques to measure MSTID propagation velocity, wave period, and wavelength parameters, that rely upon the assumption that the HF Doppler sounding point occurs at the midpoint between the transmitter and receiver.

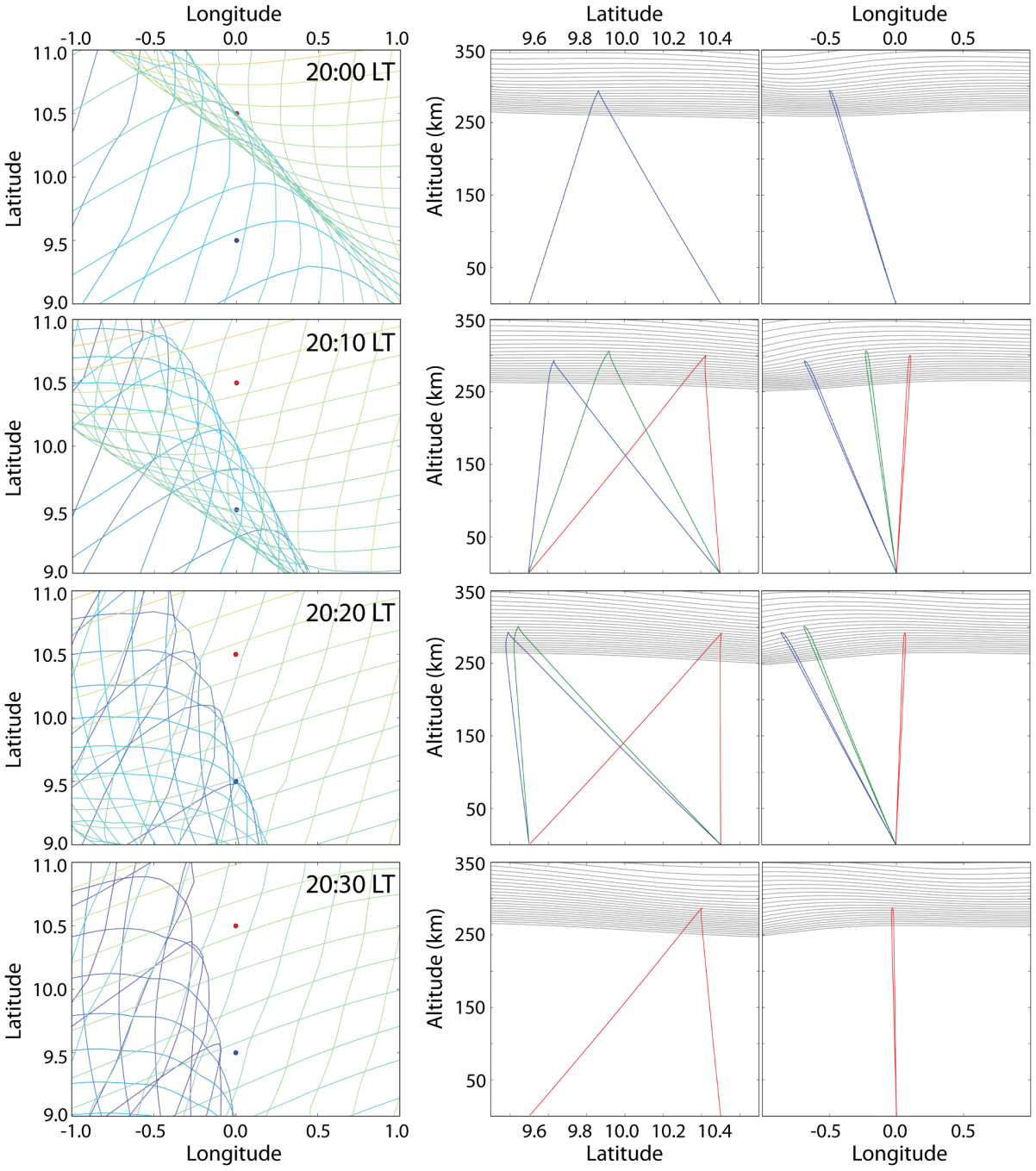


Figure 3.9: The left panels show the grid mesh technique at different times for 3.125 MHz, O-mode waves launched from a transmitter at 9.1° latitude, 0.1° longitude in the -140° bearing MSTID case. The middle and right panels show the eigenrays between the transmitter and a receiver at 10° latitude and 0° longitude at corresponding times.

Not only does this location vary in space, but it also varies in time. The second row corresponds to 20:10 LT. Now the MSTID has moved farther to the southwest (see also Figure 3.3). Now the hypothetical receiver is located in the region where multipath propagation occurs. The middle and right panels show the calculated raypaths for the three distinct eigenrays. The latitude and longitude of each eigenray reflection point varies significantly.

The third row shows the configuration at 20:20 LT. There are still three distinct eigenrays. At this time, however, two of them reflect at significantly lower latitude ($\sim$ 100 km), as well as have a greater longitudinal offset ($\sim$ 50 km) as compared to the other eigenray. From the left panel, the multipath region has nearly passed the receiver, so that it is expected that soon these two eigenrays will merge then promptly disappear.

The bottom (fourth) row shows the configuration at 20:30 LT. As expected, there is no more multipathing. The single ray remaining is quite different from the initial ray at 20:00 LT. This ray, however, is fairly similar to the single eigenvalue that exists in the case of the background simulation. This suggests that the effects of the MSTID have for the most part passed by the receiver at this time.

It is evident that these results are both fully consistent with, and explain the characteristic 'S' shape in HF dDoppler soundings during the passage of a wavelike disturbance, as originally explained in a conceptual hypothesis in earlier work [9], and also recently revisited [7]. The recent study also importantly notes the formation of the 'S' trace for a given transmitter to receiver direction depends on the orientation of the MSTID bearing with the great circle path connecting a given transmitter and

receiver [7]. For example, if the MSTID bearing is orthogonal to the great circle path connecting the transmitter and receiver, a characteristic 'S' trace of HF doppler with any significant duration is not expected to occur, though a brief instant of multipathing propagation and a step in HF Doppler should.

Typically HF radio wave ionospheric sounding techniques can only measure the observed characteristics of a received signal from which the actual ray path must be inferred given some set of physical assumptions. One such typical observable is group path delay, or virtual height. Figure 3.10 shows how the virtual height for the hypothetical scenario evolves over time. Again there is only one observed group path until the formation of the multipath triad occurs, and then after some time the triad disappears. While two of the three paths (one of which is the original) have a virtual height that increases with time, both of these eventually disappear. The new and surviving raypath has a virtual path that decreases with time.

Also of interest is how the ray changes as a function of frequency. The left panel of Figure 3.11 shows an example QVI for the background case. Here there is no multipathing, and the QVI is very smooth. The red indicates O-mode and the blue indicates the X-mode. The right panel shows an example QVI (O-mode trace only) for the -140° bearing MSTID case at the same time. The colors correspond to rays in Figure 3.9. The trace from the red eigenray is smooth and continuous. It is very similar to the O-mode trace in the background case. The traces from the other two eigenmodes differ significantly. We note that similar perturbations in the QVI have been seen in measurements [6].

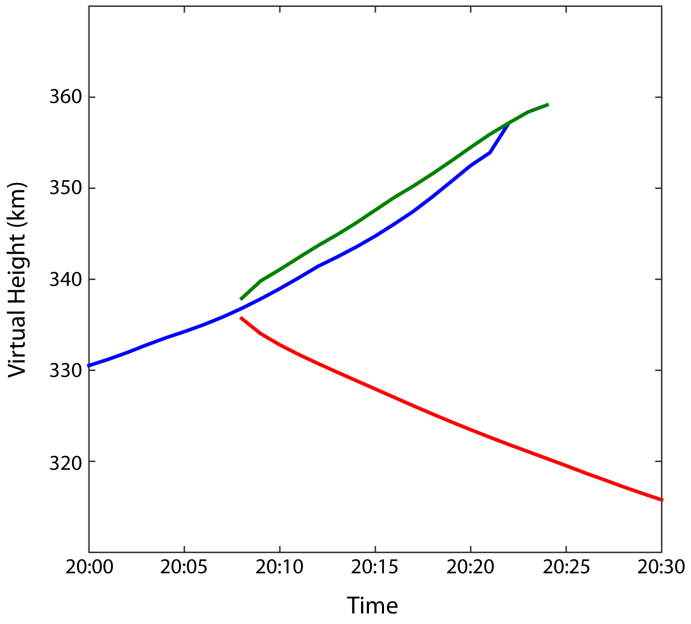


Figure 3.10: The virtual path for each of the eigenrays in the previous figure as a function of time. There is significant variation in the virtual height both between the different eigenrays and also as the MSTID propagates through the ionosphere.

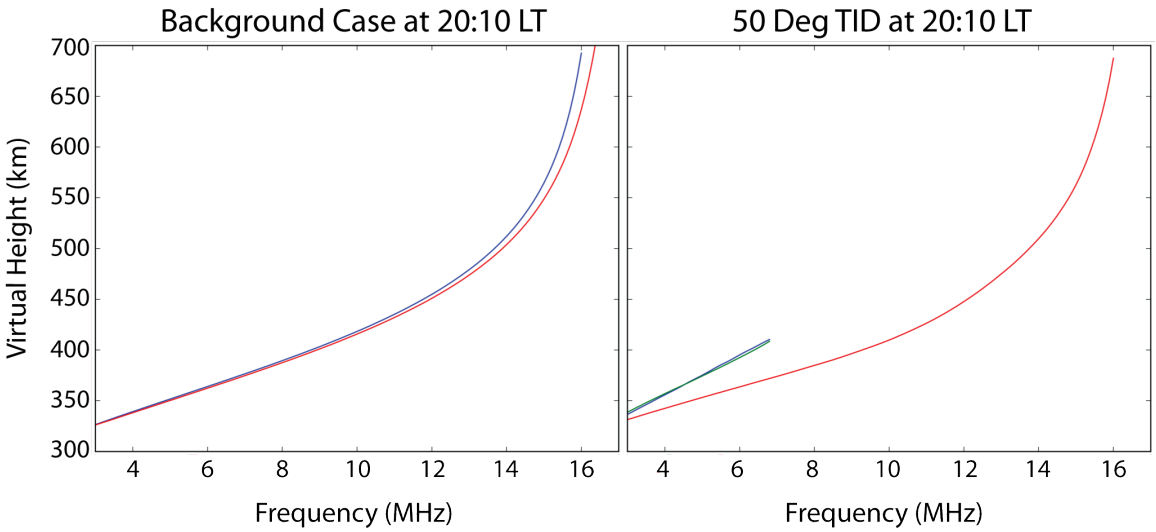


Figure 3.11: The left panel shows a QVI for the background case at 20:10 LT; in this panel, the red trace indicates the O-mode and the blue trace indicates X-mode. The right panel shows the multipathing that occurs for the O-mode trace of a QVI in the -140° bearing MSTID case. Here the colors match the colors in Figure 3.9

## 3.5 Discussion

For the first time, a realistic, full-physics, time-dependent, mesoscale ionospheric model (SAMI3) simulation of an MSTID has been used in connection with a full physics 3D HF raytrace code (MoJo-15) to predict the spatiotemporal evolution of high-angle-of-incidence HF ionospheric sounding observables. The advantage to this approach is that horizontal gradients in all directions and time evolution of the perturbation are taken into account. The main results show that these horizontal gradients have a profound effect on the path of the HF rays through the ionosphere resulting in out-of-plane propagation that cannot be properly accounted for assuming only 2D propagation. Accounting for both three dimensional propaga-

tion and three dimensional ionospheric gradients is necessary to accurately capture the complexity of radio wave propagation through the ionosphere.

The influence of the passage of an MSTID on the mapping of the set of all possible transmission paths to the ground from a given transmitter was determined through the mapping of a mesh of tilted and rotated 2D ray fans. The folding of the grid, in the presence of the horizontal gradients occurs for MSTIDs propagating at all angles. In general the rays tend to refract both in plane and out of plane along the direction of propagation. The simulations show that three eigenrays are a common feature during an ionospheric disturbance as originally hypothesized by Jones and described in [9] (see also [7]). In the future, the arrival angle and group path delay information of propagation paths should also be examined to understand the correlation between the characteristics of HF Doppler sound observables and MSTIDs.

Clearly the actual ionospheric structure can be more complicated as shown by the recent HF dDoppler traces presented by [7], where tilts are observed along up to 5 different propagation paths, each manifesting itself with a different HF Doppler trace. For the simple, yet typical MSTID propagation characteristics selected for this study the HF ray paths through the perturbed ionosphere varied widely as the MSTID propagates over the transmitter; where reflection location varied as much as 100 km during the course of the simulation. Currently, HF Doppler systems are being developed and deployed to detect MSTIDs in the ionosphere, but one of the assumptions in the algorithm is that the ray path does not vary significantly [8]. This assumption may only be valid for TIDs with long wavelengths (>300-350 km) since

the horizontal gradients would not be as steep. Future modeling work to directly simulate the HF Doppler should be undertaken, which would provide additional insights into the correlation between HF Doppler signatures and the path of the radio waves through the ionosphere. In addition, colocation of 630 nm images with HF Doppler signatures would allow for validation of the length, direction and wave periods of the MSTIDs. This is particularly important since HF Doppler observations have been used to support the hypothesis of secondary gravity waves propagating in the thermosphere [53].

# Chapter 4: Can HF Heating Generate ESF Bubbles?

Equatorial Spread F (ESF) bubbles are a critical issue for ionospheric research due to the impact on Command, Control, and Communications ($C^3$) systems, which are often disrupted and degraded in the presence of turbulent ionospheric conditions. The evolution of ESF bubbles is complex and numerical simulation models are necessary to understand their formation and evolution. One of the primary seeds used in modeling studies is to artificially create a density perturbation in the ionosphere [21]. Strong density perturbations have been observed during artificial HF heating experiments [2, 12, 39]. Thus, it has been hypothesized that density structures generated by artificial HF heating could trigger the onset of an ESF bubble as well as affect the evolution of naturally created ESF. In this chapter, a modified version of the SAMI3/ESF ionosphere code is used to model the density depletions created by HF heating, and to determine if ESF bubbles can be artificially generated.

The organization of the chapter is as follows: first we discuss the general properties and formation of ESF bubbles. This is followed by a outline of previous work in modeling the formation of ESF bubbles in the ionosphere. Next, the density structures formed by artificial HF heating are described and the previous work in modeling such structures is summarized. Then we examine the main question of how

the density structures formed by artificial HF heating impact the growth rate of ESF and whether HF heating can generate ESF. We conclude with a brief discussion.

## 4.1 The Physics of Equatorial Spread F Generation in the Ionosphere

Spread F is a broad term that characterizes spreading in the height of $F$-region backscatter returns on ionograms as shown in Figure 4.1, where the spreading in the return is indicated by the red and blue vertical lines. It is caused by irregularities and inhomogeneous structures of the normally smooth $F$-region density profile. Figure 4.2 shows an example of a Range-Time-Intensity map from the Jicamarca radar; starting around 19:30, the scatter shows spread F irregularities in the ionosphere. Such irregularities can occur at any latitude, but they are particularly pronounced at the equator, where the irregularities can grow into large scale plasma bubbles. Spread F at the equator goes by many different names, including Equatorial Plasma Bubbles (EPB) and Convective Ionospheric Storms (CIS), but for the purposes of this work, it will be referred to as Equatorial Spread F (ESF).

ESF appears in the post-sunset ionosphere, between sunset and midnight, which is when the equatorial $F$-region ionosphere can become unstable due to the generalized Rayleigh-Taylor (RT) instabilities. The nonlinear state of RT is characterized by a plasma bubble, or a vertically elongated wedge of depleted plasma along the magnetic field line. The width of the bubble in longitude is typically on the order of several hundred kilometers. Frequently multiple bubbles appear around the same time; the distance between the bubbles can vary from 10-100 km in longitude. The

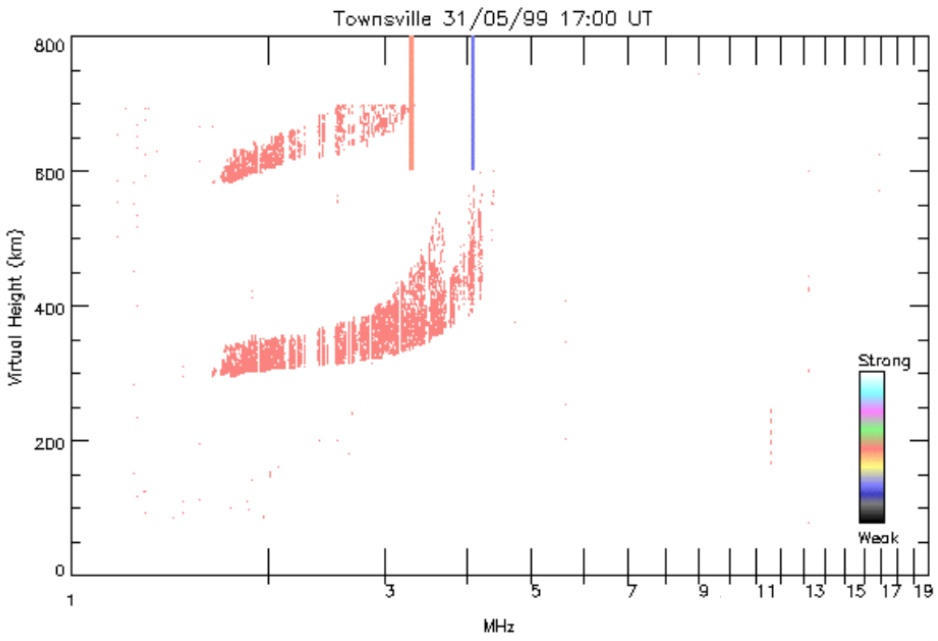


Figure 4.1: An ionogram shows spreading in the F peak, which is denoted by the vertical blue and red lines. (Reproduced from [54])

depletions have low density ($\lesssim 10^4$ cm$^{-3}$), which is an order of magnitude below the ambient plasma density. Once they form, they rise to high altitudes (above 1000 km) with upward drift speeds between 100-500 m/s. Eventually the upward drift of the bubble stops and it becomes a fossil bubble that drifts eastward with the background plasma [31].

The formation of ESF depends on both the ionosphere and the neutral atmosphere. The strength of the equatorial electrojet at sunset, the integrated Pedersen conductivity and bottomside gradients all set the initial background conditions, but the main factor that determines whether there will be ESF is the magnitude of the upward plasma drift. Meridional winds also likely play a large role in the variability of ESF since under certain conditions they can suppress or enhance the growth of a

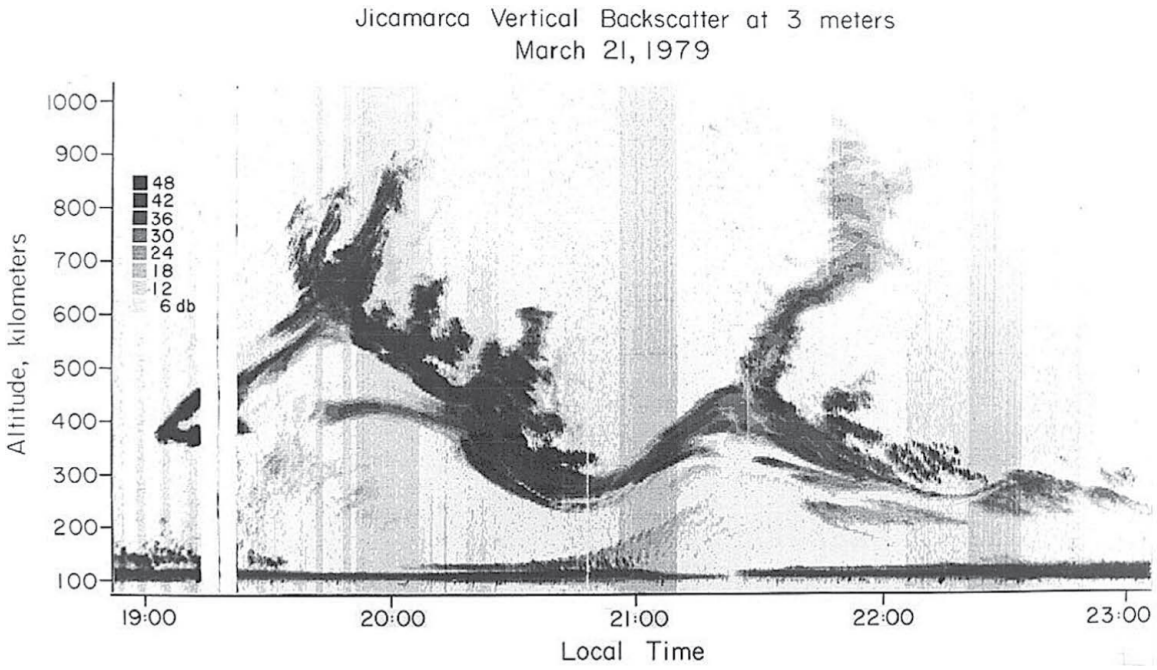


Figure 4.2: A range-time-intensity map from the Jicamarca radar shows the backscatter power at 3 meter wavelengths. From 19:00 to 19:30 LT, the $F$-peak is smooth, but rising. Around 19:30 the turbulent conditions from ESF appear and persist until 21:00. Additional irregularities are seen after 21:30. (Reproduced from [29])

bubble [25].

ESF is driven by the Rayleigh-Taylor instability, which causes small irregularities to grow due to the unstable state set up by post-sunset ionospheric conditions. In the ionosphere, the daytime E-region dynamo winds generate an eastward electric field, which causes an upward $\mathbf{E} \times \mathbf{B}$ drift in the $F$-region. This field is enhanced at dusk by a combination of the increase in zonal winds blowing across the terminator from day to night, and the sharp conductivity gradient that exists at the terminator. This enhancement of the electric field creates a stronger vertical $\mathbf{E} \times \mathbf{B}$ drift, so the $F$-region ionosphere is lifted as the sun sets. Once the sun sets, the lower ionosphere decays rapidly due to the lack of photoionization forming a steep vertical density gradient on the bottom side of the $F$-region. This is the classical setup for a Rayleigh-Taylor instability as seen in the top panel of Figure 4.3.

Once the ionosphere is in an unstable equilibrium, a seed, or small density perturbation can trigger the instability by nonlinearly increasing the growth rate. Simulations of ESF often use a 5% density perturbation on the bottomside of the ionosphere as such a seed. Other possible causes for ESF include gravity waves that are perpendicular to the magnetic field, sheer flow on the bottom side of the ionosphere and Traveling Ionospheric Disturbances (TIDs) [27]. The bottom panel of Figure 4.3 shows the ionosphere with a density depletion. Charges build up around the density perturbation due to the divergence in current between the dense $F$-region and the depletion. The charge separation results in a polarization electric field in the cavity and the plasma in the cavity $\mathbf{E} \times \mathbf{B}$ drifts upward creating a larger density depletion. This cycle is unstable, and results in nonlinear growth of

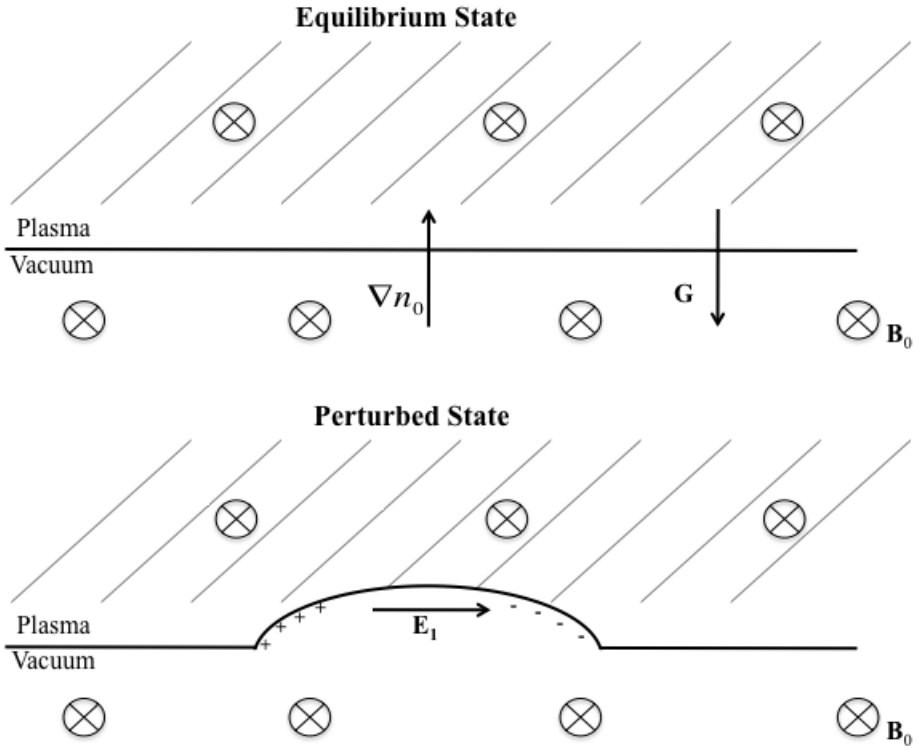


Figure 4.3: The top panel shows the background conditions responsible for the Rayleigh-Taylor instability: a dense fluid is situated above a light fluid in an unstable equilibrium. The introduction of a small density perturbation, such as in the bottom panel, causes charge to build up at the edges of the depletion, which generates a polarization electric field, $\mathbf{E}_1$. The plasma in this region drifts upward from the resultant $\mathbf{E}_1 \times \mathbf{B}$ drift creating a larger density perturbation. This cycle continues and generates irregularities that bubble up though the dense fluid layer.

the density depletion, which propagates upward through the dense $F$-region.

Note that in the ionosphere, the local density at the equator is not as important for ESF formation as the integrated electron density along the magnetic field line. Due to the processes described above, a steep density gradient forms in the field line integrated electron density. A subsequent perturbation to the field line integrated electron density triggers the formation of ESF.

Significant progress has been made by other authors in modeling ESF in the ionosphere. In particular, a number of studies have been done with SAMI3/ESF, which is the model used in this work. The first studies demonstrated that the model could produce realistic ESF studies using a simple density perturbation in the bottomside of the $F$-region [21]. Figure 4.4 shows the evolution of an ESF bubble in SAMI3/ESF. The left panels show the electron density as a function of longitude and altitude for different times during the simulation. The right panels show the electron density at the same times, but as a function of latitude and altitude. As time progresses, the ESF bubble rises through the $F$-peak to high altitudes. The right panels show that the depletion extends along the field line.

SAMI3/ESF was subsequently used to investigate a number of different aspects of ESF. For example, the atomic and molecular ion dynamics during an ESF event were investigated and it was discovered that during the early stages a super fountain effect can occur with upward ion velocities of 1km/s. In addition, it was found that plasma depletions can be enhanced by draining $H^+$ ions along the geomagnetic field and lifting molecular ions such as $NO^+$ to altitudes as high as 400 km [22].

Another study focused on the temperature evolution of the plasma during

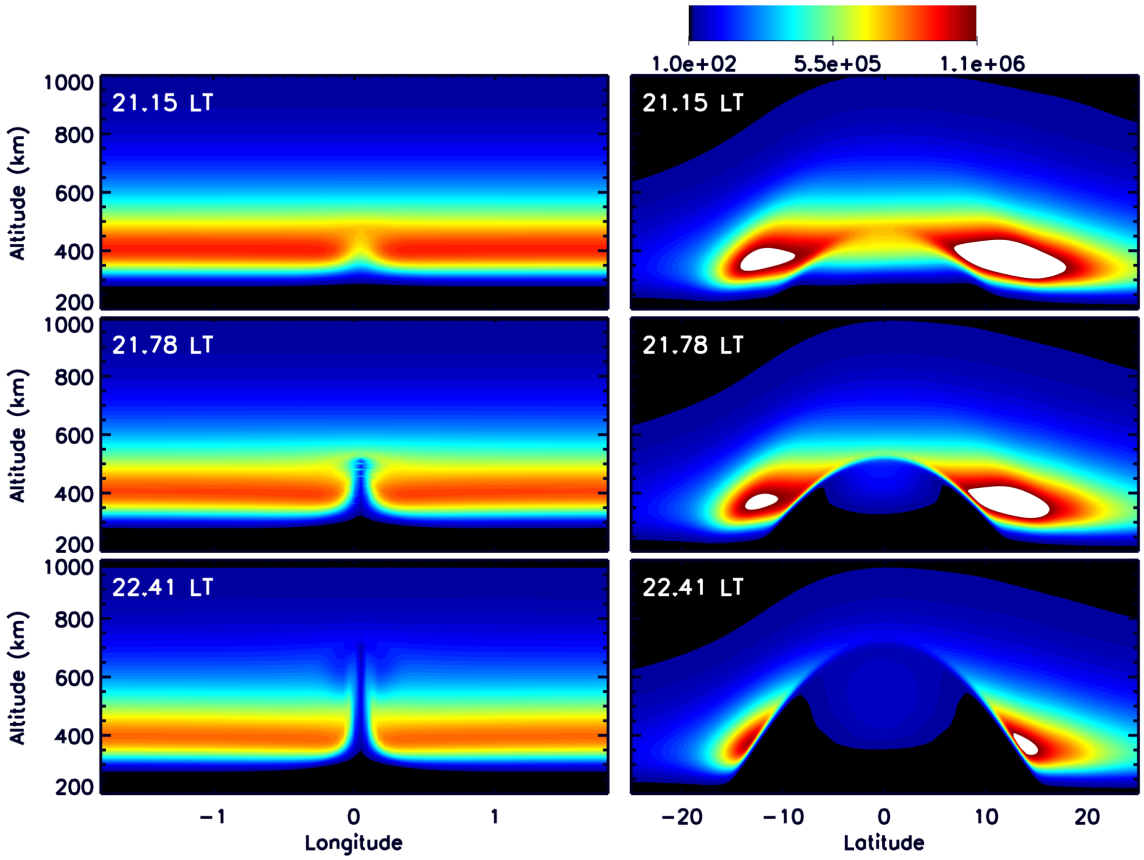


Figure 4.4: Contour plots of electron density ($cm^{-3}$) as a function of longitude and altitude (left panels) and as a function of latitude and altitude (right panels) at different times during a SAMI3/ESF simulation. In the top panels, there is a small perturbation on the bottomside of the ionosphere at the equator. As time progresses the ESF bubble propagates upward through the $F$-peak. Note that the depletion extends along the magnetic field line (right panels). The color white indicates saturation.

ESF [23]. Ions and electrons were found to undergo adiabatic cooling due to the increase in flux tube volume as the plasma bubble rises. Ion heating also occurs as the ions stream down the converging magnetic field due to compression. In addition, electrons at high altitudes ($\sim$ 1200 km) can be heated by thermal conduction and hydrogen ions at low altitudes can be heated by ion-neutral frictional heating.

A series of studies [24, 25, 32] have focused on the effects of the neutral winds on ESF. Zonal winds were found to have a strong influence on the morphology of the ESF bubbles. In some cases the plasma bubble will tilt westward. Observations of a reversed 'C' shaped bubble have been reproduced in the model. The meridional wind has been found to have a stabilizing or destabilizing effect on ESF depending on the direction of the winds.

The studies described above use a small ($\sim$ 5%) Gaussian-like density perturbation along the flux tube situated below the peak of the integrated field line density as a trigger. The perturbation is centered at 0° longitude and is generally at about 400 km altitude. A series of studies examined other potential triggers for ESF in the ionosphere. First it was shown that a Medium Scale Traveling Ionospheric Disturbance (MSTID) was able to trigger ESF, and that the coupling between the two was strongest when the wave vector is perpendicular to the geomagnetic field [33]. Other studies demonstrated that both circular (local) and plane wave (nonlocal) gravity waves couple to the bottom side $F$-region and can effectively seed ESF [34,35]. These observations motivated our study of HF heating triggering or controlling ESF.

## 4.2 Modeling the Effects of Artificial HF Heating in the $F$-Region Ionosphere

Powerful HF heaters at HAARP and other facilities can create strong electron heating by injecting HF waves into the ionosphere. The heated electrons cause the plasma to expand away from the heated region, leaving behind a density depletion. Initially the ions are not strongly affected by the HF heating since they are heavy and can efficiently transfer momentum via ion-neutral collisions. The electrons are not as strongly coupled to the neutral particles, and they are light, so their temperature increases significantly and they respond by expanding away from the heated area. This expansion of the electrons creates charge separation, which sets up an ambipolar electric field. The ambipolar electric field effectively glues the electrons and ions together so that they move as one, and thus the plasma as a whole expands out of the heated region.

Since the particles are effectively tied to the magnetic field, the expansion takes place parallel to $B_0$, and plasma travels both up and down the field line, which is referred to as field-aligned plasma transport. An example of this is shown in Figure 4.5, which shows the electron density as a function of longitude and altitude in the left-hand panel, and as a function of latitude and altitude in the right-hand panel. In this simulation, a heater at Arecibo's magnetic latitude (28°) was on for 15 minutes. The heater frequency was 5.1 MHz, which matched the plasma frequency at 300 km altitude and the model heating rate was set to 1000 K/s .

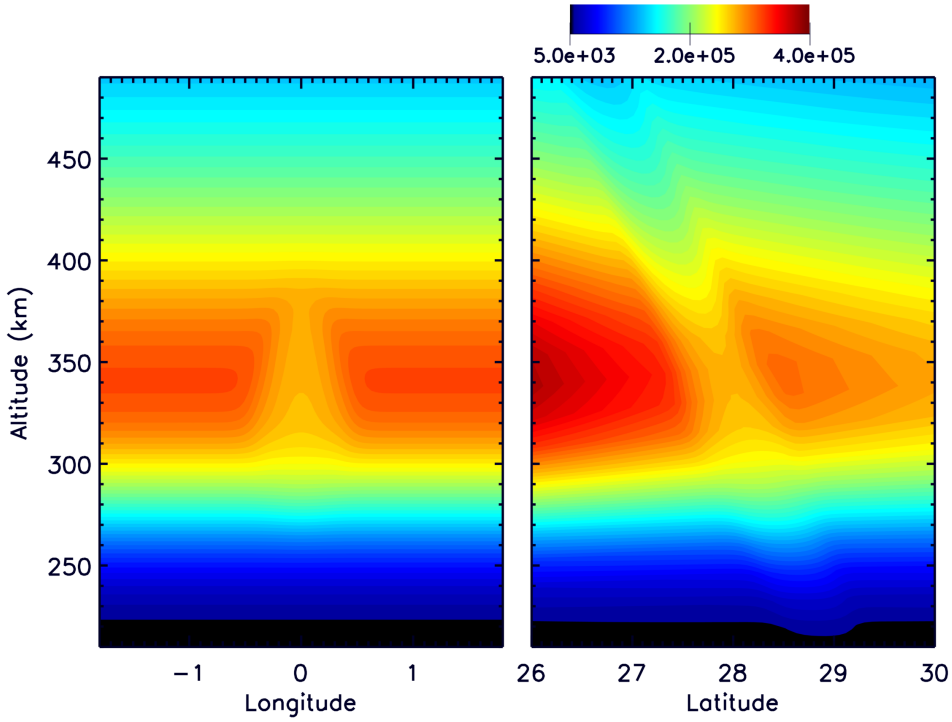


Figure 4.5: Contour plots of electron density ($cm^{-3}$) as a function of longitude and altitude (left panel) and as a function of latitude and altitude (right panel) show a density depletion created from 15 minutes of constant artificial HF heating at Arecibo Observatory.

In some cases, the density perturbation propagates along the entire magnetic field line such that an artificial duct is formed. The majority of previous modeling work has focused on the investigation of the processes that lead to field-aligned duct formation. Some of these inquiries occurred during the time that the Arecibo heater was active, but they were restricted to 1D models and limited to altitudes below 500 km [42]. More recently, there have been a series of studies using modified versions of SAMI2, which is ideal for such investigations since it includes the ion inertia parallel to B in the ion momentum equation. This is critical to modeling artificial ducts since it allows for the study of sound wave propagation in the plasma. Also, SAMI2 models the plasma along the entire field line so conjugate effects can be investigated.

In the first study using a modified version of SAMI2, a localized, Gaussian-shaped heating source was added to an early version of SAMI2 to demonstrate that ducts could form in the ionosphere from strong thermal perturbations [44]. It was demonstrated that HF heating generates a thermal wave in the plasma, which propagates through the topside ionosphere and down the other side of the magnetic field line. The wave drove ion outflows and displaced the ambient plasma leading to the formation of a density duct that stretched along the magnetic field line to the conjugate point. The study focused on the HF heating response of plasma confined to a single magnetic field line, so it was essentially 1D. In addition, a number of comparisons were made to determine the effect of the basic heating parameters on the creation of artificial ducts.

A second study also used a localized, Gaussian-shaped heating source, but it

used a more robust version of SAMI2 as the basis for the heating model [40]. The purpose of the study was to validate the new heating model against two experiments: the first experiment was done at the SURA heating facility and used DEMETER as a diagnostic tool; the second was an EISCAT heating experiment using the EISCAT Incoherent Scatter Radar (ISR) as a diagnostic tool. The new heating model was shown to reproduce the experimental observations.

Another study examined the impact of HF heating at Arecibo on the conjugate ionosphere [55]. In particular, the development and formation of enhanced electron temperature along the heated field line and the associated changes in electron density was examined. It was found that the conjugate effects occurred during periods of relatively low electron densities, such as during the night, or during periods of low $F_{10.7}$. The effects on the conjugate ionosphere were restricted to the topside $F$-layer and did not penetrate below the $F$-peak on the conjugate side. The primary inhibitor of conjugate effects was heating losses associated with inelastic electron-neutral (particularly $N_2$) collisions.

Finally, one other similar study used a three-dimensional model of HF heating to determine the effects of the neutral winds on artificial duct formation [57]. A moderate zonal neutral wind of 60 m/s was found to significantly suppress duct formation, such that the density depletion at the conjugate point is almost imperceptible.

Here we use a version of the SAMI3/ESF that has been modified similarly to the previous work to simulate artificial HF heating. As described in Section 2.1.4,

the original electron temperature equation in SAMI3/ESF is:

$$\frac{\partial T_e}{\partial t} - \frac{2}{3}\frac{1}{n_e k} b_s^2 \frac{\partial}{\partial s}\kappa_e \frac{\partial T_e}{\partial s} = Q_{en} + Q_{ei} + Q_{phe} \tag{4.1}$$

The terms on the right-hand side of the equation are heating/cooling terms associated with electron-neutral collisions ($Q_{en}$), electron-ion collisions ($Q_{ei}$), and photoelectron heating ($Q_{phe}$). The second term on the left-hand side is a diffusion term, $\kappa_e$ is the parallel electron thermal conductance, k is the Boltzmann constant, and $b_s$ is the component of the magnetic field in the field line direction.

In order to simulate HF heating, a Gaussian-shaped source term is added to the electron temperature equation. This is also known as the 'hot brick' model:

$$Q_{RF} = \left(\frac{dT_e}{dt}\right)_0 \exp[-(z-z_0)^2/\Delta z^2] \exp[-(\theta-\theta_0)^2/\Delta\theta^2] \exp[-(\phi-\phi_0)^2/\Delta\phi^2] \tag{4.2}$$

In Eq. (4.2), $(dT_e/dt)_0$ is the total heating rate per electron in K/s. The other parameters are the electron number density, $n_e$; Boltzmann constant, $k$; the center altitude of the heating location, $z_0$; the vertical extent of the heated region, $\Delta z$; the latitude of the heating location, $\theta_0$; the latitudinal extent of the heated region, $\Delta\theta$; the longitude of the heating location, $\phi_0$; and the longitudinal extent of the heated region, $\Delta\phi$. A previous study compared data from DEMETER observations of a SURA experiment to simulations using the 2D version of this model and concluded that a model heating rate of 1000 K/s (approximately $2.6 \times 10^9$eV cm$^{-2}$s$^{-1}$) was in best agreement with the data, so we will use that value here [40].

We assume that the altitude range from 375 km to 400 km is where the HF heating occurs, which corresponds to a heater frequency of about 9 MHz. The latitudinal extent of the heated region is set to $\Delta\theta = 0.25°$. The particular longitude

is irrelevant since the magnetic field is not tilted, so we define a grid which covers -2° to 2° in longitude, and we set $\phi_0$ to 0° longitude. The longitudinal extent is set to $\Delta\phi = 0.25°$.

SAMI3/ESF uses output from the SAMI2 model for its initial state. We ran SAMI2 for 48 hours using the following geophysical conditions: $F_{10.7} = 100$, $F_{10.7}A = 100$ ($F_{10.7}A$ is the 81-day centered average of $F_{10.7}$), Ap = 4, and day of year = 130. The simulation includes geographic longitudes from ±2°. The plasma parameters at 19:30 UT of the second day are used to initialize the 3D model.

## 4.3 Can HF Heating Generate ESF Bubbles?

To study whether HF heating can generate ESF bubbles we ran three different simulations using the modified SAMI3/ESF code. The first simulation was a control simulation which did not include any perturbations to the plasma density. The second simulation imposed a small Gaussian-like density perturbation at $t = 0$ along the flux tube with apex at 400 km and centered at 0° longitude. The third simulation used a density perturbation that was created from 15 minutes of HF heating (from 19:30-19:45) just below the density peak at the equator, between 375 and 400 km. In each case, the neutral wind values (both meridional and zonal) were set to 0 m/s and the code was run from 19:30 to 1:00 LT.

Figure 4.6 shows contour plots of the logarithmic electron density for the run with the density perturbation and the run with the HF heating perturbation at 19:45 and 22:00. In the left column, the density perturbation case, there is an initial

density perturbation at 19:45, which results in a rising ESF bubble by 22:00. The right column shows that in the case of the HF heating, a similar density perturbation is produced around 19:45, but this density perturbation does not result in an ESF bubble. We note that the control simulation also did not generate an ESF bubble.

In order to understand why there is no ESF bubble created in the HF heating case, we present Figure 4.7, which shows the electron density along the field line for each of the three simulations. The black line is the control case with no density perturbation. In the density perturbation case (blue line), the electron density decreases uniformly along the field line between about $\pm 5^\circ$ latitude. In the case of the HF heating, however, there is a decrease in density at $0^\circ$ latitude but an increase at $\pm 2^\circ$ latitude. The difference in the density modification along the field line is due to the nature of the HF heating. When the ionosphere is heated, the temperature increases, which causes a pressure gradient. This pressure gradient drives electrons down the field line to higher latitudes, away from the heating location; it does not decrease the number of electrons along the field line.

The change in the electron density causes a corresponding change in the Pedersen conductivity along the field line. The field line integrated Pedersen conductivity is a key factor in the growth rate of an ESF bubble [56]. The growth rate is defined as follows:

$$\gamma = -\frac{\int \sigma_{H_c}(g_p/L_n)ds}{\int \sigma_p ds} \tag{4.3}$$

where $g_p$ is the gravitation term, $s$ is in the direction of the field line, $L_n^{-1} = \partial ln(n_0)/\partial p$, $n_0$ is the electron density and $p$ is perpendicular to the field line. The

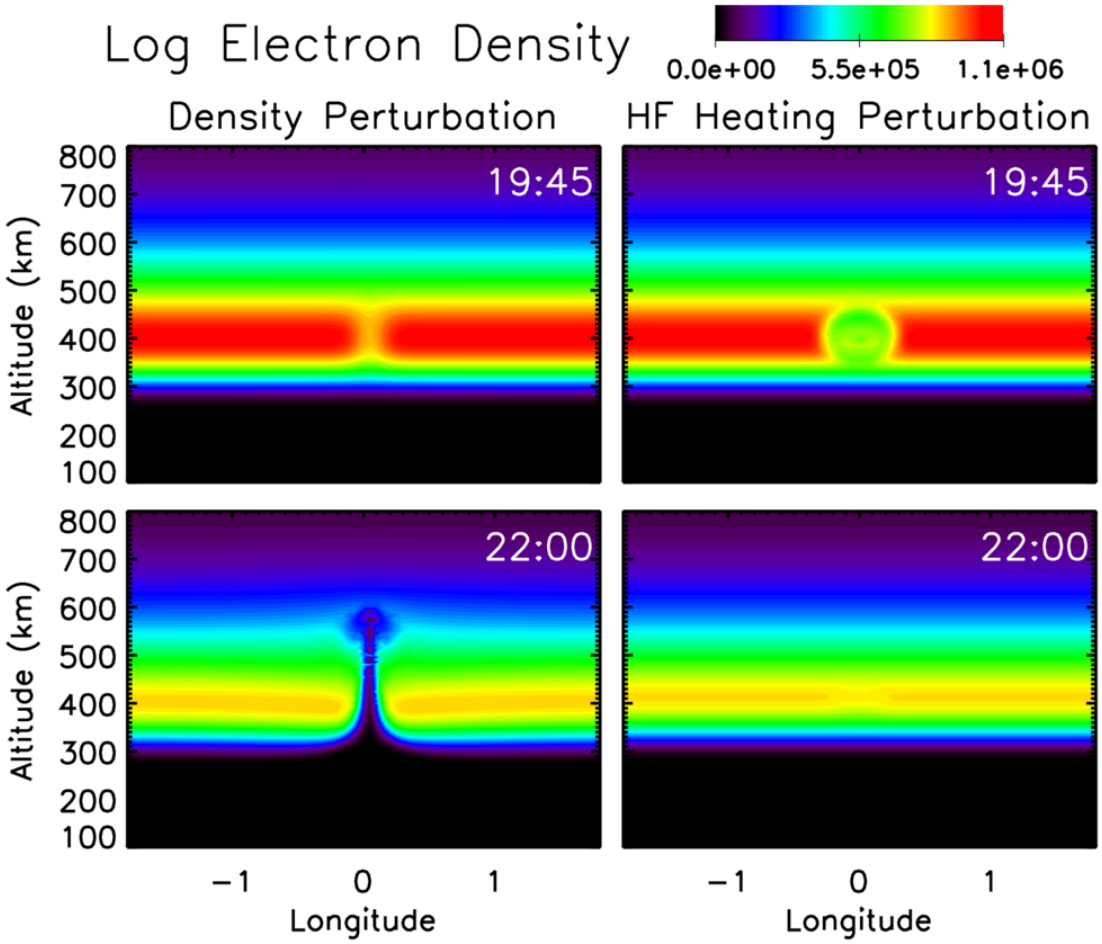


Figure 4.6: Contour plots of logarithmic electron density ($cm^{-3}$) as a function of longitude and altitude. The left column shows electron density at two different times in a simulation with a standard density perturbation, which triggers the formation of an ESF bubble. The right column shows the electron density during a similar simulation that uses HF heating as the density perturbation seed. In this case no ESF bubble is formed.

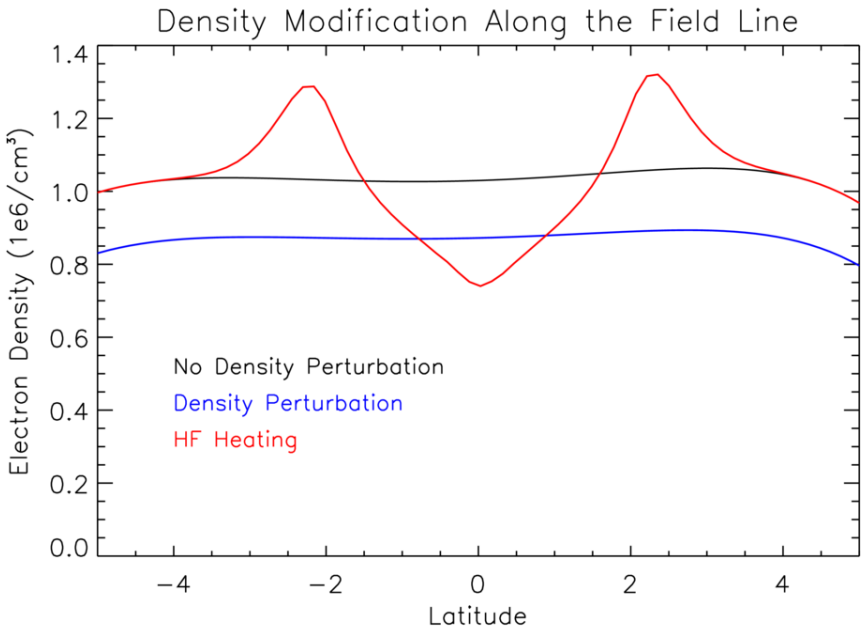


Figure 4.7: Line plot of electron density along the field line as a function of latitude. The black line is the control case with no density perturbation. The addition of a standard density perturbation reduces the density along the field line (blue line). HF heating (red line) reduces the density at 0° latitude, but increases it around ±2° latitude.

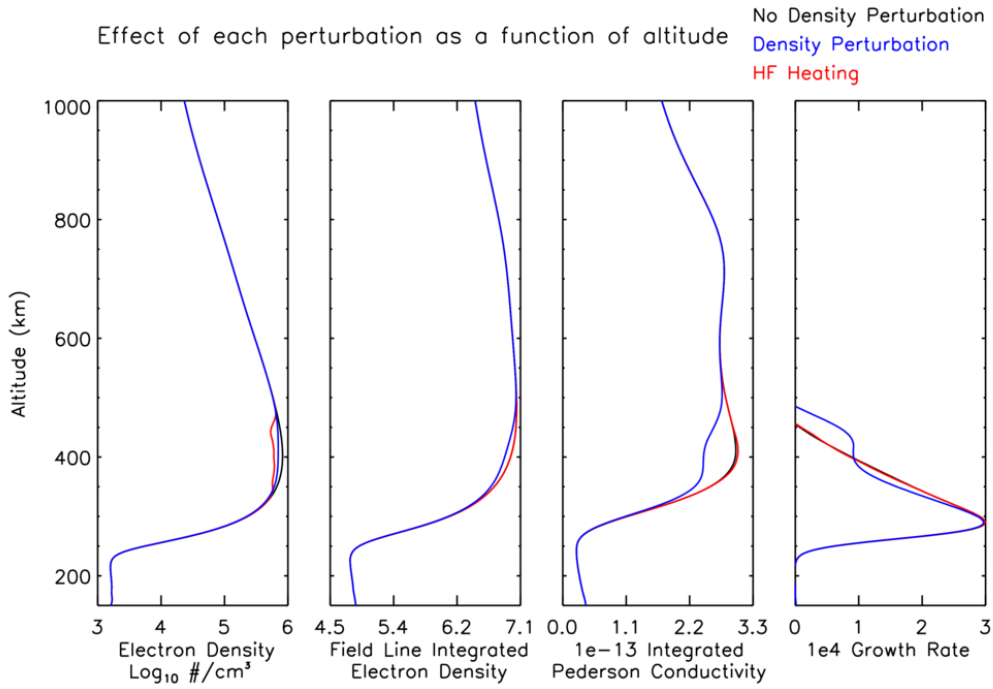


Figure 4.8: Line plots of ionospheric quantities as a function of altitude for each of the three simulations at 19:45 LT. The left panel shows the logarithmic electron density at 0° latitude, the second panel from the left shows the field line integrated electron density in the same location, the third panel from the left shows the integrated field line Pedersen conductivity. The panel furthest to the right shows the growth rate associated with an ESF bubble. Only the density perturbation case shows a change in the ESF growth rate.

Pedersen conductivity can be approximated as $\sigma_P \approx \sum_i \frac{nec}{B}\frac{\nu_{in}}{\omega_i cf}$, where $\nu_{in}$ is the ion-neutral collision frequency and $\omega_{icf} = \mathrm{e}|B|/m_i\mathrm{c}$. The Hall conductivity can be approximated as $\sigma_{H_c} \approx \sum_i \frac{nec}{B}\frac{1}{\omega_i cf}$. The growth rate defined in Eq. (4.3) is inversely proportional to the field line integrated Pedersen conductivity.

Figure 4.8 shows different plasma quantities as a function of altitude. The left panel illustrates the difference in electron density in each of the three simulations. Both the density perturbation and HF heating simulations show a decrease

in electron density near the $F2$ peak. The next panel shows the integrated field line density for each simulation. Since in the HF heating case, the electron density is not uniformly decreased, but is redistributed along the field line, the integrated electron density is basically unchanged, whereas the density perturbation case shows a decrease in the field line integrated density. The third panel from the left shows the corresponding integrated Pedersen conductivity. In the case of the density perturbation, the integrated Pedersen conductivity shows a decrease around 400 km, but there is no reduction in the HF heating case. The result of this difference is shown in the far right panel, which shows the growth rate for each case. The HF heating case does not show a change in the growth rate, which is expected because there was no change in the integrated field line electron density or Pedersen conductivity. Since the growth rate is unchanged, no ESF bubble forms. In the density perturbation case, on the other hand, there is a marked increase in the growth rate around 400 km altitude due to the changes in the field line integrated quantities.

## 4.4 Discussion

This study indicates that the density perturbations created by artificial HF heating in the ionosphere will not generate ESF bubbles at low latitudes. The results of the simulation show that the density holes created by HF heating are surrounded by local increases in the electron density. Thus, instead of a true hole in the ionosphere, the plasma has simply been redistributed along the magnetic field line. Since the plasma has not been uniformly depleted along the field line, the

integrated field line Pedersen conductivity does not decrease. Without the change in Pedersen conductivity, the growth rate remains unchanged and an ESF bubble does not form.

A number of other simulations were also run with variations on the HF heating parameters. Parameters modified during the continuing study include the beam width, the timing and/or duration of the HF heating, as well as the effect of modulated heating. None of these variations were found to have any significant effect on the results described here. The effect of the heater power was also examined using the effective heating rates for actual HF heaters. The original study approximated the power at SURA (and presumably also the new heater at Arecibo). We used values of 3000 K/s to approximate the power of the EISCAT heater and 5000 K/s for HAARP based on model comparison studies [38, 40], however, changing the heater power did not modify the results and no ESF bubble was created. We have also done simulations where the HF heating was applied at other locations along the magnetic field line and no ESF bubbles were generated.

Several simulations were also performed to evaluate the effect of the neutral winds on these results. Zonal winds were found to transport the system in the longitudinal direction, but did not lead to ESF bubble generation. Meridional winds have been found to be stabilizing or destabilizing depending on their latitudinal gradient [25]. However, we were interested to see if the winds would transport electrons to low enough altitudes to affect the chemical loss rate. We found that a relatively large, constant meridional wind of 60 m/s was not effective enough to transport the electrons to low enough altitudes and the addition of meridional winds

did not allow for the creation of an ESF bubble.

A previous study modeled HF heating at the location of the EISCAT heater (near Tromsø, Norway at a latitude $\sim 70°$) and showed that a significant number of electrons were transported to low enough altitudes ($\sim$ 250 km) for recombination to occur [40]. We do not see this in our simulation studies. The reason is that the magnetic field declination angle at Tromsø is $\sim 78°$ (almost vertical) and the heated plasma at $\sim$ 350 km only needs to propagate through $\sim$ 200 km of the thermosphere. However, in the equatorial region the magnetic field declination angle is $\sim 0°$ and the heated plasma needs to propagate $\sim$ 1000 km through the thermosphere to reach an altitude $\sim$ 250 km. In the bottomside ionosphere, there are a greater number of neutral particles, so much of the HF heating is lost to electron-neutral collisions [55]. This physical loss mechanism suppresses HF heating and prevents electrons from being transported to lower altitudes.

The role of suprathermal electrons generated by HF heating experiments is not included in SAMI3. For sufficiently high electron energies, these electrons can increase the electron density at lower altitudes by impact ionization [45]. However, this effect would increase the Pedersen conductance along a flux-tube which inhibits the growth of the Rayleigh-Taylor instability [32, 37]. On the other hand, suprathermal electrons can also excite the $N_2$ vibrational state which could lead to an enhanced recombination rate of electrons and decrease the electron density. This would decrease the Pedersen conductance and could potentially be sufficient to allow ESF bubbles to develop. To mimic the effect of enhanced recombination at lower altitudes we 'turned off' electron-neutral cooling that inhibits heat flow to the

lower ionosphere. We do find that plasma travels to lower altitudes and begins to recombine. However, even for this situation, we found that no ESF bubbles formed.

We also briefly considered the question of whether HF heating could suppress an ESF bubble already forming in the ionosphere. Our preliminary results suggest that this may not be possible because the increase in the field line integrated Pedersen conductivity is small relative to the decrease from the initial ESF density perturbation bubble seed. Future work will attempt to address this problem more comprehensively.

# Chapter 5: The Role of Neutral Winds on $F$-Region Ionospheric HF Heating: The Snapback Effect

As discussed in Section 2.3, the development of high power HF ionospheric heaters, such as HAARP and EISCAT, has been an extremely valuable tool to study, in a cause and effect fashion, physical processes occurring in the ionosphere. Of particular interest is $F$-region, HF heating resulting in the generation of electron density structures, including ionospheric ducts [57]. It has been found that the time-length of heating is an important factor of the triggered phenomena. At high latitudes, given the slow variability of ambient $F$-region conditions, the effective heating time is essentially controlled by the heater on-off time. Previous experiments have demonstrated that this is not true at middle and equatorial latitudes, where the ionospheric dynamics resulting from neutral winds constantly changes the heating location, preventing the steady state heater operations that are generally desired [2]. Understanding the heating time constraints imposed by the presence of neutral winds is important in the design of high power novel transmitters that are being developed under an AFOSR MURI [43].

In this chapter we exploit a raytrace model (MoJo) and a 3D ionospheric model to examine the interaction effects between the ionospheric drifts caused by

neutral winds and artificial HF heating. First, the effect of a zonal neutral wind on the $F$-region ionosphere is explained, followed by a demonstration of the effect of the zonal wind on an electron density cavity generated by artificial HF heating. Next the conclusions of an Arecibo HF heating experiment are examined. Due to the interaction effects between the heater wave and the density cavity, the need for a self-consistent HF heating model is established and a new model based on these parameters is outlined. The following section shows simulation results from the new model, which is used to simulate the snapback experiment and to explain the physical mechanism behind the snapback effect. Lastly, we present conclusions and discuss the implications of this work on the development of future HF heaters for use in the low and middle latitudes.

## 5.1 The Modification of Ionospheric Density Structures by Zonal Neutral Winds

As described in Section 2.3, artificial HF heating generates electron density structures such as ionospheric ducts and cavities. The morphology of these depletions may be altered due to the interaction of the ionosphere and the thermosphere; in particular, zonal neutral winds affect the dynamics of the ionosphere, which influences of the evolution of artificially generated HF heating structures.

The thermospheric winds are driven primarily by pressure gradients due to solar-driven temperature differences. The neutral winds in the $F$-region directly affect the plasma dynamics in the ionosphere, especially at night. The meridional

wind (north-south) primarily drives plasma up and down in the direction of the field lines. The zonal wind, on the other hand, can create strong zonal $\mathbf{E} \times \mathbf{B}$ drifts through an interaction that is sometimes called the $F$-region Dynamo. This is the dominant dynamo process at night since the $E$-region decays rapidly after sunset [13].

As outlined in Section 2.1.3, the electrons are restricted to motion along the geomagnetic field because the ratio of electron-neutral collisions to the electron cyclotron frequency is much less than 1 ($\nu_{en}/\omega_{ecf} << 1$). The ions are not tied as tightly to the geomagnetic field because the ratio is comparably larger ($\nu_{in}/\omega_{icf} \sim 1/300$). Thus, while the electrons do not move in direct response to the neutral winds, the ions do. The ratio also determines the direction of motion of the ions to an applied force; the direction is given as: $\tan^{-1}(\omega_{icf}/\nu_{in})$, which in this case is nearly 90° at 300 km altitude.

The basic outline for the $F$-region dynamo is shown in Figure 5.1, which assumes that there is a constant zonal neutral wind in the eastward direction. The zonal wind drives the ions upward in the $\mathbf{U} \times \mathbf{B}$ direction. Since the current can be considered to be divergence-less for time scales longer than a second ($\nabla \cdot \mathbf{J} = 0$), a polarization electric field of equal magnitude must be generated in the opposite (downward) direction. The resulting $\mathbf{E} \times \mathbf{B}$ drift is approximately the same magnitude as the zonal neutral wind and is in the same direction (eastward). Thus, a zonal wind in the eastward direction causes the plasma to drift eastward at approximately the same speed as the zonal wind.

The $\mathbf{E} \times \mathbf{B}$ drift also influences the evolution of density cavities generated

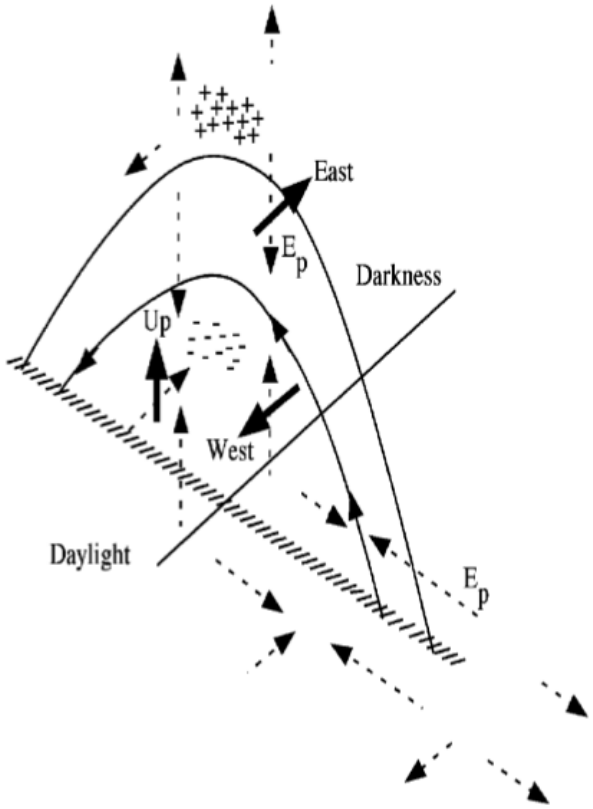


Figure 5.1: Illustration of the $F$-region dynamo effect: an eastward zonal neutral wind creates a $\mathbf{U} \times \mathbf{B}$ drift which drives the ions upward; this results in a downward polarization electric field ($E_p$). The electric field establishes an eastward $\mathbf{E}_p \times \mathbf{B}$ drift of the plasma at $F$-region altitudes. (Reproduced from [18])

from artificial HF heating. In order to determine the effect of zonal winds on the density depletions, two simulations of artificial HF heating were run using the model described in Section 4.2. The simulation parameters are consistent with a hypothetical heater at Arecibo Observatory in Puerto Rico. Note that in this model, the heating location does not change as a function of time; thus for the full hour that HF heating is turned on the Gaussian temperature perturbation is applied to a fixed location of 330 km altitude, 0° longitude, and 28° magnetic latitude. In each simulation, a different value of the zonal neutral wind is assumed; in the first there is no zonal wind and in the second, a constant, 60 m/s zonal wind is used.

Figure 5.2 shows contour plots of the electron density at the heated location for each simulation as a function of longitude and altitude after one hour of HF heating. For a 0 m/s zonal wind (left panel), the density perturbation is symmetric in longitude and altitude. The addition of a 60 m/s zonal wind (right panel), however, leads to an electron density distribution that is highly antisymmetric in longitude.

The addition of a constant zonal wind also alters the evolution of the density cavity in time. Figure 5.3 shows the time progression of the relative electron density ($n_e^h/n_e^a$) as a function of longitude at the heating latitude and altitude for the case with a 60 m/s zonal wind. Here $n_e^h$ is the electron density in a run with artificial HF heating, and $n_e^a$ is the electron density in the ambient case. Shortly after heating begins, the density hole is nearly symmetric at about 0° longitude. As time progresses, however, the density hole becomes deeper and shifts eastward in longitude. This is because at negative longitudes the electrons are driven down the field line to

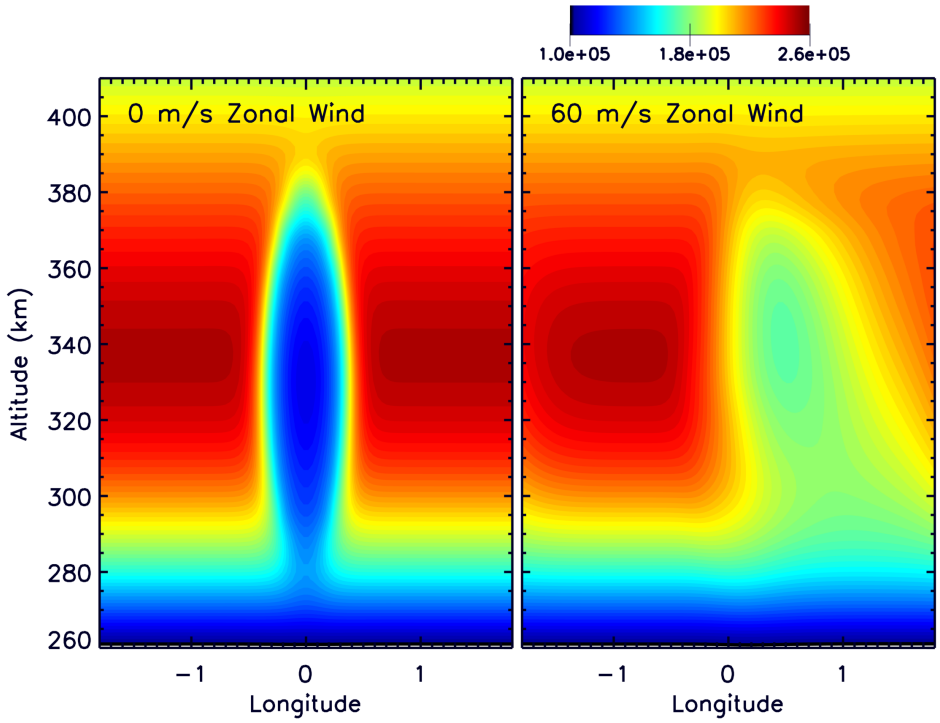


Figure 5.2: Contour plots of electron density ($cm^{-3}$) as a function of longitude and altitude illustrate the effect of zonal winds on an electron density cavity generated by artificial HF heating. When the zonal wind is absent (left), the density depletion is symmetric in longitude; however for a constant, 60 m/s zonal wind (right), the density gradients are antisymmetric in longitude.

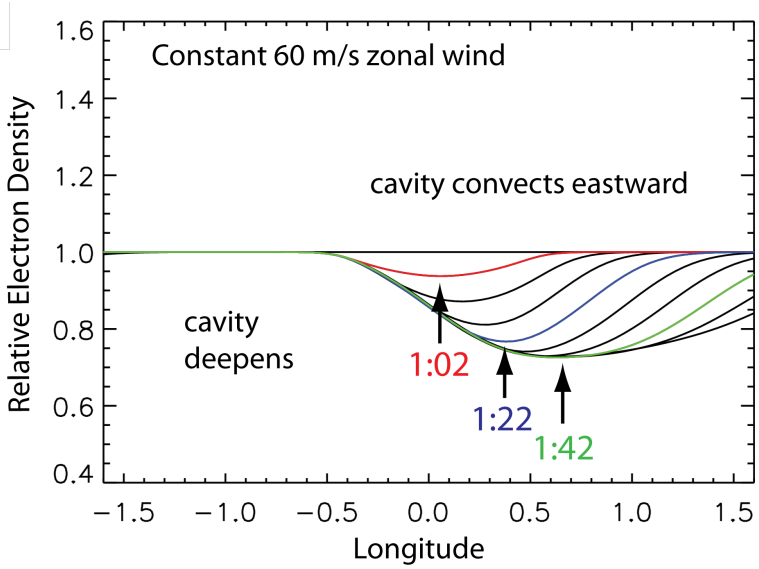


Figure 5.3: The relative electron density (heated/ambient) as a function of longitude at different times during artificial HF heating in the presence of a constant 60 m/s zonal wind shows that the density gradient becomes increasingly antisymmetric about 0° as heating continues.

the conjugate side by the HF heating and they also drift eastward due to the zonal $\mathbf{E} \times \mathbf{B}$ drift. They are also replenished, however from electrons drifting eastward from more negative longitudes. At positive longitudes, the electrons are depleted due to heating and the zonal $\mathbf{E} \times \mathbf{B}$ drift, but the density is not replenished as quickly since the electrons at more negative longitudes have already been depleted.

Thus, a zonal neutral wind of 60 m/s causes the electron density depletion to evolve as a function of time such that large longitudinal electron density gradients appear in the ionosphere near the heater beam reflection location. Large horizontal gradients have a significant effect on the path of HF radio waves through the ionosphere, as described in Chapter 3. This suggests that the location of HF heating

will evolve as the shape of the density cavity changes.

## 5.2 The Necessity for a Self-Consistent HF Heating Model

A number of campaigns have been conducted over the past 30 years where density structures formed from HF heating have been observed and analyzed [2, 12, 39]. One early experiment at Arecibo demonstrated that there may be interactions that occur between the density cavity and the heater wave, such that the location of HF heating changes as a function of time [2]. The experimental results were that the heating location drifted eastward or westward in longitude depending on the direction of the zonal neutral wind, and eventually "snapped back" to the original heating longitude. The motion velocity was independently validated using the Arecibo incoherent scatter radar for plasma drift measurements [3].

This process is illustrated in Figure 5.4. It was hypothesized that the horizontal density gradients at the reflection point would cause the ray to be refracted in the same direction as the winds, and thus the location of HF heating would also drift in the direction of the wind. Once the density depletion was significantly transported in longitude, the density gradients would not be strong enough to refract the heater ray, so the ray would snap back, resulting in a snapback of the heating location as well [2]. This was shown in a previous simulation study; however, they didn't use a realistic, self-consistent ionosphere [49].

Since the heating location changes as the ionospheric density depletion evolves, it is necessary to use a self-consistent model for HF heating to simulate this exper-

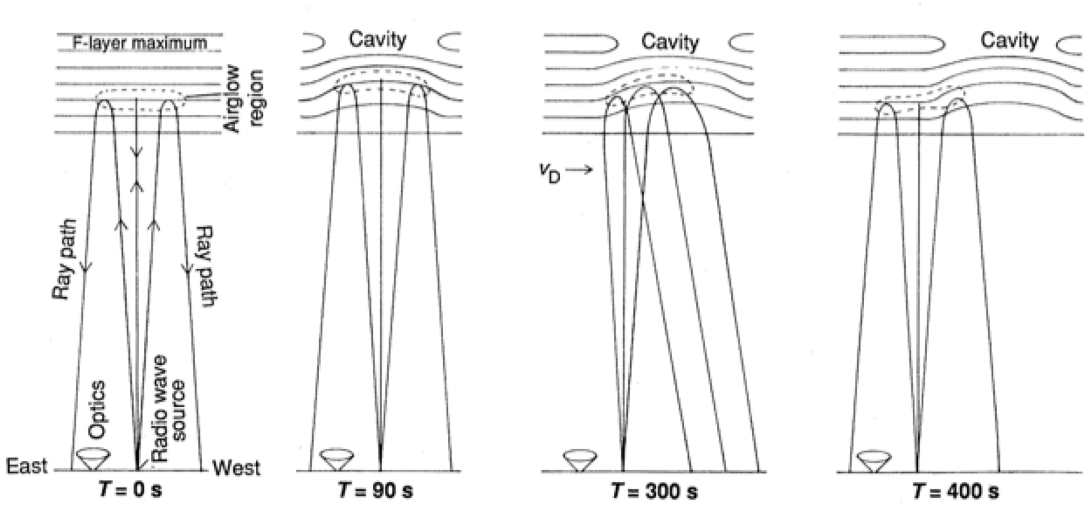


Figure 5.4: Outline of proposed snapback theory by [2]. As the electron density cavity drifts westward, the incoming HF heater rays are refracted in the same direction. Eventually the cavity drifts out of range, diminishing the horizontal density gradients such that incoming HF heater rays are no longer refracted westward and they "snapback" to their original ray paths. (Reproduced from [2])

iment. We have developed a new HF heating model that couples a first principles ionosphere model, SAMI3/ESF with a raytrace model, MoJo. At each output time step (about 1 minute) the MoJo ray race code is run in order to determine the latitude, longitude and altitude of the HF heating. This input is fed into the electron temperature equation which simulates HF heating.

The full SAMI3/ESF electron temperature equation is described in Chapter 3. Once again, we also use a Gaussian-shaped source term to simulate artificial HF heating in the ionosphere:

$$Q_{RF} = \left(\frac{dT_e}{dt}\right)_0 \exp[-(z-z_0)^2/\Delta z^2] \exp[-(\theta-\theta_0)^2/\Delta\theta^2] \exp[-(\phi-\phi_0)^2/\Delta\phi^2] \quad (5.1)$$

The heating source term is calculated at each gridpoint, thus z is the altitude of the gridpoint, $\theta$ the latitude, and $\phi$ the longitude. In Eq. (5.1), $(dT_e/dt)_0$ is the total heating rate per electron in K/s. The other parameters are the center altitude of the heating location $z_0$; the vertical extent of the heated region, $\Delta z$; the center latitude of the heating location, $\theta_0$; the latitudinal extent of the heated region, $\Delta\theta$; the center longitude of the heating location, $\phi_0$; and the longitudinal extent of the heated region, $\Delta\phi$. Note that the non-local transport effects of accelerated suprathermal electrons are neglected.

Unlike Chapter 4, where the heating location was fixed, the heating location changes at each time step. At each user-defined time step MoJo is run using the updated electron density. Then the average heating location is determined by calculating the altitude where the ray is between the upper hybrid altitude and the plasma frequency altitude. In this region, electrons are accelerated by Langmuir

waves with the electric field vector (**E**) parallel to the magnetic field (**B**) at the reflection point. The upper hybrid altitude is defined by the following condition: $\omega = [\omega_p^2(z_0 - \Delta z) + \omega_{ecf}^2]^{1/2}$ where $\omega$ is the input angular wave frequency, $\omega_p$ is the plasma frequency at the altitude $z_0 - \Delta z$, and $\omega_{ecf}$ is the electron cyclotron frequency. The plasma frequency altitude is defined as the altitude where the plasma frequency is equal to the input wave frequency. The average latitude, longitude, and altitude are taken as the lat0, lon0 and alt0 heating parameters in Eq. (5.1). Thus, as ionosphere evolves due to the HF heating, the location of further HF heating is modified.

## 5.3 Simulations of the Snapback Effect

In order to demonstrate and explain the physical mechanism behind the snapback phenomenon, the coupled model is run using initial conditions similar to that of the original snapback experiment. For the transmitter location, we choose a longitude of 0° and the magnetic latitude of the Arecibo Observatory, which is approximately 28°. In Equation 5.1 the altitude range is set to $\Delta z = 10$ km, based on output from test runs. The latitudinal extent of the heated region is set to $\Delta\theta = .25°$ and the longitudinal extent is set to $\Delta\phi = .25°$.

For the initial state of SAMI3/ESF, we use output from a 48-hour run of the SAMI2 model with the following conditions: $F_{10.7} = 100$, $F_{10.7}A = 100$, Ap = 4, and day of year = 130. The simulation includes geographic longitudes from ±2°, so universal time and local time are the same. The plasma is modeled from ±35°

magnetic latitude. The plasma parameters at 00:00 UT of the second day are used to initialize the 3D model. The $F$ peak maximum electron density above Arecibo is taken as $2.9 \times 10^5$ cm$^{-3}$, which corresponds to a critical frequency of about 4.8 MHz. Each simulation starts at 0:00; at 1:00 the artificial heater is turned on and it heats continuously for 30 minutes.

First we examine a simulation with a median value (60 m/s) for the zonal neutral wind. As in previous studies we estimate the total heating rate per electron to be approximately 1000 K/s [57]. The input heater frequency is 4.4 MHz, just below the critical frequency.

The left column of Figure 5.5 shows optical data of airglow clouds observed in an Arecibo experiment [2]. The 630.0 nm emissions are from the $O(^1D)$ state of atomic oxygen, which is formed by inelastic collisions with electrons whose energies are above 2 eV. The electrons are accelerated by the electric potential associated with plasma waves that are generated by the transmitted pump wave near the reflection altitude as part of anomalous absorption. The relevant reactions are:

$$e* + O(^3P) \rightarrow e + O(^1D) \tag{5.2}$$

$$O(^1D) \rightarrow O(^3P) + h\nu \tag{5.3}$$

SAMI3 does not model this type of enhanced airglow, so it is necessary to use the electron temperature as a proxy. The right-hand column shows the electron temperature as a function of latitude and longitude at 310 km altitude for

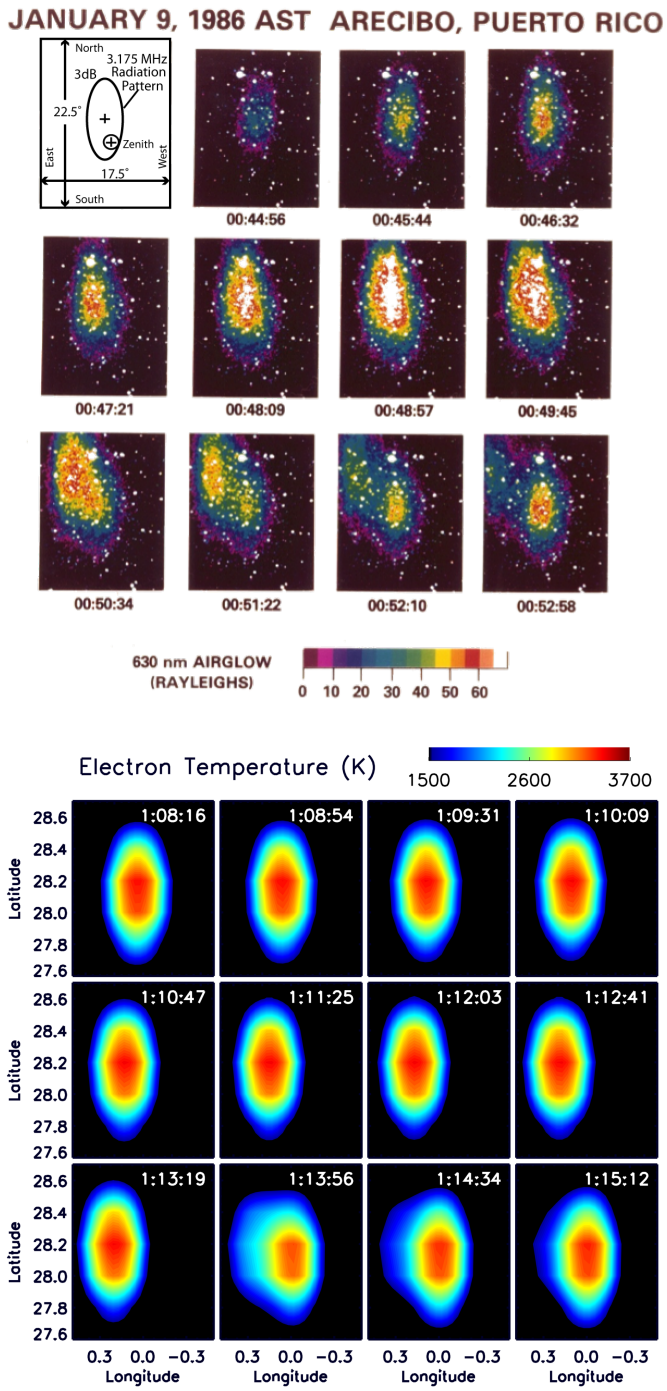


Figure 5.5: The top row shows 630 nm airglow from a 1986 experiment at Arecibo. The bottom row shows contour plots of the modeled electron temperature as a function of longitude and latitude at 310 km altitude at different times during the artificial heating. The heating starts at 1:00, and the initial heated area is around 0° longitude. As time progresses, the heated area moves eastward in longitude (to the left) due to the zonal wind. After approximately 15 minutes, the heated area snaps back to roughly the original heating longitude.

different times during the HF heating. In both the data and the simulation, the heating location drifts eastward (left) in longitude. Initially the heating location is approximately 0° longitude. The heating location reaches its maximum change in the heating longitude at 1:13:19 (bottom left corner). Less than a minute later (bottom row, 2nd column on the left) the heating location has snapped back to about 0° longitude.

Figure 5.6 shows the logarithmic electron density ($cm^{-3}$) as a function of longitude and altitude. The calculated ray path is shown in blue; the transmitter is at 0° longitude, so the ray path originates on the left hand side, then reflects and propagates back towards the Earth on the right-hand side. The portion of the ray path that passes through the region where anomalous absorption occurs is highlighted in yellow. The density range for anomalous absorption is also outlined by the black solid lines. The top row shows a simulation where the heater continuously turned on; the bottom row shows a simulation where the heater is turned off at 1:15.

In both simulations, the heating location at the onset of artificial HF heating is around 0° longitude. The density gradient in the longitude direction due to the zonal winds causes the ray path to be refracted eastward in longitude, away from the transmitter. Thus, as the heating continues, the heating location also drifts eastward in longitude. At 1:13 (middle panel), the density cavity drifts into the path of the refracted heater beam and only a small part of it near the original heating location is in the appropriate density range for anomalous absorption. Thus, the heating location, "snaps back" to the original location. In the case of continuous heating (top panel), this cycle continues, and the heating location drifts eastward

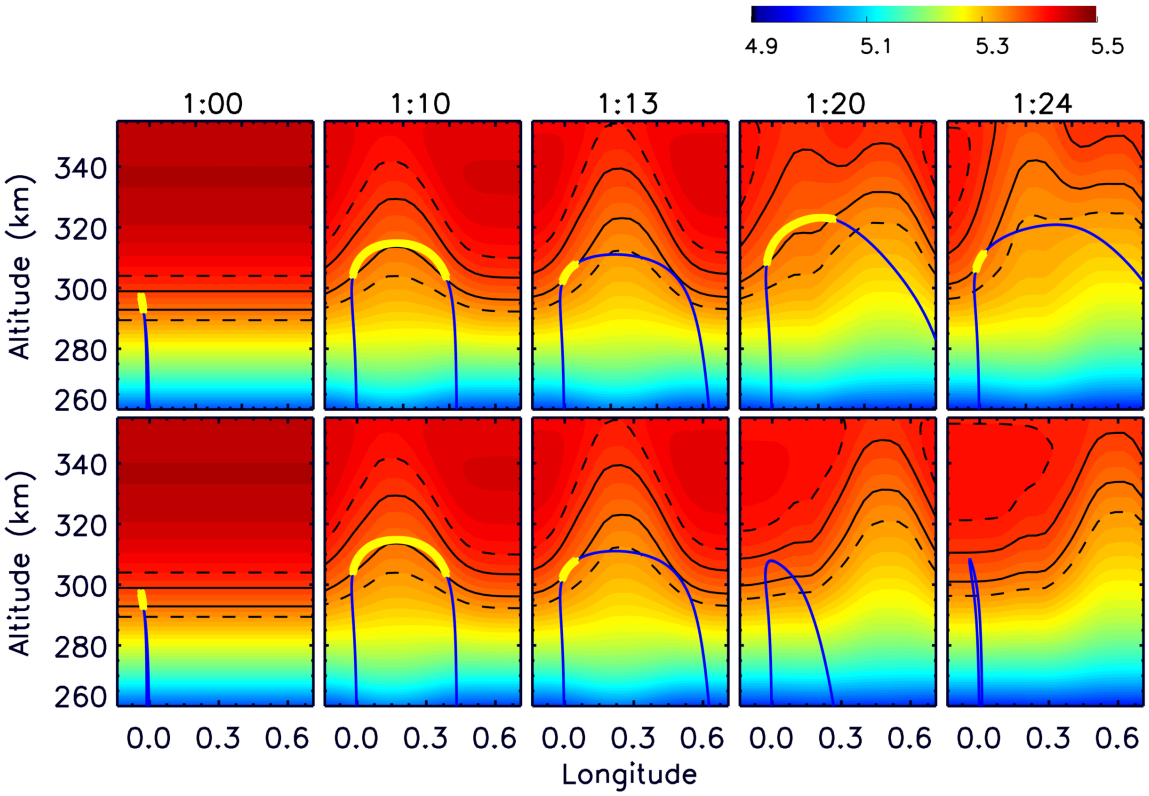


Figure 5.6: Contour plots of logarithmic electron density ($cm^{-3}$) as a function of longitude and altitude. The black solid lines outline the density range where anomalous absorption occurs. The blue line is the ray path of the heater at that time. The portion of the ray path that passes through the anomalous absorption zone is highlighted in yellow. The top row shows different times for a simulation with the heater constantly on. In this case the heating location snaps back (middle and far right panels), but the ray does not because of the continuous horizontal density gradient. The bottom row shows the same times for a simulation where the heater is turned off at 1:15. After the heater is turned off, the horizontal gradient diminishes and the ray path snaps back.

in longitude until the density cavity drifts into the path of the ray, causing another snap back.

Figure 5.7 shows the same effect in three dimensions. The red contour outlines where the electron density is equal to the upper hybrid resonance, which is the lower limit for anomalous absorption. The black line traces the ray through the ionosphere; whenever it is above the red contour, it is in the electron density range where anomalous absorption occurs. The top panel shows the configuration at 1:20, before the snapback; in this case the ray is in the range for anomalous absorption for a range of longitudes. The bottom panel shows the configuration after snapback at 1:24. In this case, the density hole is wider and the portion of the ray that reaches the density range for anomalous absorption is less extended in longitude.

This is different from the explanation of the physical mechanism originally provided by [2], who hypothesized that the density gradients due to the cavity would weaken as the winds transported the cavity longitudinally so that the ray would no longer refract and the entire ray path would snap back to the original ray path. In the simulations, we have found that while the heating location snaps back, the ray path itself does not. This is due to the horizontal gradient in the electron density around 0° longitude, which causes the ray to refract towards the region of lower electron density. As the heater is on continuously, this horizontal gradient is consistently present, and the ray does not snap back. Once the heater is turned off, such as at 1:15 (bottom row), the longitudinal electron density gradient decreases and the ray path snaps back to the original ray path.

In Figure 5.5, both the observations and the simulation indicate that some

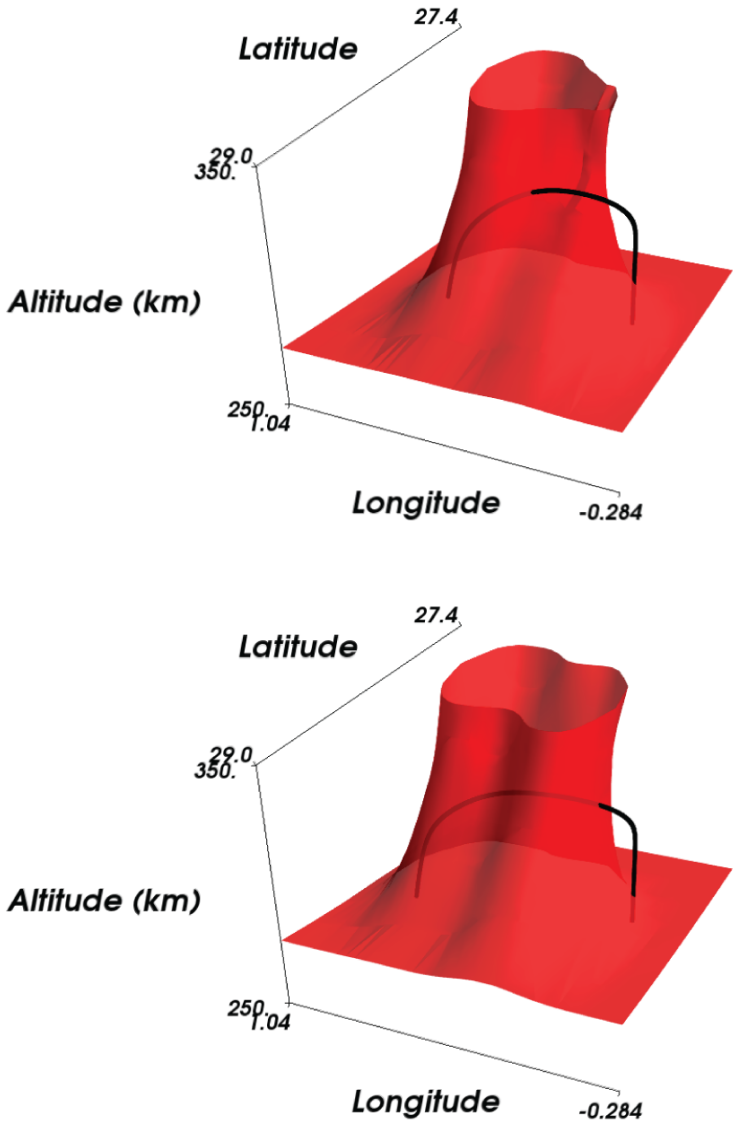


Figure 5.7: Three dimensional plots that show the configuration before (top panel) and after snapback (bottom panel). The red contour outlines the lower limit of the electron density range where anomalous absorption occurs. The heating region can be found by determining where the ray is outside of the contour.

residual electron heating remains after the heating location snapped back to the original location. This is seen particularly at times 1:13:56 and 1:14:34 in the simulation (middle two panels in the bottom row). The snapback in the observations occurs more quickly after heating onset than in the simulation. In the observations, the snapback occurs only 8 minutes after onset heating, whereas in the simulation it occurs 15 minutes after the heating starts. A possible explanation for this is that the neutral wind was faster than 60 m/s during the time of the experiment. Figure 5.8 shows the heating longitude as a function of time for three different zonal wind speeds. The faster the zonal wind speed, the more quickly the snapback occurs. Note that if the entire ray path drops below the range for anomalous absorption, the simulated HF heating automatically stops; this can cause interruptions in the line showing the heating longitude.

It should be noted that the input heater frequency needs to be slightly increased to obtain an equivalent maximum heating longitude for a larger zonal wind. This has implications for how to suppress snapback. Figure 5.9 shows plots of the heating longitude as a function of time for two cases. The left panel shows a set of simulations run with an input frequency of 4.4 MHz, and a zonal neutral wind of 60 m/s; as we see, the stronger the heater input is, the larger the variation in heating longitude. The right panel shows a set of simulations with varying input frequencies, a fixed heating rate of 1000 K/s, and a zonal wind of 60 m/s. In this case, the larger the input frequency, the larger the variation in heating longitude. This implies that in order to suppress the snapback, or to create a steady state heating location, one could either reduce the power and/or frequency of an HF heater.

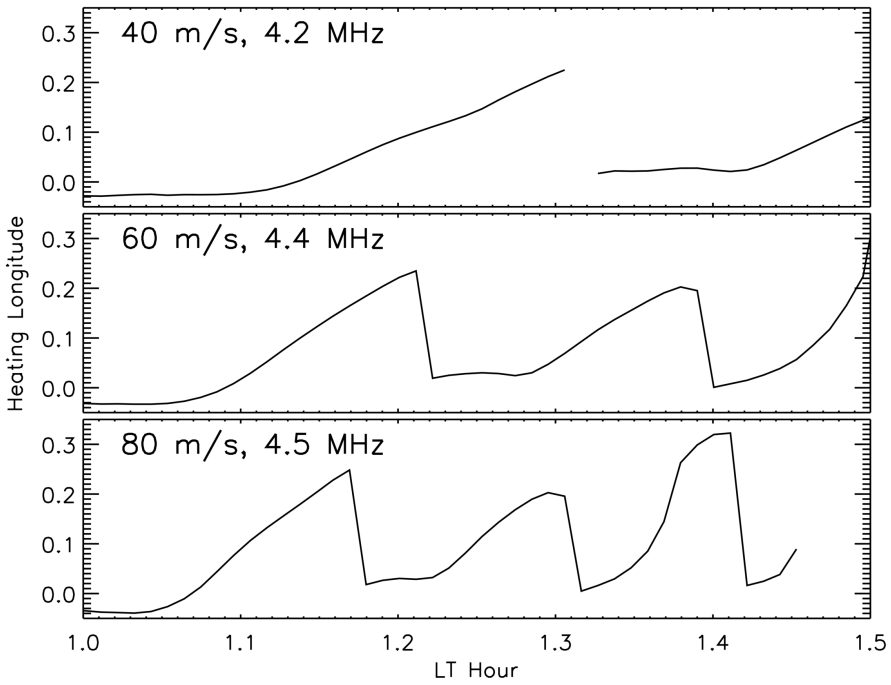


Figure 5.8: The heating longitude as a function of time for simulations with different zonal wind speeds illustrates the effect of wind speed on the frequency of snapback. Note that to obtain equivalent perturbed heating longitudes it is necessary to use a higher frequency for faster zonal winds.

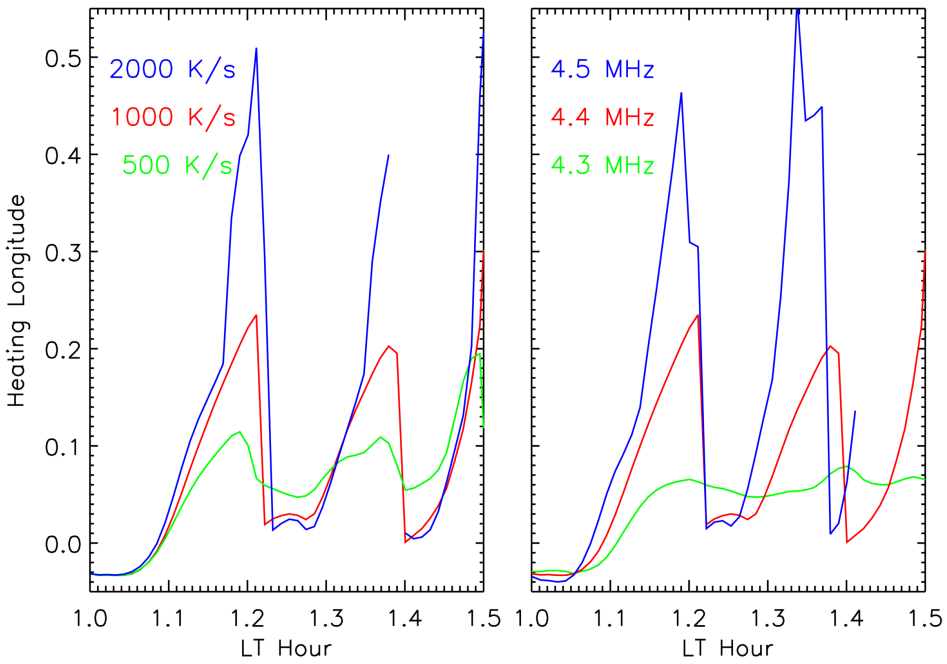


Figure 5.9: The heating longitude as a function of time for a constant zonal wind of 60 m/s. The left panel shows the variation in heating longitude for different heater powers with a fixed 4.4 MHz frequency: the stronger electron heating rate leads to larger fluctuations in the heating longitude. The right panel shows the variation in heating longitude for different input frequencies with a constant electron heating rate (1000 K/s): higher frequencies result in larger displacement in the heating longitude.

## 5.4 Discussion

We have coupled a first principles ionosphere model (SAMI3/ESF) with a raytrace model (MoJo) in order to self-consistently calculate HF heating. We have found good agreement with an early Arecibo experiment [2] and explained the physical mechanism responsible for the snapback effect. HF heating creates a plasma depletion in the ionosphere, which in turn affects the input HF heater wave. When a zonal neutral wind is present, the shape of the cavity becomes antisymmetric in longitude due to the depletion drifting in the same direction as the neutral wind. The HF heater rays are subsequently refracted in the same direction. Eventually the cavity convects into the path of the ray such that the majority of the ray path passes through a region where the electron density is too low for anomalous absorption and the heating location appears to snap back.

The frequency of snapback is dependent on the speed of the zonal neutral wind. Snapbacks occur more frequently for faster zonal winds. The input power and frequency are shown to affect the range in heating longitude values. The higher the power/frequency, the farther the HF rays refract and heat other longitudes. This has implications for new HF heating systems that are developed in the future, since in most cases it is desirable for the heater to work in steady state conditions where the heating location is not constantly changing. The snapback effect may be suppressed if the heater input power and/or frequency is reduced, which indicates that new heaters with flexible transmission power and frequency are essential for efficient heating in the low and middle latitudes. It should be noted that the maximum

useable frequency for steady state artificial HF heating is dependent on the wind speed; a higher maximum useable frequency is available for faster winds.

The next step in HF interactions modeling is to propagate multiple rays and calculate the ray convergence (or divergence) to better determine the power in the ionospheric regions. Large-scale self-focusing (see, [1]) is the first step in creating large-scale plasma cavities responsible for the HF snapback effects. This is followed by Fresnel diffraction of the wave into smaller kilometer-scale filaments. At some point, a full-wave treatment may be attempted but the geometric-optics approach used in this paper is adequate for large-scale ionospheric modifications. Another possible enhancement would be to use the ray path to calculate the width ($\Delta z$, $\Delta\theta$ and $\Delta\phi$) of the heating region, which was constant for this study. A more self-consistent method could use an approach where the width of the heated location in latitude, longitude, and altitude changes as the ray path does. A simple version of this was examined where 5 rays were used in order to determine the heating area and the results were not significantly different from those described in this paper. Lastly, we note that this model could be useful to guide and interpret future experiments at Arecibo with the new heater facility.

# Chapter 6: Summary

Artificial heating experiments allow scientists to treat the ionosphere as an open plasma laboratory, however, unlike a confined laboratory, the ionosphere has unique dynamics and irregularities that complicate the use of HF propagation and heating. This thesis exploits the capabilities of high-fidelity 3D models to study the effects of the ionosphere on radio wave propagation and heating.

Chapter 3 presented the first study to use a realistic, full-physics, time-dependent ionospheric model in conjunction with a full-physics 3D raytrace code to examine the effect of ionospheric density gradients generated by MSTIDs on HF radio wave propagation. From calculating the spatiotemporal evolution of high-angle-of-incidence HF ionospheric sounding observables, it was determined that horizontal gradients have a profound effect on the path of the radio waves through the ionosphere and that the resultant out-of-plane propagation cannot be accurately modeled assuming 2D propagation.

The study also utilized a new technique of mapping a mesh of ray fans to study the influence of MSTID propagation on the set of all possible transmission paths to the ground from a given receiver. It was concluded that the occurrence of three eigenrays is common due to the horizontal gradients that occur due to the MSTIDs.

In addition, one of the assumptions of HF Doppler systems that are being developed and deployed to detect MSTIDs in the ionosphere is that the ray path does not vary significantly as a function of time; we have found that this assumption is incorrect, as the reflection location of the ray paths varied by as much as 100 km during the course of the simulation. Future work should include the modeling of HF Doppler to determine the validity of a fixed ray path assumption in the interpretation of HF Doppler signals.

Chapter 4 examined the question of whether the density perturbations created by artificial HF heating could generate an ESF bubble. It was concluded that it was unlikely that HF heating could generate an ESF bubble since the density depletions created by HF heating were surrounded by local increases in the electron density; in other words, the plasma was simply redistributed along the magnetic field line. Since the plasma along the field was not actually depleted, the Pedersen conductivity did not decrease, the growth rate remained unchanged, and no ESF bubble formed in the ionosphere. This conclusion was determined to hold for various other simulation parameters including: modified beam width, modified timing and/or duration of HF heating, modulated heating, smaller/larger heating rates, different heating location along the magnetic field, and the inclusion of neutral winds.

It was also determined that HF heating could not suppress ESF bubbles. There is future work to be done in this area, however, because while the addition of HF heating was unable to short circuit an already forming bubble, it may be possible to neutralize the initial density perturbations, such as gravity waves, that trigger the instability.

Chapter 5 utilized the first self-consistent model of HF heating to simulate the observations of the "snapback" effect from an Arecibo HF heating experiment. In addition, the physical mechanism for the snapback was determined: HF heating creates a density cavity in the ionosphere that becomes antisymmetric during the artificial heating due to the influence of the zonal neutral wind. The horizontal gradients from the cavity refract the HF heater rays so that they follow the drifting bubble in the same direction as the zonal neutral wind. Eventually the cavity is depleted enough that the HF heater rays no longer pass through a region with densities sufficient for anomalous absorption and the heating location appears to snap back.

The frequency of the snapback was shown to be dependent on the speed of the zonal neutral wind, with snapbacks occurring more frequently for higher wind speeds. The input power and frequency affect the spread in possible heating longitudes. By decreasing the input power and/or the frequency a steady state can be obtained, where the heating location no longer changes as a function of time. This implies that future HF heating systems should be developed with variable input powers and frequencies so that they may obtain steady state heating conditions regardless of the zonal neutral wind speed. Future work in this area should focus on propagating multiple rays in order to calculate the convergence or divergence of the rays, so that the power delivered to ionospheric regions can be determined.

# Appendix A: MoJo

## A.1 Overview

MoJo (Modernized Jones) is based on the original Jones-Stephenson (1975) raytracing code. While the code has been updated to take advantage of modern computational techniques, it retains the same general structure and equations as the original code.

The general problem of raytracing is: given a wave frequency, wave mode (O-mode or X-mode), and an initial direction, to determine the path of the wave through the ionosphere. In order to solve this problem, the general method is to numerically integrate Hamilton's equations, which define how the position of the wave and the wave propagation vector, $\mathbf{k}$, change along the path. In order to integrate the equations, at every point along the path, we need to know the coordinates, the electron density and its derivatives, and also the magnetic field and the collision frequency at that particular point in space. Once these parameters have been determined, the derivatives of these equations are calculated and the numerical integrator propagates forward in time.

## A.2 Basic Symbols

Following is a list of the basic symbols and notation used in this Appendix.

| | |
|---|---|
| $B_0$ | Magnetic Induction of Earth's Magnetic Field |
| $c$ | Speed of Light in a Vacuum |
| $e$ | Charge of the Electron |
| $f$ | Wave Frequency |
| $f_H = \frac{eB_0}{2\pi m}$ | Electron Cyclotron (gyro) Frequency |
| $f_N = \sqrt{\frac{n_e e^2}{4\pi^2 \epsilon_0 m}}$ | Plasma Frequency |
| $H$ | Hamiltonian |
| $\mathbf{k}$ | Propagation vector which is perpendicular to the wavefront. The magnitude is $2\pi/\lambda = \omega n/c$. |
| $k_r, k_\theta, k_\varphi$ | Components of the propagation vector in the $r$, $\theta$ and $\varphi$ directions. |
| $M$ | Mass of the electron |
| $n_e$ | Number of Electrons per Unit Volume |
| $n$ | Phase Refractive Index (complex) |
| $n'$ | Group Refractive Index (complex) |
| $P$ | Phase Path Length |
| $P'$ | Group Path Length ($P' = ct$) |
| $r, \theta, \varphi$ | The Spherical Polar Coordinates of a Point |
| $s$ | Geometric Ray Path Length |
| $t$ | Time |
| $U = 1 - iZ$ | Collisions |
| $V_r, V_\theta, V_\varphi$ | Components of the wave normal direction normalized so that $V_r^2 + V_\theta^2 + V_\varphi^2 = real(n^2)$ |
| $v$ | Phase velocity |
| $X$ | $\omega_N^2/\omega^2 = f_N^2/f^2$ |
| $Y$ | $\omega_H/\omega = f_H/f$ |
| $Z$ | $\nu/\omega$ |
| $\epsilon_0$ | Electric permittivity of free space |
| $\lambda$ | Wavelength |
| $\nu$ | Electron collision frequency |
| $\rho$ | Characteristic wave polarization |
| $\rho_L$ | Longitudinal polarization |
| $\tau$ | Independent variable in Hamilton's equation |
| $\psi$ | Angle between the wave normal and $-B_0$ |
| $\omega$ | $2\pi f$, angular wave frequency |
| $\omega_H$ | $2\pi f_H$, angular gyrofrequency |
| $\omega_N$ | $2\pi f_N$, angular plasma frequency |

## A.3 Input Parameters

In order to run MoJo there are a number of parameters that must be defined. The basic parameters are the wave frequency, the mode (O-mode or X-mode), the transmitter location, and the initial azimuth and elevation of the wave. In addition to this several fields must also be provided: the electron density, the magnetic field, and the collision frequency. The following sections describe in detail these quantities, their importance and how they are defined for use in MoJo.

### A.3.1 Electron Density

For high frequency waves, the electrons in the ionosphere are affected by the wave, whereas the ions are too heavy to respond. Thus, the ion density is not important, and it is only the electron density as a function of position that is required.

MoJo requires the electron density to be on a fixed latitude, longitude, altitude grid. MoJo then uses cubic interpolation to calculate the electron density and its derivatives at the given location. In general, the profile of the electron density is the most important factor when raytracing and determines where the ray reflects back towards the Earth. Horizontal gradients can factor in the path of the ray, especially if they occur near the reflection point of the wave.

The subroutine "electrons.f90" interpolates the electron density field to the given location and determines the derivatives. In general, instead of the electron density ($n_e$), the quantity $X = f_N^2/f^2$ and its derivatives are calculated, where $f$ is the input wave frequency and $f_N = (8.98e3/1 \times 10^6)\sqrt{n_e}$ is the plasma frequency in

MHz.

### A.3.2 Magnetic Field

The magnetic field is calculated in "magnfield.f90." The code calculates the strength and direction of the magnetic field at a given location using a harmonic analysis. Generally, the important calculation is for Y and its derivatives, where $Y = f_H/f$. Here, $f$ is the input wave frequency and $f_H = e|B_0|/m_e c$ is the electron gyro frequency. In order to update the magnetic field, one would need to update the subroutine.

The magnetic field introduces an anisotropy, or a preferred direction into the raytracing calculation. This causes the path to change depending on the initial polarization from the transmitter. If the radio waves from a transmitter are Left Hand Circularly Polarized (LHCP), then they are referred to as O-mode waves; if they are Right Hand Circularly Polarized (RHCP) then they are referred to as X-mode waves. At a given point in the plasma, the polarization depends only on the conditions at that point and not on how it got there. In the plane of the wavefront, both modes are circularly polarized. The ordinary wave is called "ordinary" because it reflects at the same height that it would if there were no magnetic field. The other wave solutions are called extraordinary waves. The O-mode wave tends to reflect when it is perpendicular to the magnetic field, and the X-mode tends to reflect parallel to the magnetic field. Without the magnetic field defined, there would be no difference between the O and X-modes.

### A.3.3 Collision Frequency

Collisions primarily serve as a source of absorption for the incoming EM wave. The electron-neutral collision frequency dominates at lower altitudes, but at higher altitudes, the electron-ion collision frequency dominates. In some cases, if the collision frequency is much larger than the input wave frequency, the collisions can affect the path of the ray as well, but this is not typically the case for high frequency waves, which range in frequency from about 3-30 MHz.

A default collision frequency can be used in MoJo (as it is in this work). In this case, for a given location, it can simply be calculated as follows:

$$\nu_e = \nu_{en}/e^{A_{en}(z-z_{en})} + \nu_{ei}/e^{A_{ei}(z-z_{ei})} \tag{A.1}$$

where $\nu_{en} = 5.0 \times 10^{11} s^{-1}$ is the electron-neutral collision frequency at the reference height $z_{en} = 0$ km, and $A_{en} = 1/6.5$ is the scale height for the electron-neutral collisions. For the electron-ion collisions: $\nu_{ei} = 1.0e3s^{-1}$ is the electron-ion collision frequency at $z_{ei} = 200$ km and $A = .01$ is the scale height.

The alternative is to calculate the collision frequency as a function of the electron density, electron temperature, and neutral densities. The collision frequency changes as a function of time, solar activity, time of year, and location, so it may be desired to use a more accurate equation. The equations for the collision frequencies are derived in [50].

## A.4 Ray Tracing Equations

### A.4.1 Numerical Integration

The numerical integrator used in this work is the standard Runge-Kutta 4th order integrator. MoJo includes a standard Fortran subroutine for the Runge-Kutta called RK4. The integrator requires both the current value and the derivative in order to integrate along the ray path. The Hamilton subroutine provides the derivatives necessary for the integration. Another variable step Adams-Moulton predictor-corrector method is provided, but it is not used for this work.

### A.4.2 Hamilton's Equations

In order to calculate the ray path, we numerically integrate Hamilton's equations. These equations are calculated in the "hamilton.f90" subroutine. Note that the actual Hamiltonian, its derivatives, the phase refractive index, and its derivatives are all calculated in the Appleton-Hartree subroutine.

The variables that must be solved for are the spherical coordinates of each point along the ray path (r, $\theta, \phi$), the propagation vector with components $k_r$, $k_\theta$, $k_\varphi$, which are normalized so that in free space ($k_r^2 + k_\theta^2 + k_\varphi^2 = \omega^2/c^2$), as well as the time (t) and the angular frequency of the wave ($\omega = 2\pi f$). In spherical polar coordinates, Hamilton's eight equations can be defined as follows:

$$\frac{dr}{d\tau} = \frac{\partial H}{\partial k_r} \tag{A.2}$$

$$\frac{d\theta}{d\tau} = \frac{1}{r}\frac{\partial H}{\partial k_\theta} \tag{A.3}$$

$$\frac{d\varphi}{d\tau} = \frac{1}{r\sin\theta}\frac{\partial H}{\partial k_\varphi} \tag{A.4}$$

$$\frac{dt}{d\tau} = -\frac{\partial H}{\partial \omega} \tag{A.5}$$

$$\frac{dk_r}{d\tau} = -\frac{\partial H}{\partial r} + k_\theta\frac{d\theta}{d\tau} + k_\phi\sin\theta\frac{d\varphi}{d\tau} \tag{A.6}$$

$$\frac{dk_\theta}{d\tau} = \frac{1}{r}(-\frac{\partial H}{\partial \theta} - k_\theta\frac{dr}{d\tau} + k_\varphi r\cos\theta\frac{d\varphi}{d\tau}) \tag{A.7}$$

$$\frac{dk_\varphi}{d\tau} = \frac{1}{r\sin\theta}(-\frac{\partial H}{\partial \varphi} - k_\varphi\sin\theta\frac{dr}{d\tau} - k_\varphi r\cos\theta\frac{d\theta}{d\tau}) \tag{A.8}$$

$$\frac{d\omega}{d\tau} = \frac{\partial H}{\partial t} \tag{A.9}$$

Note that in the above equations, $\tau$ is parameter that depends on the choice of Hamiltonian. Also, in Equation A.5, $t$ is the propagation time of a wave packet, whereas in Equation A.9 it simply expresses the time variation of a time varying medium.

For the actual calculations we modify Hamilton's equations so that the group path ($P' = ct$) is used as the independent variable. The derivatives with respect to the group path do not depend on the Hamiltonian. Thus, by using it as the

independent variable, we could switch Hamiltonians in the middle of a path. It should also be noted that this will force the program to take smaller steps in real path length near the reflection point. To derive the modified Hamilton equations, we divide the equations 1-3 and 5-7 in the previous section by c times the 4th equation. The six modified equations are:

$$\frac{dr}{dP'} = -\frac{1}{c}\frac{\partial H/\partial k_r}{\partial H/\partial \omega} \tag{A.10}$$

$$\frac{d\theta}{dP'} = -\frac{1}{rc}\frac{\partial H/\partial k_\theta}{\partial H/\partial \omega} \tag{A.11}$$

$$\frac{d\varphi}{dP'} = \frac{1}{rc\sin\theta}\frac{\partial H/\partial k_\varphi}{\partial H/\partial \omega} \tag{A.12}$$

$$\frac{dk_r}{dP'} = \frac{1}{c}\frac{\partial H/\partial r}{\partial H/\partial \omega} + k_\theta\frac{d\theta}{dP'} + k_\phi sin\theta\frac{d\varphi}{dP'} \tag{A.13}$$

$$\frac{dk_\theta}{dP'} = \frac{1}{r}\left(\frac{1}{c}\frac{\partial H/\partial \theta}{\partial H/\partial \omega} - k_\theta\frac{dr}{dP'} + k_\varphi r\cos\theta\frac{d\varphi}{dP'}\right) \tag{A.14}$$

$$\frac{dk_\varphi}{dP'} = \frac{1}{r\sin\theta}\left(\frac{1}{c}\frac{\partial H/\partial \varphi}{\partial H/\partial \omega} - k_\varphi\sin\theta\frac{dr}{dP'} - k_\varphi r\cos\theta\frac{d\theta}{dP'}\right) \tag{A.15}$$

## A.5 The Appleton-Hartree Formulation

Generally, the dispersion relation is written in the form:

$$H = constant \tag{A.16}$$

Then H is taken as the Hamiltonian, which, at each point along the path of the ray, is ensured to be a constant because of Hamilton's equations. Losses do not have a large effect on the path of HF radio waves; they mainly cause attenuation of the signal.

It should be noted that in an absorbing medium the dispersion relation will be complex, this will lead to a complex Hamiltonian and the resulting ray paths calculated with Hamilton's equations will have complex coordinates. This is called raytracing in complex space and it is an extension of the phase integral method [5]. This may be required to calculate propagation for low-mid frequencies. This dissertation deals with HF ray tracing, but the code still performs the calculations in complex space.

The Appleton-Hartree formulation is contained in a separate subroutine that calculates the Hamiltonian and its partial derivatives. In addition, each version calculates $n^2$, $nn'$, $n\ \partial n/\partial r$, $n\ \partial n/\partial\theta$, $n\ \partial n/\partial\varphi$, $n\ \partial n/\partial V_r$, $n\ \partial n/\partial V_\theta$, $n\ \partial n/\partial V_\varphi$, $n\ \partial n/\partial t$, and the polarization. Here, n is the complex phase refractive index, $n'$ is the complex group refractive index, r, $\theta$, and $\varphi$ are the spherical polar coordinates of a point along the ray path, and $V_r$, $V_\theta$, $V_\varphi$ are the components of the wave normal direction.

The following Hamiltonian is used:

$$H = \frac{1}{2}\left(\frac{c^2}{\omega^2}(k_r^2 + k_\theta^2 + k_\varphi^2) - n^2\right) \tag{A.17}$$

The square of the index of the phase refractive index (which is complex) is

defined as:

$$n^2 = 1 - 2X\frac{1 - iZ - X}{2(1 - iZ)(1 - iZ - X) - Y_T^2 \pm \sqrt{Y_T^4 + 4Y_L^2(1 - iZ - X)^2}} \tag{A.18}$$

where:

$$X = \frac{\omega_p^2}{\omega^2}; \quad Y = \frac{\omega_{ecf}}{\omega}; \quad Y_T = Y\sin\psi; \quad Y_L = Y\cos\psi; \quad Z = \frac{\nu_e}{\omega} \tag{A.19}$$

In the above, $f_N$ is the plasma frequency, $f_H$ is the electron gyrofrequency, $\nu_e$ is the electron collision frequency, $f$ is the wave frequency, and $\psi$ is the angle between the direction of the wave normal and the Earth's magnetic field.

These are the equations that are calculated in this subroutine.

$$V^2 = V_r^2 + V_\theta^2 + V_\varphi^2 \tag{A.20}$$

$$V \cdot Y = V_r Y_r + V_\theta Y_\theta + V_\varphi Y_\varphi \tag{A.21}$$

$$\frac{Y_L}{V} = \frac{V \cdot Y}{V^2} \tag{A.22}$$

$$Y_L^2 = \frac{(V \cdot Y)^2}{V^2} \tag{A.23}$$

$$Y_T^2 = Y^2 - Y_L^2 \tag{A.24}$$

$$Y_T^4 = (Y_T^2)^2 \tag{A.25}$$

$$U = 1 - iZ \tag{A.26}$$

Note: in the following equation, the plus is for the O-mode, and minus for the X-mode.

$$RAD = \pm\sqrt{Y_T^4 + 4Y_L^2(U-X)^2} \tag{A.27}$$

$$D = 2U(U-X) - Y_T^2 + RAD \tag{A.28}$$

$$n^2 = 1 - \frac{2X(U-X)}{D} \tag{A.29}$$

$$\frac{n}{Y_L Y_T}\frac{\partial n}{\partial \psi} = \frac{2X(U-X)\left(-1 + \frac{Y_T^2 - 2(U-X)^2}{RAD}\right)}{D^2} \tag{A.30}$$

$$Y_T Y_L \frac{\partial \psi}{\partial r} = \frac{Y_L^2}{Y}\frac{\partial Y}{\partial r} - \left(V_r \frac{\partial Y_r}{\partial r} + V_\theta \frac{\partial Y_\theta}{\partial r} + V_\varphi \frac{\partial Y_\varphi}{\partial r}\right)\left(\frac{Y_L}{V}\right) \tag{A.31}$$

$$Y_T Y_L \frac{\partial \psi}{\partial \theta} = \frac{Y_L^2}{Y}\frac{\partial Y}{\partial \theta} - \left(V_r \frac{\partial Y_r}{\partial \theta} + V_\theta \frac{\partial Y_\theta}{\partial \theta} + V_\varphi \frac{\partial Y_\varphi}{\partial \theta}\right)\left(\frac{Y_L}{V}\right) \tag{A.32}$$

$$Y_T Y_L \frac{\partial \psi}{\partial \varphi} = \frac{Y_L^2}{Y}\frac{\partial Y}{\partial \varphi} - \left(V_r \frac{\partial Y_r}{\partial \varphi} + V_\theta \frac{\partial Y_\theta}{\partial \varphi} + V_\varphi \frac{\partial Y_\varphi}{\partial \varphi}\right)\left(\frac{Y_L}{V}\right) \tag{A.33}$$

$$n\frac{\partial n}{\partial X} = -\frac{2U(U-X)^2 - Y_T^2(U-2X) + \frac{Y_T^4(U-2X) + 4Y_L^2(U-X)^3}{RAD}}{D^2} \tag{A.34}$$

$$n\frac{\partial n}{\partial Y} = \frac{2X(U-X)}{D^2 Y}\left(-Y_T^2 + \frac{Y_T^4 + 2Y_L^2(U-X)^2)}{RAD}\right) \tag{A.35}$$

$$n\frac{\partial n}{\partial Z} = \frac{iX}{D^2}\left(-2(U-X)^2 - Y_T^2 + \frac{Y_T^4}{RAD}\right) \tag{A.36}$$

$$n\frac{\partial n}{\partial r} = n\frac{\partial n}{\partial X}\frac{\partial X}{\partial r} + n\frac{\partial n}{\partial Y}\frac{\partial Y}{\partial r} + n\frac{\partial n}{\partial Z}\frac{\partial Z}{\partial r} + \frac{n}{Y_L Y_T}\frac{\partial n}{\partial \psi}Y_L Y_T \frac{\partial \psi}{\partial r} \tag{A.37}$$

$$n\frac{\partial n}{\partial \theta} = n\frac{\partial n}{\partial X}\frac{\partial X}{\partial \theta} + n\frac{\partial n}{\partial Y}\frac{\partial Y}{\partial \theta} + n\frac{\partial n}{\partial Z}\frac{\partial Z}{\partial \theta} + \frac{n}{Y_L Y_T}\frac{\partial n}{\partial \psi}Y_L Y_T \frac{\partial \psi}{\partial \theta} \tag{A.38}$$

$$n\frac{\partial n}{\partial \varphi} = n\frac{\partial n}{\partial X}\frac{\partial X}{\partial \varphi} + n\frac{\partial n}{\partial Y}\frac{\partial Y}{\partial \varphi} + n\frac{\partial n}{\partial Z}\frac{\partial Z}{\partial \varphi} + \frac{n}{Y_L Y_T}\frac{\partial n}{\partial \psi}Y_L Y_T \frac{\partial \psi}{\partial \varphi} \tag{A.39}$$

$$n\frac{\partial n}{\partial V_r} = \frac{n}{Y_T Y_L}\frac{\partial n}{\partial \psi}\left(\frac{V_r Y_L^2}{V^2} - \left(\frac{Y_L}{V}\right)Y_r\right) \tag{A.40}$$

$$n\frac{\partial n}{\partial V_\theta} = \frac{n}{Y_T Y_L}\frac{\partial n}{\partial \psi}\left(\frac{V_\theta Y_L^2}{V^2} - \left(\frac{Y_L}{V}\right)Y_\theta\right) \tag{A.41}$$

$$n\frac{\partial n}{\partial V_\varphi} = \frac{n}{Y_T Y_L}\frac{\partial n}{\partial \psi}\left(\frac{V_\varphi Y_L^2}{V^2} - \left(\frac{Y_L}{V}\right)Y_\varphi\right) \tag{A.42}$$

$$nn' = n^2 - \left(2Xn\frac{\partial n}{\partial X} + Yn\frac{\partial n}{\partial Y} + Zn\frac{\partial n}{\partial Z}\right) \tag{A.43}$$

$$\frac{\partial n}{\partial t} = \frac{\partial n}{\partial X}\frac{\partial X}{\partial t} \tag{A.44}$$

The polarization is defined as:

$$\rho = -i\frac{(-Y_T^2 + RAD)\sqrt{V^2}}{2(U-X)V \cdot Y} \tag{A.45}$$

The longitudinal polarization (from Budden 1961 page 49):

$$\rho_L = \frac{iX\sqrt{Y_T^2}}{(U-X)(U+i\frac{V \cdot Y}{\sqrt{V^2}}\rho)} \tag{A.46}$$

Once the other variables have been calculated, the derivatives of the Hamiltonian are calculated:

$$\frac{\partial H}{\partial t} = -n\frac{\partial n}{\partial t} \tag{A.47}$$

$$\frac{\partial H}{\partial r} = -n\frac{\partial n}{\partial r} \tag{A.48}$$

$$\frac{\partial H}{\partial \theta} = -n\frac{\partial n}{\partial \theta} \tag{A.49}$$

$$\frac{\partial H}{\partial \varphi} = -n\frac{\partial n}{\partial \varphi} \tag{A.50}$$

$$\frac{\partial H}{\partial \omega} = -\frac{nn'}{\omega} \tag{A.51}$$

$$\frac{\partial H}{\partial k_r} = \frac{c^2}{\omega^2}k_r - \frac{c}{\omega}n\frac{\partial n}{\partial V_r} \tag{A.52}$$

$$\frac{\partial H}{\partial k_\theta} = \frac{c^2}{\omega^2}k_\theta - \frac{c}{\omega}n\frac{\partial n}{\partial V_\theta} \tag{A.53}$$

$$\frac{\partial H}{\partial k_\varphi} = \frac{c^2}{\omega^2} k_\varphi - \frac{c}{\omega} n \frac{\partial n}{\partial V_\varphi} \tag{A.54}$$

$$\vec{k} \cdot \frac{\partial H}{\partial \vec{k}} = k_r \frac{\partial H}{\partial k_r} + k_\theta \frac{\partial H}{\partial k_\theta} + k_\varphi \frac{\partial H}{\partial k_\varphi} = n^2 \tag{A.55}$$

$$n' = n + f \frac{dn}{df} = n + \omega \frac{dn}{d\omega} \tag{A.56}$$

$n'$ is the group refractive index. $V_r$, $V_\theta$ and $V_\varphi$ are the components of the wave normal, which are normalized such that $V_r^2 + V_\theta^2 + V_\varphi^2 = real(n^2)$.

# Bibliography


[1] Bernhardt, P.A. and L.M. Duncan, The feedback-diffraction theory of ionospheric heating, *J. Atmos. and Terr. Phys., 44*, No. 12, 1061, 1982.

[2] Bernhardt, P. A., L. M. Duncan, and C. A. Tepley (1988), Artificial airglow excited by high-power radio waves, *Science 242*, 1022.

[3] Bernhardt, P. A., L. M. Duncan, and C. A. Tepley, Heater-induced cavities as optical tracers of plasma drifts, *J. Geophys. Res., 94*, 7003-7010, 1989.

[4] Bristow, W. A., and R. A. Greenwald (1995), Estimating gravity wave parameters from oblique high-frequency backscatter: Modeling and analysis, *J. Geophys. Res., 100(A3)*, 36393648, doi:10.1029/94JA02704.

[5] Budden, K. G. (1985), *The Propagation of Radio Waves*, doi:10.1017/CBO9780511564321, Cambridge Univ. Press, New York.

[6] Cervera, M. A., and T. J. Harris (2014), Modeling ionospheric disturbance features in quasi-vertically incident ionograms using 3-D magnetoionic ray tracing and atmospheric gravity waves, *J. Geophys. Res. Space Physics, 119*, 431440, doi:10.1002/2013JA019247.

[7] Chum, J., T. Sindelrov, J. Lastovicka, F. Hruska, D. Buresov, and J. Base (2010), Horizontal velocities and propagation directions of gravity waves in the ionosphere over the Czech Republic, *J. Geophys. Res., 115*, A11322, doi:10.1029/2010JA015821.

[8] Crowley, G., and F. S. Rodrigues (2012), Characteristics of traveling ionospheric disturbances observed by the TIDDBIT sounder, *Radio Sci., 47*, RS0L22, doi:10.1029/2011RS004959.

[9] Davies, K., and D. M. Baker (1966), On frequency variations of ionospherically propagated HF radio signals, *Radio Sci., 1*, 545556.

[10] Drob, D. P., J.T. Emmert, J.W. Meriwether, J.J. Makela, E. Doornbos, M. Conde, G. Hernandez, J. Noto, K.A. Zawdie, S.E. McDonald, J.D. Huba, J.H. Klenzing (2015), An Update to the Horizontal Wind Model (HWM): The Quiet Time Thermosphere, *Earth and Space Science, 2*, doi:10.1002/2014EA000089.

[11] Duly, T. M., J. D. Huba, and J. J. Makela (2014), Self-consistent generation of MSTIDs within the SAMI3 numerical model, *J. Geophys. Res. Space Physics, 119*, 67456757, doi:10.1002/2014JA020146.

[12] Duncan, L. M., J. P. Sheerin, and R. A. Behnke (1988), Observations of ionospheric cavities generated by high-power radio waves, *Phys. Rev. Lett. 61*, 239.

[13] Eccles, J. V., J. P. St. Maurice, and R. W. Schunk (2015), Mechanisms underlying the prereversal enhancement of the vertical plasma drift in the low-latitude ionosphere. *J. Geophys. Res. Space Physics, 120*, 49504970. doi: 10.1002/2014JA020664.

[14] Garcia, F. J., M. C. Kelley, J. J. Makela, and C.-S. Huang (2000), Airglow observations of mesoscale low-velocity traveling ionospheric disturbances at midlatitudes, *J. Geophys. Res., 105(A8)*, 1840718415, doi:10.1029/1999JA000305.

[15] Georges, T. M., and J. J. Stephenson (1969), HF Radar Signatures of Traveling Ionospheric Irregularities, 3D Ray-Tracing Simulation, *Radio Sci., 4(8)*, 679696, doi:10.1029/RS004i008p00679.

[16] Gurevich, A. V., A. V. Lukyanov, and K. P. Zybin (1996), Anomalous absorption of powerful radio waves on the striations developed during ionospheric modification, *Phys. Lett. A 211*, 363, doi:10.1016/0375-9601(95)00970-1.

[17] Haselgrove, C. B., and J. Haselgrove (1960), Twisted ray paths in the ionosphere, *Proc. Phys. Soc. London, 75*, 357363.

[18] Heelis, R. A. (2004), Electrodynamics in the low and middle latitude ionosphere: A tutorial, *J. Atmos. Sol. Terr. Phys., 66*, 825838.

[19] Hooke, W. H. (1969), E-region ionospheric irregularities produced by internal atmospheric gravity waves, *Planet. Space Sci., 17*, 749765, doi:10.1016/0032-0633(69)90195-0.

[20] Huba, J. D., G. Joyce, and J. A. Fedder (2000), Sami2 is Another Model of the Ionosphere (SAMI2): A new low-latitude ionosphere model, *J. Geophys. Res., 105(A10)*, 2303523053, doi:10.1029/2000JA000035.

[21] Huba, J. D., G. Joyce and J. Krall (2008), Three-dimensional equatorial spread *F* modeling, *Geophys. Res. Lett. 35*, L10102, doi:10.1029/2008GL033509.

[22] Huba, J. D., J. Krall, and G. Joyce (2009), Atomic and molecular ion dynamics during equatorial spread F, *Geophys. Res. Lett., 36*, L10106, doi:10.1029/2009GL037675.

[23] Huba, J. D., G. Joyce, J. Krall, and J. Fedder (2009), Ion and electron temperature evolution during equatorial spread F, *Geophys. Res. Lett., 36*, L15102, doi:10.1029/2009GL038872.

[24] Huba, J. D., S. L. Ossakow, G. Joyce, J. Krall, and S. L. England (2009), Three-dimensional equatorial spread F modeling: Zonal neutral wind effects, *Geophys. Res. Lett., 36*, L19106, doi:10.1029/2009GL040284.

[25] Huba, J. D., and J. Krall (2013), Impact of meridional winds on equatorial spread *F*: Revisited, *Geophys. Res. Lett., 40*, 12681272, doi:10.1002/grl.50292.

[26] Huba, J. D., D. Drob, T.-W. Wu, and J. J. Makela (2015), Modeling the Ionospheric Impact of Tsunami-driven Gravity Waves with SAMI3: Conjugate Effects, *Geophys. Res. Lett., 42*, doi:10.1002/2015GL064871.

[27] Hysell, D. L. (2000), An overview and synthesis of plasma irregularities in equatorial spread F , *J. Atmos. Sol. Terr. Phys., 62*, 10371056.

[28] Jones, R. M., and J. J. Stephenson (1975), A versatile three-dimensional ray tracing computer program for radio waves in the ionosphere, *NASA STI/Recon Technical Report N, 76*, 25,476.

[29] Kelley, M. C., M. F. Larsen, C. LaHoz, and J. P. McClure (1981), Gravity wave initiation of equatorial spread F: A case study, *J. Geophys. Res., 86(A11)*, 90879100, doi:10.1029/JA086iA11p09087.

[30] Kelley, M. C. (2009), *The Earth's Ionosphere*, Academic Press, Burlington, MA.

[31] Kelley, M. C., J. J. Makela, O. de La Beaujardire, and J. Retterer (2011), Convective ionospheric storms: A review, *Rev. Geophys., 49*, RG2003, doi:10.1029/2010RG000340.

[32] Krall, J., J. D. Huba, G. Joyce, and S. T. Zalesak. (2009), Three-dimensional simulation of equatorial spread F with meridional wind effects, *Ann. Geophys., 27*, 18211830.

[33] Krall, J., J. D. Huba, S. L. Ossakow, G. Joyce, J. J. Makela, E. S. Miller, and M. C. Kelley (2011), Modeling of equatorial plasma bubbles triggered by non-equatorial traveling ionospheric disturbances, *Geophys. Res. Lett., 38*, L08103, doi:10.1029/2011GL046890.

[34] Krall, J., J. D. Huba, G. Joyce, and M. Hei (2013), Simulation of the seeding of equatorial spread F by circular gravity waves, *Geophys. Res. Lett., 15*, doi:10.1029/2012GL054022.

[35] Krall, J., J. D. Huba, and D. C. Fritts (2013), On the seeding of equatorial spread F by gravity waves, *Geophys. Res. Lett., 40*, 661664, doi:10.1002/grl.50144.

[36] Lobb, R. J., and J. E. Titheridge (1977), The effects of travelling ionospheric disturbances on ionograms, *J. Atmos. Terr. Phys., 39*, 129138.

[37] Maruyama, T. (1988), A diagnostic model for equatorial spread F, 1, Model description and application to electric field and neutral wind effects, *J. Geophys. Res., 93(A12)*, 1461114622, doi:10.1029/JA093iA12p14611.

[38] Milikh, G. M., K. Papadopoulos, H. Shroff, C. L. Chang, T. Wallace, E. V. Mishin, M. Parrot, and J. J. Berthelier (2008), Formation of artificial ionospheric ducts, *Geophys. Res. Lett., 35*, L17104, doi:10.1029/2008GL034630.

[39] Milikh, G. M., E. Mishin, I. Galkin, A. Vartanyan, C. Roth, and B. W. Reinisch (2010), Ion outflows and artificial ducts in the topside ionosphere at HAARP, *Geophys. Res. Lett., 27*, L18102, doi:10.1029/2010GL044636.

[40] Milikh, G. M., A. G. Demekhov, K. Papadopoulos, A Vartanyan, J. D. Huba, and G. Joyce (2010), Model for artificial ionospheric duct formation due to HF heating, *Geophys. Res. Lett., 37*, L07803, doi:10.1029/2010GL042684.

[41] Milikh, G. M., A. Demekhov, A. Vartanyan, E. V. Mishin, and J. Huba (2012), A new model for formation of artificial ducts due to ionospheric HF-heating, *Geophys. Res. Lett., 39*, L10102, doi:10.1029/2012GL051718.

[42] Newman, A. L., H. C. Carlson Jr., G. P. Mantas, and F. T. Djuth (1988), Thermal response of the F-region ionosphere for conditions of large HF-induced electron-temperature enhancements, *Geophys. Res. Lett., 15*, 311.

[43] Papadopoulos, K. (2015), Ionospheric Modifications Using Mobile. High Power HF Transmitters based on HPM Technology, ICPPS 2015, Antalya, Turkey.

[44] Perrine, R. P., G. M. Milikh, K. Papadopoulos, J. D. Huba, G. Joyce, M. Swisdak, and Y. Dimant (2006), An interhemispheric model of artificial ionospheric ducts, *Radio Sci. 41*, RS4002, doi:10.1029/2005RS003371.

[45] Pedersen, T., B. Gustavsson, E. Mishin, E. MacKenzie, H. C. Carlson, M. Starks, and T. Mills (2009), Optical ring formation and ionization production in high-power HF heating experiments at HAARP, *Geophys. Res. Lett., 36*, L18107, doi:10.1029/ 2009GL040047.

[46] Perkins, F. (1973), Spread F and ionospheric currents, *J. Geophys. Res., 78(1)*, 218226, doi:10.1029/JA078i001p00218.

[47] Picone, J. M., A. E. Hedin, D. P. Drob, and A. C. Aikin (2002), NRLMSISE-00 empirical model of the atmosphere: Statistical comparisons and scientific issues, *J. Geophys. Res., 107*, 1468, doi:10.1029/2002JA009430.

[48] Press, W. H., B. P. Flannery, S. A. Teukolsky, and W. T. Vetterling (1986). Numerical recipes: The art of scientific programming. Cambridge University Press, Cambridge, New York.

[49] Rowland, H.L. and P.A. Bernhardt, A nonlinear oscillator in the ionosphere: Beam snapback during RF heating, in *Physics of Space Plasmas*, T. Chang, Editor, SPI Conference Proceedings and Reprint Series, Number 11, 1991.

[50] Robert W. Schunk and Andrew F. Nagy (2000). *Ionospheres: Physics, Plasma Physics, and Chemistry*. Cambridge University Press, Cambridge.

[51] Shiokawa, K., C. Ihara, Y. Otsuka, and T. Ogawa (2003), Statistical study of nighttime medium-scale traveling ionospheric disturbances using mid-latitude airglow images, *Journal of Geophysical Research, 108(A1)*, 1052, doi:10.1029/2002JA009491.

[52] Stocker, A. J., N. F. Arnold, and T. B. Jones (2000), The synthesis of travelling ionospheric disturbance (TID) signatures in HF radar observations using ray tracing, *Ann. Geophys., 18*, 5664, doi:10.1007/s00585-000-0056-4.

[53] Vadas, S. L., and G. Crowley (2010), Sources of the traveling ionospheric disturbances observed by the ionospheric TIDDBIT sounder near Wallops Island on 30 October 2007, *J. Geophys. Res., 115*, A07324, doi:10.1029/2009JA015053.

[54] Wilkinson, P. (1999), Scaling Ionograms, IPS Meeting.

[55] Wu, T.-W., J. D. Huba, G. Joyce, and P. A. Bernhardt (2012), Modeling Arecibo conjugate heating effects with SAMI2, *Geophys. Res. Lett., 39*, L07103, doi:10.1029/2012GL051311.

[56] Zalesak, S. T. and Huba, J. D. (1991): Effect of meridional winds on the development of equatorial spread-F , Eos Trans. AGU, 72, Spring Meet. Suppl., 211.

[57] Zawdie, K. A., J. D. Huba, and T.-W. Wu (2013), Modeling 3-D artificial ionospheric ducts, *J. Geophys. Res. Space Physics, 118*, 74507457, doi:10.1002/2013JA018823.